

**DEVELOPMENT OF REMEDIATION TECHNOLOGY FOR HAZARDOUS
HEXAVALENT CHROMIUM IN AQUEOUS SOLUTIONS USING g-C₃N₄ BASED
PHOTOCATALYST**

**A DISSERTATION SUBMITTED TO THE MIE UNIVERSITY IN PARTIAL
FULFILLMENT OF THE REQUIREMENT FOR THE DEGREE OF
DOCTOR OF PHILOSOPHY**

BY

AKLIMA KHATUN



**ANALYTICAL & ENVIRONMENTAL CHEMISTRY LABORATORY
DEPARTMENT OF APPLIED CHEMISTRY
GRADUATE SCHOOL OF ENGINEERING
MIE UNIVERSITY
MIE, JAPAN
SEPTEMBER, 2024**

Table of Contents

Table of Contents	II
List of Figures	VII
List of Tables	XII
List of Schemes	XII
Chapter One: General Introduction	
1.1 Introduction	2
1.2 Hexavalent Chromium	4
1.2.1 Sources of Hexavalent Chromium	6
1.2.2 Hexavalent Chromium Exposure	8
1.2.3 Effects on Human Health	9
1.2.4 Effects on Plant Health	9
1.3 Pollutants Removal Techniques	10
1.3.1 Adsorption	10
1.3.2 Chemical Precipitation	11
1.3.3 Membrane Filtration	13
1.3.4 Coagulation and Flocculation	15
1.3.5 Ion Exchange	15
	II

1.3.6 Electrochemical Treatment	16
1.3.7 Bioremediation	18
1.3.8 Photocatalytic Remediation	20
1.3.8.1 The Principle of Photocatalytic Reaction Mechanism	22
1.3.8.2 Photocatalytic Reduction Mechanism	23
1.3.8.3 Photocatalytic Degradation Mechanism	25
1.3.8.4 Improvement of photocatalytic Performance	26
1.4 Graphitic Carbon Nitride (g-C ₃ N ₄)	28
1.4.1 Modification of g-C ₃ N ₄	31
1.4.1.1 Metal doping	32
1.4.1.2 Non-metal doping	34
1.4.1.3 Metal deposition (co-catalyst)	34
1.4.1.4 Molecular Doping	35
1.4.1.5 Heterojunction	35
1.4.1.6 Morphology Modulation	39
1.5 Objectives of the Research	41
□ General Objectives	41
□ Specific Objectives	41
1.6 References	42

Chapter Two: Facile Synthesis of ZnO/g-C₃N₄ with Enhanced Photocatalytic Performance for the Reduction of Cr(VI) in Presence of EDTA Under Visible Light Irradiation

2.1 Introduction	66
2.2 Experimental	68
2.2.1 Chemicals	68
2.2.2 Synthesis of ZnO/g-C ₃ N ₄ Composite	69
2.2.3 Synthesis of ZnO and g-C ₃ N ₄	69
2.2.4 Characterization	70
2.2.5 Photocatalytic Reduction of Cr(VI) to Cr(III)	71
2.3 Results and Discussion	72
2.3.1 Structural Investigation of Synthesized Composite	72
2.3.2 Optical Properties	79
2.3.3 Photocatalytic Activity	82
2.3.4 Possible Reaction Mechanisms	90
2.4 Conclusions	93
2.5 References	95

Chapter Three: Facile Fabrication of Ag/g-C₃N₄ Photocatalyst with Visible Light Responsive Efficiency for Cr(VI) Reduction in Presence of EDTA

3.1 Introduction	107
3.2 Materials and Methods	109

3.2.1 Chemicals and Materials	109
3.2.2 Synthesis of Ag/g-C ₃ N ₄	110
3.2.3 Characterization	110
3.2.4 Photocatalytic Reduction	111
3.3 Results and Discussion	112
3.3.1 TG Analysis	112
3.3.2 XRD Analysis	112
3.3.3 FTIR Analysis	113
3.3.4 XPS Analysis	115
3.3.5 BET Surface Area and Pore Size Distribution Analysis	116
3.3.6 Morphological Analysis	118
3.3.7 Optical Properties Analysis	120
3.3.8 PL Analysis	120
3.3.9 EIS Analysis	121
3.3.10 Mott-Schottky plots, Valance Band (VB) XPS Analysis and Band Diagram	122
3.3.11 The Photocatalytic Activity	124
3.3.12 Effect of Ag Content	125
3.3.13 Effect of Calcination Temperature and Time	126
3.3.14 Effect of Catalyst Dosages	127

3.3.15 Effect of EDTA Concentration	128
3.3.16 Effect of Initial Concentration	130
3.3.17 Effect of pH	130
3.3.18 Reaction Mechanism	137
3.3.19 Reusability	134
3.4 Conclusions	136
3.5 References	137
Chapter Four: Summary and Thesis Conclusions	
4.1 Summary and Thesis Conclusions	154
List of Published Articles	157
<i>List of Attending Conference</i>	158

List of Figures

Figure name	Page No.
1.1 Sources of heavy metals.	3
1.2 Groups of heavy metals.	4
1.3 Chemical species of Cr(VI) as a function of pH	6
1.4 Schematic diagram presenting different removal techniques used for the removal of toxic heavy metal, organic and other pollutants.	10
1.5 Schematic diagram for the advantages and disadvantages of photocatalytic remediation methods.	22
1.6 A general mechanism presenting photocatalytic reduction or degradation of pollutants. M: compounds in reductive reactions; and O: compounds in oxidative reactions.	23
1.7 Schematic diagram of possible photocatalytic mechanism for the reduction of Cr(VI) by g-C ₃ N ₄ .	25
1.8 Schematic diagram of possible photocatalytic mechanism for the degradation of organic pollutant by g-C ₃ N ₄ photocatalyst under light irradiation.	26
1.9 Schematic diagram of possible photocatalytic mechanism for the reduction of Cr(VI) by g-C ₃ N ₄ in presence of EDTA.	27
1.10 The g-C ₃ N ₄ synthesis via thermal polymerization of different precursors.	29
1.11 Schematic illustration of photoexcited electron–hole pairs in g-C ₃ N ₄ with possible decay pathways. A and D denote electron acceptor and electron donor.	30
1.12 Common modification methods of g-C ₃ N ₄ .	32
1.13 Schematic diagram of possible photocatalytic mechanism for the reduction of Cr(VI) by g-C ₃ N ₄ by the introduction of Ag metal in the presence of EDTA.	33

1.14	Charge transfer mechanism of (a) Type I, (b) Type III, (c) Type II, and (d) Z-scheme heterojunctions.	37-38
1.15	Charge transfer in the conventional Type II g-C ₃ N ₄ based heterojunction systems constructed by coupling g-C ₃ N ₄ to a second semiconductor ZnO, for the reduction of Cr(VI) in the presence of EDTA.	39
2.1	TG analysis curve for ZnO/g-C ₃ N ₄ composite until 950 °C at a heating rate of 10 °C min ⁻¹ .	73
2.2	(a) XRD patterns and (b) FTIR spectra for ZnO, g-C ₃ N ₄ , ZnO/g-C ₃ N ₄ and ZnO/g-C ₃ N ₄ after reaction.	74
2.3	SEM images of (a) ZnO, (b) g-C ₃ N ₄ , (c) ZnO/g-C ₃ N ₄ and (d) ZnO/g-C ₃ N ₄ after reaction.	75
2.4	TEM images of (a) ZnO, (b) g-C ₃ N ₄ , (c) ZnO/g-C ₃ N ₄ and (d) ZnO/g-C ₃ N ₄ after reaction.	76
2.5	XPS spectra of g-C ₃ N ₄ , and ZnO/g-C ₃ N ₄ composite. (a) survey spectra of ZnO/g-C ₃ N ₄ composite and g-C ₃ N ₄ , high resolution; (b) C1s, (c) N1s, and (d) O1s XPS spectra of ZnO/g-C ₃ N ₄ and g-C ₃ N ₄ ; (f) Zn 2p peaks of ZnO/g-C ₃ N ₄ composite.	78
2.6	(a) N ₂ adsorption-desorption isotherms and (b) pore size distribution curves of g-C ₃ N ₄ and ZnO/g-C ₃ N ₄ composite.	79
2.7	(a) UV-visible DRS for ZnO, g-C ₃ N ₄ , ZnO/g-C ₃ N ₄ and ZnO/g-C ₃ N ₄ after reaction; and Tauc plot (b) for g-C ₃ N ₄ , ZnO/g-C ₃ N ₄ , ZnO/g-C ₃ N ₄ after reaction and (c) for ZnO.	80
2.8	(a) Photoluminescence spectra of ZnO, g-C ₃ N ₄ , ZnO/g-C ₃ N ₄ and ZnO/g-C ₃ N ₄ after reaction and (b) Nyquist plots of g-C ₃ N ₄ , ZnO/g-C ₃ N ₄ .	81
2.9	(a) Photocatalytic reduction of Cr(VI) with several conditions. (b) Effect of zinc acetate amount as ZnO precursor. (c) Effect of heating temperature programs of the composite. Photocatalytic reduction of	83

Cr(VI) by ZnO/g-C ₃ N ₄ in presence of EDTA; Cr(VI): 20 ppm, EDTA: 500 ppm, ZnO/g-C ₃ N ₄ : 40 mg.	
2.10 Effect of (a) concentration of EDTA, (c) photocatalyst dosage, (d) initial concentration of Cr(VI) and (f) initial pH on the photocatalytic Cr(VI) reduction by ZnO/g-C ₃ N ₄ . (b) Plot of ln(C ₀ /C) verses irradiation time at different concentration of EDTA. (e) Reduced amount of Cr at different concentrations of Cr(VI) on the photocatalytic reduction of Cr(VI) by ZnO/g-C ₃ N ₄ in the presence of EDTA. (g) Reusability of ZnO/g-C ₃ N ₄ .	87-88
2.11 VBXPS spectra of ZnO/g-C ₃ N ₄ composite.	90
2.12 Proposed mechanisms for photocatalytic reduction of Cr(VI) by ZnO/g-C ₃ N ₄ in presence of EDTA.	93
3.1 (a) TG analysis curve for Ag/g-C ₃ N ₄ composite, (b) XRD patterns of g-C ₃ N ₄ , and Ag/g-C ₃ N ₄ , (c) Standard XRD cards of JCPDS 87-1526 and 65-2871, and (d) FTIR spectra of g-C ₃ N ₄ , and Ag/g-C ₃ N ₄ .	113-114
3.2 The crystal structure of the 100 and 002 planes in g-C ₃ N ₄ and the (002) plane in Ag/g-C ₃ N ₄ .	114
3.3 (a) Survey XPS spectra of Ag/g-C ₃ N ₄ composite and g-C ₃ N ₄ ; overlapping high resolution (b) C 1s, (c) N 1s, and (d) O 1s XPS spectra of Ag/g-C ₃ N ₄ and g-C ₃ N ₄ and (e) high resolution Ag 3d XPS spectra of Ag/g-C ₃ N ₄ composite.	116
3.4 N ₂ adsorption-desorption isotherms (a,c) and pore size distribution curves (b,d) of g-C ₃ N ₄ and Ag/g-C ₃ N ₄ composite.	117
3.5 SEM images of (a) g-C ₃ N ₄ , and (b) Ag/g-C ₃ N ₄ and TEM images of (c) g-C ₃ N ₄ , and (d) Ag/g-C ₃ N ₄ .	118-119
3.6 EDS mapping of Ag/g-C ₃ N ₄ with SEM and EDX spectra.	119
3.7 (a) UV-visible DRS, (b) Tauc plot, (c) Photoluminescence spectra and (d) Nyquist plots of g-C ₃ N ₄ , and Ag/g-C ₃ N ₄ (inset figure: equivalent circuit diagram).	122

3.8 Mott-Schottky plots for (a) g-C ₃ N ₄ and (b) Ag/g-C ₃ N ₄ , VBXPS analysis of (c) g-C ₃ N ₄ and (d) Ag/g-C ₃ N ₄ , and (e) energy band diagram of g-C ₃ N ₄ and Ag/g-C ₃ N ₄ .	124
3.9 (a) Photocatalytic reduction of Cr(VI) with several conditions and (b) corresponding plot of $\ln(C_0/C)$ versus irradiation time; Cr(VI): 20 ppm (30mL), photocatalyst: 40 mg, EDTA-2Na: 400 ppm (EDTA: 314 ppm).	125
3.10 Effect of Ag content (percentage of used Ag with respect to the weight of urea in the Ag/g-C ₃ N ₄ preparation) on the photocatalytic Cr(VI) reduction by Ag/g-C ₃ N ₄ in presence of EDTA; Cr(VI): 20 ppm (30mL), photocatalyst: 30 mg, EDTA-2Na: 500 ppm (EDTA: 392 ppm).	126
3.11 Effect of (a) heating temperature for 5 h and (b) calcination time at 500 °C of the composite fabrication on the photocatalytic Cr(VI) reduction by Ag/g-C ₃ N ₄ in presence of EDTA; Cr(VI): 20 ppm (30 mL), photocatalyst: 30 mg, EDTA-2Na: 500 ppm (EDTA: 392 ppm).	127
3.12 (a) Effect of photocatalyst dosage on the photocatalytic Cr(VI) reduction and (b) corresponding Plot of $\ln(C_0/C)$ versus irradiation time; Cr(VI): 20 ppm (30mL), EDTA-2Na: 500 ppm (EDTA: 392 ppm).	128
3.13 Effect of EDTA on the photocatalytic Cr(VI) reduction by Ag/g-C ₃ N ₄ ; Cr(VI): 20 ppm (30mL), photocatalyst: 40 mg.	129
3.14 Effect of initial concentration on (a) photocatalytic Cr(VI) reduction and (b) reduced amount of Cr by Ag/g-C ₃ N ₄ in presence of EDTA; Cr(VI): 20 ppm (30mL), photocatalyst: 40 mg, EDTA-2Na: 400 ppm (EDTA: 314 ppm).	130
3.15 Effect of initial pH on the photocatalytic Cr(VI) reduction by Ag/g-C ₃ N ₄ in presence of EDTA; Cr(VI): 20 ppm (30mL), photocatalyst: 40 mg, EDTA-2Na: 400 ppm (EDTA: 314 ppm).	131

3.16	(a) Interaction of scattered visible light with Ag/g-C ₃ N ₄ and (b) Proposed mechanisms for photocatalytic reduction of Cr(VI) by Ag/g-C ₃ N ₄ in presence of EDTA.	133
3.17	Reusability of Ag/g-C ₃ N ₄ on the photocatalytic Cr(VI) reduction in presence of EDTA.	134

List of Tables

Table names	Page No.
1.1 The four naturally occurring isotopes of Cr.	5
1.2 The widely practiced semiconductor photocatalysts	21
2.1 Surface area, pore size and pore volume of the g-C ₃ N ₄ and ZnO/g-C ₃ N ₄ composite	79
2.2 Kinetic parameters for the photocatalytic reduction of Cr(VI)	85
2.3 Photocatalytic reduction of Cr(VI) activity of synthesized ZnO/g-C ₃ N ₄ composite and some other reported composite	89
3.1 Surface area, pore volume, and pore diameter of the g-C ₃ N ₄ and Ag-g-C ₃ N ₄ composite	118
3.2 Photocatalytic reduction of Cr(VI) activity of synthesized Ag/g-C ₃ N ₄ composite and some other recent reported g-C ₃ N ₄ -based composite	135

List of Schemes

Scheme names	Page No.
2.1 Schematic diagram for the formation of the ZnO/g-C ₃ N ₄ Composite	70

CHAPTER ONE

General Introduction

1.1 Introduction

Urbanization and rapid industrial developments lead to many advantages for the daily lives of humans. Hence, a large number of industries have been developed worldwide to fulfill our needs. These industries directly discharge waste into the environment, which has an adverse effect on the ecosystem by polluting the air, water, and soil. Worldwide, about 80% of municipal and industrial wastes are released into the environment without being properly treated [1,2]. In the consideration of industrial waste containing polluted water, several categories of pollutants can be highlighted, such as heavy metals, organic and inorganic contaminants, dyes, pharmaceutical wastes, spilled oil, and many more complex chemicals. Among them, heavy metals are not biodegradable, unlike organic pollutants, and they tend to accumulate in living things when they are released into the environment. These can have a detrimental effect on the health of all living things, including humans, animals, and plants [3]. Currently, discharged industrial effluents containing heavy metals, among other pollutants, have drawn more attention because of their harmful effects on both humans and other living things. The heavy metal ion is considered of the most toxic and hazardous environmental contaminants. Heavy metals have high stability, solubility, and ease of migration into aqueous media, which means minute levels of heavy metals can pose toxic effects on living things via the ecosystem [4]. There are 96 of the 118 known chemical elements are metals mentioned in the periodic table. In general, metals with a relatively high density, atomic number, or molecular weight are termed heavy metals [5]. They are the metallic elements of the periodic table and are also known as trace elements. Introduction of heavy metals into the environment can be attributed to both anthropogenic and natural causes. Human activities such as, mining, electronic waste, power plants, agricultural sources, industrial sources,

household waste, while natural phenomena such as soil erosion, volcanic activities, urban run offs and aerosols particulate [4]. The sources of heavy metals are shown schematically in Figure 1.1.

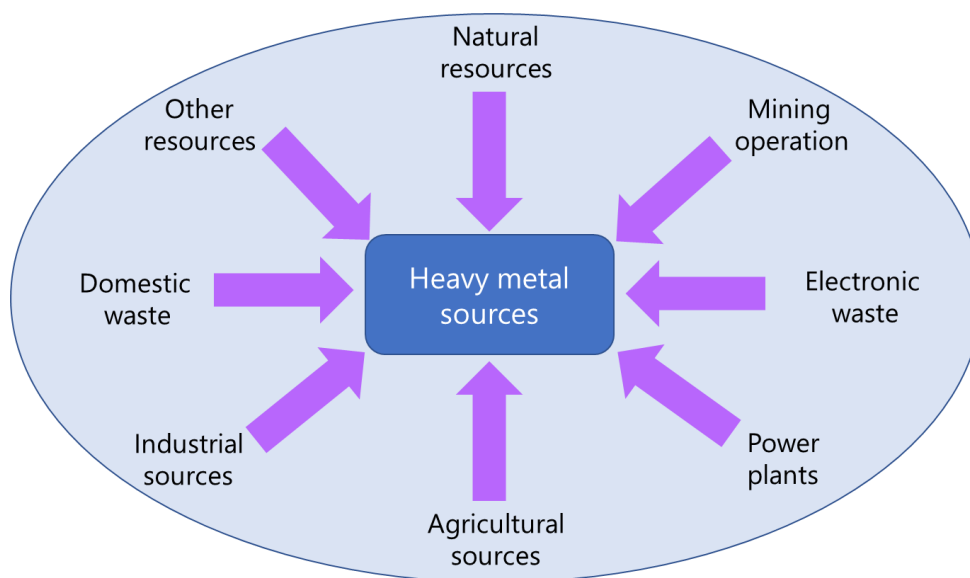


Figure 1.1 Sources of heavy metals.

Toxic heavy metals are more harmful than other pollutants like plastics, plant nutrients, pathogens, and synthetic organic and inorganic chemicals [6]. Both the ecosystem and human health may suffer from chronic exposure to low concentrations of toxic heavy metals, including tetragenic and carcinogenic effects [7]. Water contaminated with toxic heavy metals is a threat to all kinds of ecosystems, human health, and living things because these metals do not degrade in the environment and can build up in living tissue, disrupting the food chain. In 1987, the United States Environmental Protection Agency (EPA) announced a list of toxic elements in wastewater. It was found that the list contained most of the heavy metals [8]. Depending on the characteristics of metals, they are divided into four groups (Figure 1.2) [9]. Currently, researchers are more focused on the removal of toxic heavy and radioactive metals and their reuse for various productive purposes.

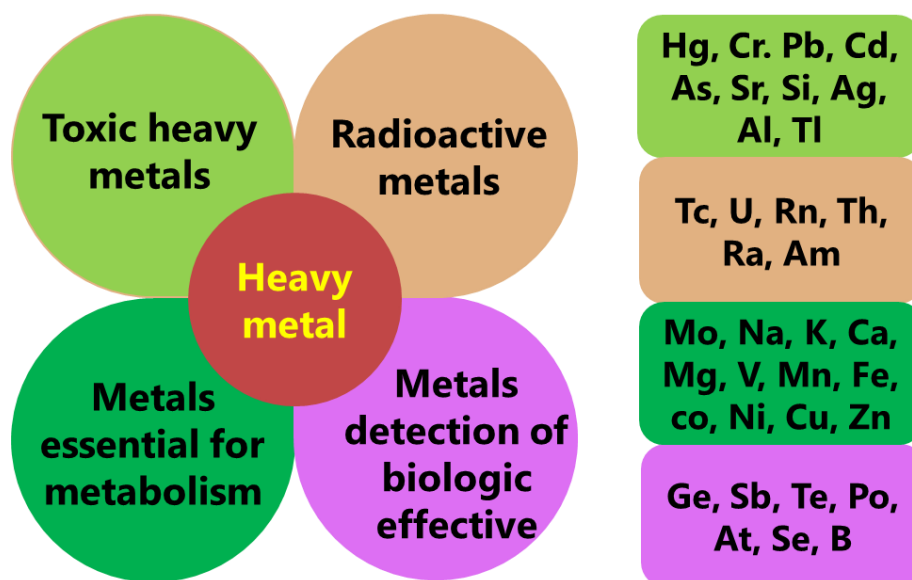


Figure 1.2 Groups of heavy metals.

1.2 Hexavalent Chromium

Chromium or Cr(VI) is an extremely toxic and 21st most abundant element found naturally in the mantle layer of the earth's crust [10,11]. It is the first element of Group VI-B and is situated between vanadium and manganese in the periodic table. Chromium was discovered by the French chemist Louis Vauquelin in 1797. It was named after the Greek word "chroma", because of the different colors found in the chromium-containing compounds [12]. Chromium has both physical and chemical properties like other elements. Physically, it is a steely gray, lustrous, hard metal. The basic properties of Cr are: atomic number 24, atomic weight 51.996 g mol⁻¹, melting point 1907 °C, boiling point 2671 °C, and atomic density of 7.14 g mL⁻¹ [13–16]. Also, chromium has four naturally occurring stable isotopes. The four isotopes of Cr and their relative abundances in the environment are listed in Table 1.1 [17].

Table 1.1 The four naturally occurring isotopes of Cr.

Isotopes of Cr	Relative abundances in the environment (%)
^{50}Cr	4.35
^{52}Cr	83.79
^{53}Cr	9.50
^{54}Cr	2.36

Though the oxidation states of Cr vary from -2 to + 6, but three thermodynamically stable Cr forms are present in the environment. These are Cr (0) i.e., metallic forms of chromium, trivalent chromium or Cr (III) and hexavalent chromium or Cr (VI). While Cr(0) as Cr-ores and Cr(III) are present naturally, Cr (VI) is rarely found in nature and mostly generated from anthropogenic activities. Elemental Cr(0) is inert in biological materials used for the manufacturing of steel and other alloys. Cr (III) is non-toxic due to its lower mobility and relative insolubility in water. It is considered an essential element for living creatures, including humans, but its absence or excess severely affects their metabolism. Cr (VI) is highly soluble in water and noxious to living organisms [18–22]. Cr(III) is typically found as an insoluble hydroxide cation, whereas Cr (VI) is an oxyanion species, in the likes of chromate (CrO_4^{2-}), dichromate ($\text{Cr}_2\text{O}_7^{2-}$), hydrogen chromate (HCrO_4^-), and dihydrogen chromate (H_2CrO_4^-), ions governed by the solution pH. The distribution of Cr(VI) species in the three pH zones is found in Figure1.3. The initial concentration of Cr(VI) is $30 \mu\text{g}\cdot\text{mL}^{-1}$ ($0.483 \text{ mmol}\cdot\text{L}^{-1}$), and the total chromium (VI) concentration C was fixed to $0.1 \text{ mmol}\cdot\text{L}^{-1}$ in order to obtain species of chromium (VI). Substantial H_2CrO_4^- concentrations occur

under the extreme condition of $\text{pH} \leq 0$, while HCrO_4^- and $\text{Cr}_2\text{O}_7^{2-}$ generally dominate in the range of pH 2 to 6. And CrO_4^{2-} predominately exists when pH is above 6.5 [11,20,23,24].

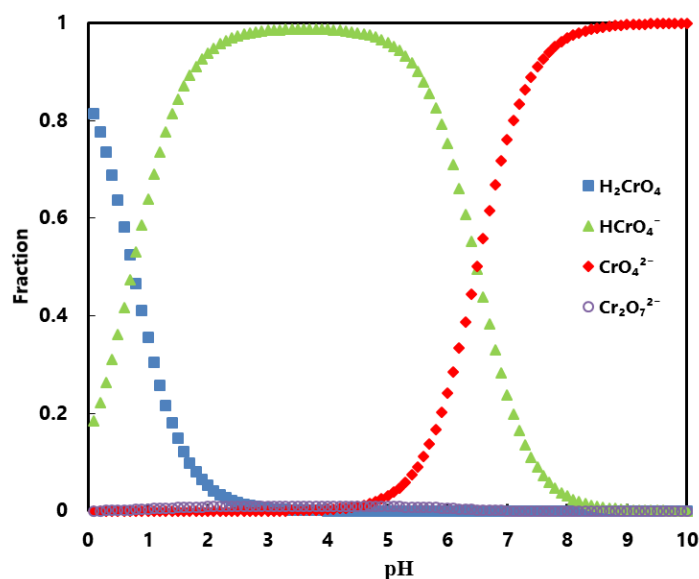


Figure 1.3 Chemical species of Cr(VI) as a function of pH

Humans are exposed to Cr(VI) through occupational hazards. In 1920, Brieger reported the first case of bronchogenic cancer among German workers in the chrome ore industry. Then, there are various reports that Cr(VI) is carcinogenic to different kinds of organisms, and the International Agency for Research on Cancer (IARC) classified it as a Group I human carcinogen in 1980 [20,21,25]. Due to the toxicity of Cr(VI), the permissible limits of Cr(VI) in drinking water are 0.05 mg/L and 0.1 mg/L, according to the World Health Organization (WHO) and the United States Environmental Protection Agency (USEPA) [26,27]. The sources and impact of chromium pollution will be explained in the next section.

1.2.1 Sources of Hexavalent Chromium

Chromium is mostly generated from anthropogenic activities. A huge amount of chromium is extracted annually due to numerous industrial and agricultural applications. The sources of

hexavalent chromium are categorized as follows [15,26,28–30]:

- ◆ Lead chromate, Crocoite, chrome yellow, chromic oxide, and chrome green are utilized in the pigment, paint, ink, dye, and plastic industries. Through these industries chromium comes into the environment.
- ◆ A huge amount of ammonium dichromate ($(\text{NH}_4)_2\text{Cr}_2\text{O}_4$) is used in the leather tanning industry to remove fur from skin. One of the main sources of Cr(VI) in aquatic environments is the tannery industry.
- ◆ Chrome plating (a thin layer of Cr on a metal substrate) is where chromic acid is used due to its anti-corrosive properties. The chrome plating industry is also responsible for toxic Cr(VI) pollution.
- ◆ Iron-based alloy (10% Cr) is added to steel for hardening it and for producing stainless steel. Due to its stable crystal structure, moderate thermal expansion, and high melting point, chromite is utilized to produce molds for brick production.
- ◆ Cr (VI) is used as a catalyst in the process of dyeing and directly as a chrome dye for the coloration of wool in textile manufacturing.
- ◆ The rubber manufacturing industry used chromium oxide as a dye to impart color to white rubber.
- ◆ Welding fume from stainless steel or nonferrous chromium alloys is also a source of Cr(VI).
- ◆ Organic fertilizers (such as biosolids and phosphorus fertilizers) contain considerable amounts of Cr, which contributes to the Cr contamination of agricultural soils.
- ◆ Cr is also unconfined into the environment (water, soil, and air), geochemically and naturally, i.e., volcanic activity and rock dust.

Hence, Cr [VI] is mostly found in environments as a result of industrialization. These industries discharged Cr-infested effluent into the environment directly. For example, chromium sulfate is used in the leather and tanning industry in Bangladesh. Note that Hazaribagh is home to 187 tanneries in the western part of the capital city of Dhaka, Bangladesh. About 85,000 tons of raw hide/skin are processed annually for leather production in Bangladesh, generating huge amounts of solid and liquid waste. Sadly, there isn't an effluent treatment plant (ETP); therefore, all waste is directly mixed with the water of the River Buriganga, which causes serious environmental pollution [31]. It is reported that the Cr concentration in the Buriganga River rises to 1.43 mg/L and 1.96 mg/L in the summer and winter seasons, respectively [32]. Not only in Bangladesh, the occurrence of Cr contamination is widespread in regions of South America, Eastern Africa, India, and China as a result of the rising industrial use of the Cr element [33].

1.2.2 Hexavalent Chromium Exposure

Cr (VI) is a significant environmental pollutant that poses a threat to both animal and plant health [34]. There are three considerable ways that humans are exposed to Cr(VI): by skin adsorption, ingestion (eating or drinking), or inhalation (breathing) of Cr-containing particles [11,35]. The main sources of chromium exposure by ingestion for humans are chromium-containing foods and drinking water. The air contains Cr(VI) in the form of dust, aerosols, and fumes due to its very non-volatile properties. Therefore, humans may intake Cr(VI) from these sources through inhalation. Moreover, certain levels of chromium can enter the skin when the body comes into contact with chromium-containing products or soil [12]. Cr (VI) exposure can be categorized as acute (lasting 14 days), intermediate (lasting 75–364 days), or chronic (lasting 365 days) based on the length of exposure [26,36,37].

1.2.3 Effects on Human Health

- ✧ The risk of lung cancer is increased by long-term inhalation of Cr(VI) compounds [36,38].
- ✧ Excessive exposure to Cr (VI) by inhaling may cause breathing issues such as asthma, coughing, shortness of breath, or wheezing, as well as nasal lining irritation, nose ulcers, and runny nose [11].
- ✧ Long-term exposure to Cr(VI) can damage the liver, kidney, circulatory system, and nerve tissues [39].
- ✧ Severe skin swelling and redness are symptoms of allergic responses to Cr(VI) [11].
- ✧ Clinical symptoms associated with acute Cr(VI) toxicity include vomiting, diarrhea, and blood loss into the gastrointestinal system, which can lead to cardiovascular problems [11].
- ✧ Moreover, Cr(VI) exposure results in skin ulcers, brain damage, encephalopathy symptoms, pneumonia, organoleptic difficulties, emphysema, and bronchitis. It also causes necrosis, which is the localized death of cells in live human parts [11].

1.2.4 Effects on Plant Health

- ✧ Cr (VI) toxicity manifests in plants as poor grain production, delayed seed germination, damaged roots, decreased root development, reduced biomass, decreased plant height, impaired photosynthetic capacity, membrane damage, chlorosis, and necrosis of the leaves [26].
- ✧ Cr(VI) can interfere with the electron transport chain and other metabolic processes, which can have an adverse impact on the photosynthesis process of plants [40].
- ✧ Furthermore, Cr(VI) may interfere with the ability of plants to absorb nutrients from the soil [13,41].

1.3 Pollutants Removal Techniques

Heavy metal, organic and other pollutants can generally be removed by adopting the following techniques (Figure 1.4).

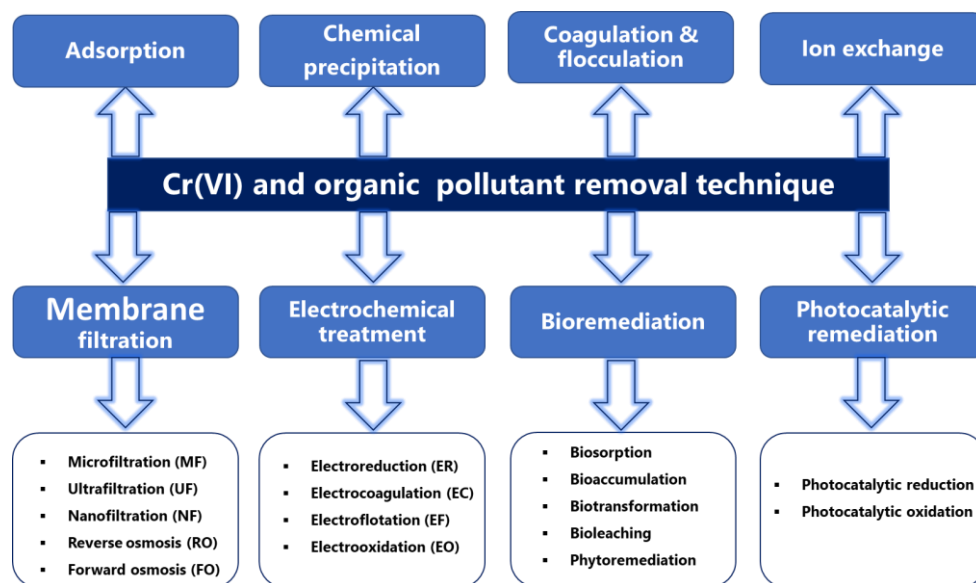


Figure 1.4 Schematic diagram presenting different removal techniques used for the removal of toxic heavy metal, organic and other pollutants.

1.3.1 Adsorption

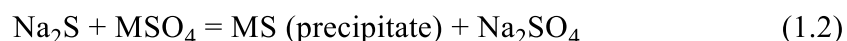
Adsorption is the most commonly utilized cost-effective, and efficient technique for heavy metal wastewater treatment. It is a process of separation in which adsorbate is moved from the liquid phase to the surface of the adsorbent and becomes bound by physical and chemical interactions [9,11,42]. The substance that concentrates at the surface is termed as adsorbate, and the material upon whose surface the adsorption takes place is called an adsorbent. The adsorption process has emerged as a preferred method for removing heavy metals from wastewater because of its low operation cost, ease of operation, high regeneration capacity, and excellent efficiency [43]. Typically, heavy metals are adsorbed onto the surface of a variety of negatively modified

materials. Adsorption of heavy metals on an adsorbent can be measured using grams of heavy metal in grams of adsorbent. It's the relationship between adsorbent and adsorbate. To identify the mechanisms of heavy metal adsorption, different mechanisms are used, including Langmuir and Freundlich adsorption isotherms. The factors: surface area of adsorbent, nature of adsorbate, initial concentration of adsorbate, pH, temperature, dosage of adsorbents, contact time, the presence of other organic components, and pressure influence the adsorption mechanism. Different adsorbents such as, activated-carbon, zeolites, alumina, iron oxide, manganese oxides, etc., have been applied for the removal of heavy metals [44] [45]. Recently, a porous composite hydrogel based on graphene has been proven effective for removing heavy metal ions from wastewater [46,47]. Also, activated carbon has a special place among the adsorbents in various industries for the removal of toxic pollutants, ions, and non-biodegradable wastewaters due to its low cost and excellent adsorption capacity [48]. Adsorbents for the removal of heavy metal ions from various sources have been developed using both industrial and agricultural waste materials, including steel slag, fly ash from power plants, coffee grounds, walnut shells, and rice husk ash [49]. These adsorbents are quite affordable, which makes the process more sustainable. Many researchers have focused on the application of different modified adsorbents and natural adsorbents for chromium remediation, e.g., activated carbon, carbon nanotubes, clay, sand, and volcanic rocks such as pumice and scoria [48]. Similarly, using an adsorbent can also remove inorganic and organic pollutants present in the effluent. Along with all the advantages of absorption technology, there are some drawbacks. It has poor selectivity, low adsorption capacity, and difficult recovery.

1.3.2 Chemical Precipitation

Precipitation is a process in which pollutants are isolated from the solution as sediment (precipitated form). Then the sediment is separated from the solution by filtration, centrifugation,

or settling [7]. The precipitate forms reduce the bioavailability of metals, which is the result of complex formation between the precipitation agent and heavy metal ions. Chemical precipitation is considered an effective method for the removal of heavy metals from industrial wastewater [7,50]. It is used mainly for the removal of metallic cations. It can also be used to remove anions like phosphate, cyanide, and fluoride, as well as organic molecules like phenols and aromatic amines. These process can also be used for water softening, oil and grease removal from emulsified solutions, heavy metal removal from metal plating wastes, and phosphate removal from washwaters and other wastewater [50]. Sulfide and hydroxide precipitation are two common types of chemical precipitation techniques [51]. For hydroxide precipitation, calcium carbonate, calcium oxide (quicklime), calcium hydroxide (slaked lime), sodium hydroxide, sodium carbonate (soda ash), and ammonium hydroxide are used as precipitants to precipitate heavy metals from the solution [52,53]. A variety of precipitants, including sodium sulfide (Na_2S), sodium hydrosulfide (NaHS), calcium sulfide (CaS), barium sulfide (BaS), iron sulfide (FeS), ammonium sulfide ($(\text{NH}_4)_2\text{S}$), and sodium thiosulfate ($\text{Na}_2\text{S}_2\text{O}_3$), can be used to precipitate metal sulfides [54]. The mechanism of heavy metal removal by precipitation of metal hydroxides and metal sulfide is shown in eqn. 1 and eqn. 2 [55]:



Where M represents metal. An advantage of precipitation methods is that they can effectively separate and concentrate pollutants from complex matrixes, such as biological fluids, soil, or wastewater. The pollutants can be easily precipitated by choosing the suitable precipitating agent and conditions. This can simplify the subsequent steps of analysis, such as filtration,

centrifugation, or chromatography, and reduce the interference and contamination from the matrix. One of the main disadvantages of precipitation methods is that they can be affected by several factors that influence the solubility and stability of the pollutants, such as temperature, pH, ionic strength, and presence of the impurities. These factors can cause variations in the yield and purity of the precipitate. Other drawbacks are huge sludge production, slow metal precipitation, poor settling, the aggregation of metal precipitates, and the long-term environmental impacts of sludge disposal [56].

1.3.3 Membrane Filtration

Nowadays, membrane technologies are becoming more frequently used for the treatment of inorganic effluent. It has the ability to remove inorganic contaminants such as heavy metals, suspended solids, and organic compounds. Basically, a membrane is a barrier that separates two phases from each other by restricting the movement of components through it in a selective manner [57]. Membrane filtration needs a driving force (pressure, concentration, or electrical potential gradients) in order to separate the desired components, which are governed by the membrane's pore size [58]. According to their driving forces, membrane processes can be classified as microfiltration (MF), ultrafiltration (UF), nanofiltration (NF), reverse osmosis (RO), and forward osmosis (FO) [59]. UF and MF membranes are both used for pretreatment to increase the efficiency of the NF and RO processes. The MF process is based on the use of membranes with a symmetrical porous structure that permit the separation of particles with pore sizes ranging from 50 to 500 nm. Using a permeable membrane, UF can separate heavy metals, macromolecules, and suspended solids from inorganic solutions based on the pore size (5–20 nm) of the separating compounds. With a metal concentration ranging from 10 to 112 mg/L at pH ranging from 5 to 9.5 and at 2 to 5 bar of pressure, UF can achieve more than 90% of removal efficiency under certain membrane

conditions. Nanofiltration is used to remove solutes whose size is about or less than 2 nm [58–60]. Among the pressure driven membrane processes, RO is highly known for its efficiency in separating small particles. Osmosis is a biophysical phenomenon occurring commonly in biologic systems in which cells in fluid compartments are separated by semipermeable membranes. Osmosis describes the diffusion of the solvent through a semipermeable membrane. A semipermeable membrane has small pores that block contaminants but allow water molecules to flow through. Thus, the pressure-driven separation process RO employs a semipermeable membrane (pore size 0.5–1.5 nm, pressure 20–70 bar) to allow only smaller molecules to pass [60,61]. Using the RO separation process, several heavy metal ions, including Ni^{2+} , Cr^{6+} , and Cu^{2+} can be removed from the electroplating effluent. RO and UF techniques have been applied to the recovery of Cr from tannery wastewaters; RO maintained a pH of neutral, and RO was able to recover nearly 99% of the Cr. Since RO involves a diffusive mechanism, the separation efficiency depends on the solute concentration, pressure, and water flow rate. Recently, RO has been used to purify industrial wastewaters from coster-field mining operations located in Victoria, Australia, with mean extraction efficiencies of 10%, 48%, 82%, 66%, and 95% for Fe^{3+} , Zn^{2+} , Ni^{2+} , As^{3+} , and Sb^{3+} , respectively [62]. The biggest problem with the RO process is membrane fouling and degradation. Moreover, in the RO process, cleaning agents or inhibitors, pH adjustment, or mineralization are also needed. Reverse osmosis requires a high total cost of production for water treatment. FO is a natural osmosis process where water molecules are drawn from one solution to another through a semipermeable membrane. In this case, a highly concentrated draw solution is used to provide a concentration gradient to draw water molecules from the feed solution. FO does not require as much pressure as RO; thus, it is energy-saving. Nevertheless, there are many

drawbacks to FO, including draw solution re-concentration, membrane selection challenges, and internal and external concentration polarization [63,64].

1.3.4 Coagulation and Flocculation

Coagulation and flocculation play a dominant role in many water and wastewater systems. Basically, flocculation and coagulation are commonly applied methods in water treatment to remove suspended solids through a technique that destabilizes the suspended particles in aqueous solutions. The difference between the two is that coagulation is the incorporation of coagulant in solution to destabilize a stabilized charged particle, and flocculation is the settling of coagulated particles [65]. In conventional chemical coagulation, iron and aluminum coagulants are used. The most common aluminum coagulants are aluminum sulfate, aluminum chloride, and sodium aluminate. Iron coagulants include ferrous sulfate, ferric sulfate, ferric chloride sulfate, and ferric chloride [66–68]. Also, as coagulants, crushed seeds have been used for drinking water treatment since ancient times. To treat wastewater containing metals like Zn(II) and Cr(VI), polymeric ferric sulfate (PFS) is used as a coagulant [69]. Traditionally, coagulation treatment has been utilized in water treatment to decrease turbidity, color and remove pathogens. The coagulation–flocculation process has some advantages, like ease of operation and cost-effectiveness, but the process produces a large quantity of sludge and is a relatively time consuming process.

1.3.5 Ion Exchange

Ion exchange is the process through which ions in solution are transferred to a solid matrix, which in turn releases ions of a different type but of the same polarity. In other words the ions in solutions are replaced by different ions originally present in the solid. Organic or inorganic matrices with ionic functional groups are present in ion exchange materials. The most often used materials for ion exchange are organic resins. According to their functional groups, ion exchange

resins can be classified as cationic exchange resin (which have positively charged mobile ions available for exchange), anion exchange resin (whose exchangeable ions are negatively charged), and chelating exchange resin. In addition, basic organic polymers are used to produce both anion and cation resins [70–72]. The ion exchange process for removing heavy metals from waste water can be explained by the following eqn. 3:



where M^- is fixed anion, EC^+ is the exchange cation (Na^+ , H^+ frequently used exchange cations), and WC^+ is the exchange cation [73]. Different types of ion exchange resins, such as zeolite, clays, amberlite, tripoli, diaion, chelex, etc., were investigated for metals cation removal [74,75]. Nowadays, ion exchange resins have been used by numerous researchers to study the removal of heavy metal ions because of their ease of use and affordability. Ion exchange resins ZIF-67 is used to treat wastewater containing Cr(VI) [76]. Chelating resins are employed in the removal of metal ions because of their strong adsorption capabilities, durability, and selectivity [77]. Though the ion exchange process has many advantages like recovery of metal value, selectivity, less sludge volume produced, it also has some drawbacks. Surface water treatment requires pretreatment, and a huge amount of contaminants are usually found. Disposing of these pollutants is quite expensive.

1.3.6 Electrochemical Treatment

Electrochemical methods are widely used for the treatment of domestic waste water as well as industrial waste water. Disinfection and the removal of pollutants, harmful ions, and heavy metals are the main concerns in the electrochemical waste water treatment methods. Generally, pollutants are degraded or reduced in the electrochemical process through either direct or indirect oxidation. In direct oxidation, oxidation takes place at the anode (positive side), where electrons

migrate to the cathode (negative side), at which the reduction process occurs. These two chemical reactions are called redox (reduction-oxidation), which purify water by removing metal. In indirect oxidation, no direct electrons transfer between the anode and the organic matter. It works on the principle that the oxidization of pollutants is done in the bulk of the solution. Chlorine is the most active species in this category. Ozone and hydrogen peroxide are also strong oxidants [78,79]. The electrochemical processes are primarily classified into electro-reduction (ER), electro-coagulation (EC), electro-flotation (EF), and electro-oxidation (EO). The ER method, also known as electrodeposition and electroplating, is a process in which targeted atoms or molecules are deposited on the surface of the cathode due to the passage of electric current in the electrochemical system [60]. Among the electrochemical methods, electrocoagulation (EC) is the most commonly used method for wastewater treatment because it combines the advantages of coagulation, flotation, and electrochemistry. The theory behind coagulation/flocculation and (EC) is basically the same. The removal of pollutants from wastewater is the target of both processes [80]. EC treatment employs soluble anodes consisting of coagulating metals like iron and aluminum. These anodes dissolve electrolytically to produce Al^{3+} and Fe^{2+} ions, which are then hydrolyzed to form polymeric hydroxides. Coagulation occurs when these metal cations combine with the negative particles carried toward the anode by electrophoretic motion. This process involves a number of destabilizing processes as well as simultaneously occurring beneficial impacts, such as pH change and the generation of hydrogen bubbles. So the EC method of removing chromium is a rather complicated procedure. Multiple steps like chemical, physiochemical, and electrochemical steps, are involved in chromium removal. Briefly, oxidation of iron at the cathode, reduction of chromium at the anode, chemical reduction of chromium by reductant metal ions, chromium adsorption, precipitation and coagulation of the hydroxides formed, co-precipitation, electro-

flotation, etc [81]. EO methods are practiced for wastewater treatment to remove pollutants. In this process, electric current is applied through electrodes in the wastewater to form strong oxidizing species like $\cdot\text{OH}$. Consequently, oxidizing agents generated from the anode directly oxidize electron-rich organic contaminants on the anode surface or indirectly oxidize them [82].

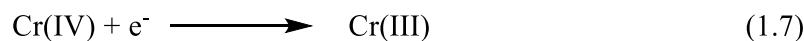
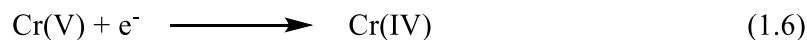
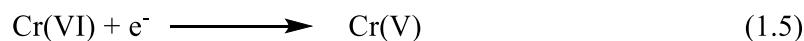
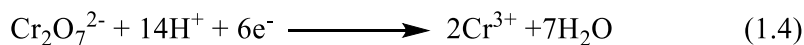
1.3.7 Bioremediation

Bioremediation is also a method for pollution treatment, it is a sustainable, affordable, and safe remediation technique. It involves application of naturally occurring microorganisms (bacteria, fungi, and plants) to biodegrade and neutralize hazardous pollutants. Bioremediation can either be done in situ or ex situ. In in situ techniques, contaminated soil or water is treated on site with the lowest disturbance to the encompassing surroundings. In contrast, in ex situ techniques, contaminants are treated in an alternative controlled environment from the contaminated site by evacuation or pumping out [12,83]. Microorganisms are suitable for removing impurities since they have proteins that allow them to use natural pollutants as food. A variety of enzymes are secreted by different microorganisms, and these enzymes have the ability to degrade environmentally hazardous chemical substances. Generally, bioremediation has been applied in multiple sections, such as the treatment of waste water and the removal of hazardous compounds. The viability of this method depends on the type of toxins, physical environment and microbial communities. For bioremediation to be beneficial, microorganisms must attack the contaminants enzymatically and transform them into harmless compounds. Since, bioremediation can be effective in environments that support microbial growth and activity, its application often involves the influence of environmental parameters to promote microbial growth and degradation [84]. Various microbial remediation techniques, such as biosorption, bioaccumulation, biotransformation, and bioleaching, have been reported for the removal of chromium and other

heavy metals from industrial wastewater [85]. Basically, microorganisms possess a variety of anionic structures on their cell surfaces, including hydroxyl, phosphoryl, carboxyl, alcohol, amine, thioether, thiol, ester, sulfonate, and sulfhydryl groups. The toxic heavy metal ions get attached to the surface ligand of the cell. Then, the metal ligand complex formed at the surface of the cell is transported inside the cell by the transporter protein. Finally, transported complexes intracellularly interact with metalbinding proteins (such as metallothionein and phytochelatins), where precipitation, methylation, and other processes take place. Tanneries are mainly responsible for the release of huge amounts of chromium into the environment. Pentachlorophenol and related biocides used in the leather tanning processes are refractive for the growth of microorganisms and they also reduce the removal of chromium from tannery effluent [86]. Also, various bacteria naturally present in soil and groundwater, like *Bacillus* sp., *Arthrobacter* sp., *Microbacterium* sp., *Providencia* sp., and *Serratia* sp., can reduce Cr(VI) to Cr(III) by accepting electrons via bacterial enzymatic processes or indirectly via by-products of bacterial activity such as hydrogen sulfide and Fe(II) [87,88]. Another category of bioremediation process is phytoremediation. Phytoremediation is a process where biological components of the environment (plants) are used to remove heavy metals, organic pollutants, and radionuclides. This can be justified by the fact that plants absorb contaminants from the soil and water interface as their nutrients [44]. This process can be categorized as phytostabilization, phytoextraction, phytovolatilization, phytodegradation, phytostimulation, etc., to degrade, remove, or immobilize the pollutants [84]. Despite its many advantages, like other technologies, bioremediation has its limitations. The efficiency of bioremediation is lower than that of physical and chemical materials, and it also takes a long time to remove pollutants.

1.3.8 Photocatalytic Remediation

Photocatalysis has been found to be one of the most effective techniques to reduce and degrade contaminants. This is a feasible alternative to the methods mentioned above. The term ‘photocatalysis’ appeared for the first time in the early years, in 1911. It is a combination of Greek words like photo, “phos”, which means light, and catalysis, “katalyo”, which means to decompose or degrade. Thus, it is a phenomenon that combines photochemistry and catalysis [89,90]. In simple terms, photocatalysis is the acceleration of a photo-generated electron in the presence of a catalyst. Generally, photocatalysts have a semiconductor structure. Hence, when light is present, photocatalysts absorb the photons efficiently, causing the active electron to shift to the conduction band, resulting in an apposite hole in the valence band. Photocatalysis involves at least two simultaneous reactions: oxidation from photogenerated holes produced in the valence band and reduction from photogenerated electrons in the conduction band. Therefore, this process can be used to oxidize organic or inorganic pollutants or reduce heavy metals due to the redox system generated on the CB and VB of a photocatalyst [91–93]. In the process of treating heavy metals, the CB and VB electrons and holes can be transferred to the semiconductor's surface and undergo successive reduction and oxidation reactions, which are embodied in the conversion of different valence states of heavy metals. In the case of heavy metal Cr(VI) reduction, electrons are migrated directly to adsorbed Cr(VI) or even at the boundary of the photocatalyst surface. Electron transfer from CB to Cr(VI) can be done in two ways. In one way, Cr(VI) can be reduced directly to Cr(III) by transferring three electrons from the photocatalyst CB in a single step. Alternatively, Cr(VI) is reduced by single electron transfer, generating Cr(V) and Cr(IV) as intermediates. Moreover, some literature reports that photogenerated superoxide in the CB of the photocatalyst can take part in the reduction of Cr(VI) to Cr(III) reactions [24,94].



Different types of visible light and UV light driven photocatalysts have been used to photocatalytically reduce heavy metal such as TiO_2 , ZnO , Cu_2O , WO_3 , Fe_2O_3 , SnO_2 , ZnFe_2O_4 , CoFe_2O_4 , etc. Again, a polymeric semiconductor, namely graphitic carbon nitride ($\text{g-C}_3\text{N}_4$), has been reported to be a hopeful candidate due to its facile synthesis, unique structure, high physicochemical stability, and “earth-abundant” nature [95]. The widely used practiced semiconductor photocatalysts are listed in Table 1.2.

Table 1.2 The widely practiced semiconductor photocatalysts [96,97]:

Semiconductor photocatalyst	Band gap (eV)	Light response	Wavelength (~ nm)
TiO_2	3.2	UV	387
ZnO	3.2	UV	387
Fe_2O_3	2.1	UV-Vis	565
ZnFe_2O_4	1.92	UV-Vis	645
WO_3	2.6	Visible	443
ZnS	3.7	UV	335
CdS	2.5	Visible	496
Cu_2O	2.2	UV-Vis	563
$\text{g-C}_3\text{N}_4$	2.7	UV-Vis	459

Heterogeneous photocatalysis has a number of benefits, but also disadvantages. The benefits and drawbacks of heterogeneous photocatalysis are illustrated in the Figure 1.5. There are several approaches to the modification of single semiconductors, such as elemental doping, heterojunction construction, surface modification, etc., that have been utilized to minimize the drawbacks of photocatalysis efficacy.

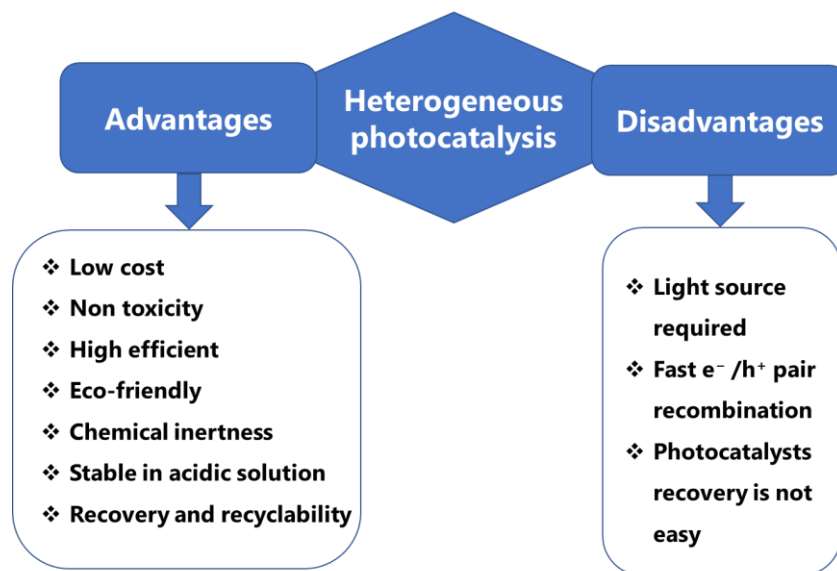


Figure 1.5 Schematic diagram for the advantages and disadvantages of photocatalytic remediation methods.

1.3.8.1 The Principle of Photocatalytic Reaction Mechanism

The basic principle of photocatalytic reduction or degradation is to produce an electron hole pair upon excitation by light of a specific wavelength, which can conduct a redox reaction on the photocatalyst surface. The photocatalytic reaction mechanism mainly includes the following steps [98]:

1. A photocatalyst is induced by light ($h\nu$) equal to or greater than its band gap energy. The valence band (VB) electron absorbs photon energy more than its band gap and transfers

from the VB to the conduction band (CB), generating an unfilled vacancy known as a hole in the VB.

2. The photogenerated electron-hole pairs have a strong tendency toward mutual extinction and radioactive recombination. And the remaining electron-hole pairs are moved to the surface of the photocatalyst.
3. Charge species such as electrons and holes undergo reduction or oxidation reactions (redox reactions) on the surface of the photocatalyst.

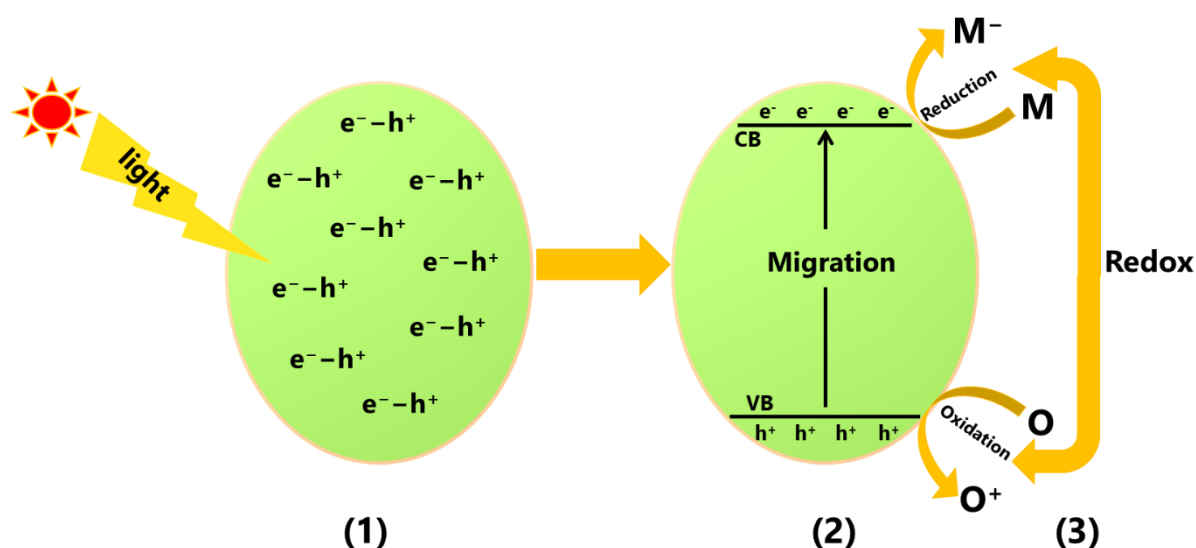
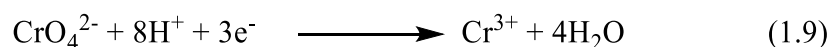
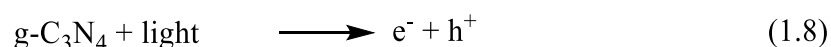


Figure 1.6 A general mechanism presenting photocatalytic reduction or degradation of pollutants. M: compounds in reductive reactions; and O: compounds in oxidative reactions.

1.3.8.2 Photocatalytic Reduction Mechanism

The above process is also followed for the photocatalytic reduction of hazardous heavy metals by various photocatalyst under light irradiation. Typically, when a UV/visible light falls on a photocatalyst with a photonic energy ($h\nu$) higher than the excitation energy (E_g), it induces the

excitation of electrons from the VB to the CB, resulting in holes in the VB and highly active electrons in the CB. These electron-hole pairs are migrated to the surface of photocatalyst to undergo redox reactions. The photocatalytic reduction occurs when the redox potential of heavy metals is greater than that of the conduction band of the applied photocatalyst. Meanwhile, the holes combine with water and generate hydroxyl radicals [99]. A possible reaction process for the photocatalytic reduction of heavy metals is presented in the following equations: photocatalyst (e.g., g-C₃N₄): heavy metal (e.g., Cr(VI)).



However, the photo-induced holes have no role in the reduction of heavy metals. But the hydroxyl radicals that are produced from the holes through water oxidation, acting as a strong oxidizing agent, can reduce pollutants. In addition, if electron-hole recombination occurs in the reaction process, it slows down the photocatalytic reduction of heavy metal.

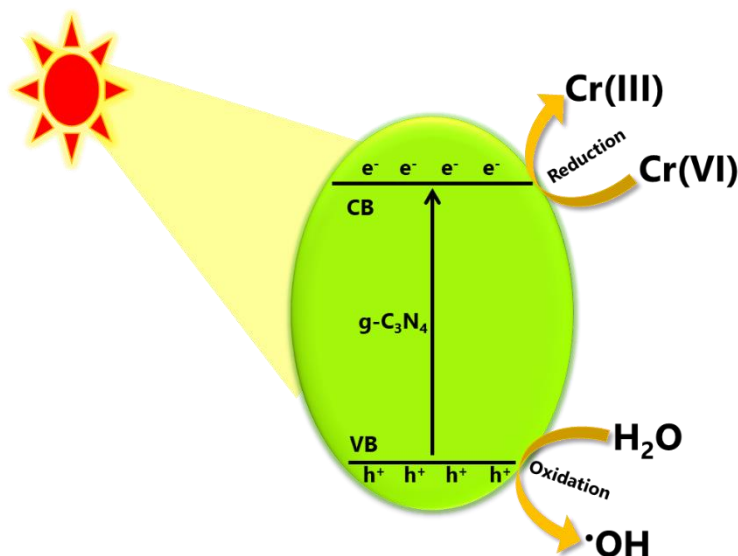


Figure 1.7 Schematic diagram of possible photocatalytic mechanism for the reduction of Cr(VI) by g-C₃N₄.

1.3.8.3 Photocatalytic Degradation Mechanism

The photocatalyst is also used for the degradation of organic pollutants. When a photocatalyst (e.g., g-C₃N₄) is induced by UV or visible light, the electron in the VB absorbs photon energy and transfers it to the CB. These conduction band electrons react with oxygen present all over the surface of g-C₃N₄ to produce superoxide radical anions ($\bullet\text{O}^{2-}$). Therefore, $\bullet\text{O}^{2-}$ radicals are the major and effective active species for the degradation of organic pollutants. On the other hand, the VB holes react with water and form hydroxyl radicals ($\bullet\text{OH}$) from water or hydroxyl ions in water. Hydroxyl radicals ($\bullet\text{OH}$), as strong oxidizing agents, degrade organic pollutants into intermediate compounds, resulting in the mineralization of pollutants into harmless substances such as H₂O and CO₂ [100]. The related photocatalytic reactions for the degradation of organic pollutants can be expressed as the following reactions:

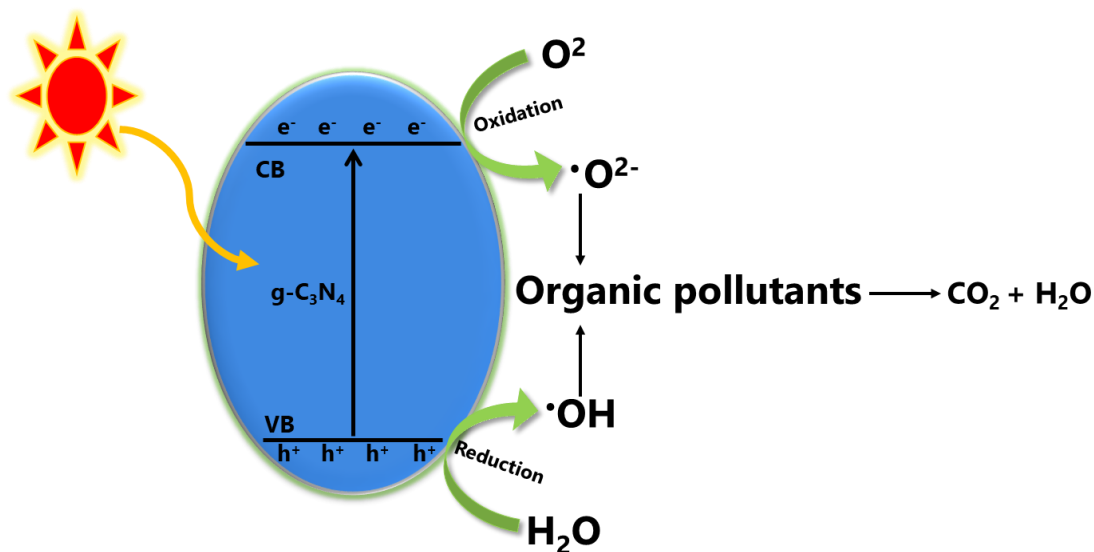
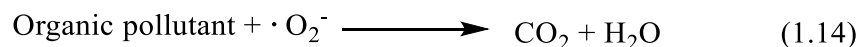
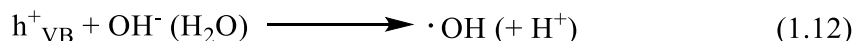
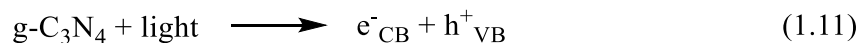


Figure 1.8 Schematic diagram of possible photocatalytic mechanism for the degradation of organic pollutant by g-C₃N₄ photocatalyst under light irradiation.

1.3.8.4 Improvement of photocatalytic Performance

Pure photocatalysts have poor photocatalytic performance because of the rapid recombination of photo-induced electrons and holes. Therefore, various strategies can be adopted to mitigate the constraints. One of them is the introduction of hole scavengers, and how it improves photocatalytic activity is explained here. Several hole scavengers such as small molecular organic acids, namely ethylenediamine tetraacetic acid (EDTA), formic acid, tartaric acid, citric acid, etc., can enhance the photocatalytic activity of photocatalysts. These hole scavengers consume holes produced in the VB to rapidly produce intermediate compounds. These compounds are then

converted to H₂O, CO₂, and mineral acids [101]. As a result, the recombination of electron-hole pairs slows down. Hence, CB electrons can contribute to the reduction of toxic heavy metals. A general mechanism for the improvement of photocatalytic reduction of toxic heavy metals (e.g., Cr(VI)) and photocatalyst g-C₃N₄ is shown in Figure 1.9.

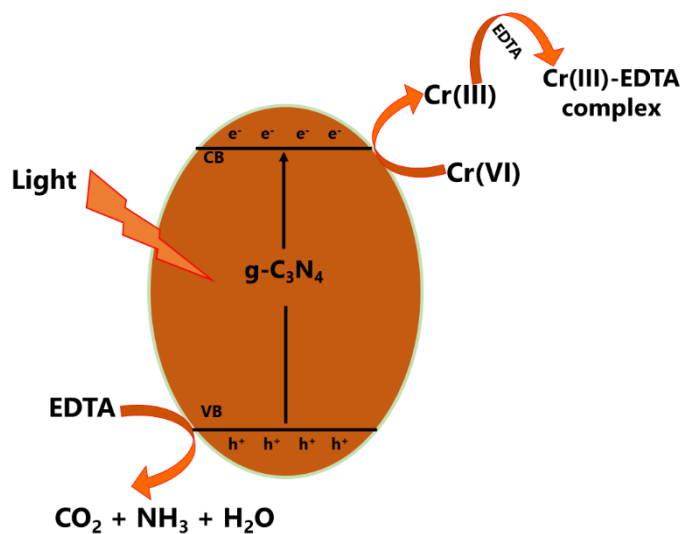
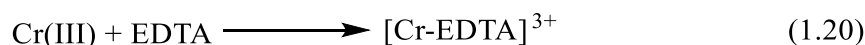
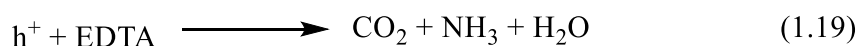
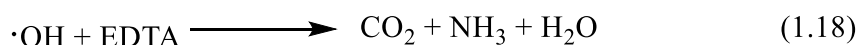
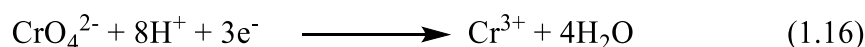
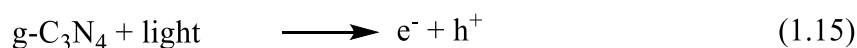


Figure 1.9 Schematic diagram of possible photocatalytic mechanism for the reduction of Cr(VI) by g-C₃N₄ in presence of EDTA.

1.4 Graphitic Carbon Nitride (g-C₃N₄)

Graphitic Carbon Nitride (g-C₃N₄) is a metal free highly active photocatalyst. It was first synthesized by Berzelius and named by Liebig in 1834. Liebig named the polymeric derivative g-C₃N₄ as “melon”, which is a linear polymer of interconnected tri-s-triazine through secondary nitrogen [102,103]. Surprisingly, the enormous potential of this polymer-like substance was not wholly recognized until recent decades. In the nineties, Liu and Cohen (1993) predicted a diamond-like structure from the fabrication of really hard carbon nitride. It has been reported about seven phases of C₃N₄, which are g-o-triazine, g-h-heptazine, g-h-triazine, pseudo cubic C₃N₄, cubic C₃N₄, α -C₃N₄, and β -C₃N₄ [104]. And around 2006, g-C₃N₄ began to be utilized in heterogeneous catalysis [105]. Wang et al. (2009) first reported the use of g-C₃N₄ as a metal-free conjugated semiconductor photocatalyst to obtain H₂ from water [106]. After that, researchers focused on polymeric conjugated semiconductor photocatalysts rather than inorganic ones. Among the carbon nitride materials, g-C₃N₄ has generated excitement in the research community because of its easy synthesis, low cost, pleasing electronic band structure, high physicochemical stability, and “earth-abundant element” features [107–110]. A number of methods, including chemical vapor deposition, solvothermal method, plasma sputtering reaction deposition, and solid-state reactions have been reported for the synthesis of g-C₃N₄. These traditional methods require strict synthesized conditions, such as higher pressure, higher temperature, longer pretreatment times, and limited access to expensive instruments. Therefore, thermal polycondensation has emerged as the most widely used technique for the synthesis of g-C₃N₄ because of its simple synthesis process, high yield, and cost effectiveness. As g-C₃N₄ only contains earth-abundant elements (carbon and nitrogen), it can be prepared with accessible raw materials at a low cost. Hence, nitrogen-rich

precursors, including urea, thiourea, cyanamide, dicyanamide, and melamine, etc., are mainly used for the fabrication of $g\text{-C}_3\text{N}_4$ (Figure 1.10) [111,112].

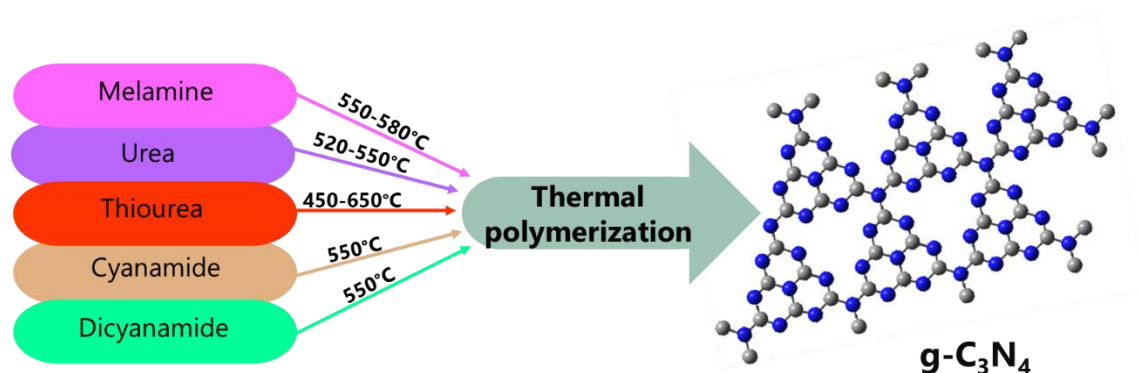


Figure 1.10 The $g\text{-C}_3\text{N}_4$ synthesis via thermal polymerization of different precursors. Adapted from Li et al. (2019).

$g\text{-C}_3\text{N}_4$ has bandgap energy, also referred to as the void region and it ranges from the top of the filled VB to the bottom of the empty CB. In the beginning, the absorption of a photon with energy equal to or greater than the bandgap results in the excitation of an electron from the VB to CB, leaving an empty state behind, which is a positive hole. The charge carriers in the excited states, once spatially separated and shifted to the surface of $g\text{-C}_3\text{N}_4$, in order to develop the reduction and oxidation processes that lead to the photocatalytic conversion of reactant molecules (Figure 1.11). The actual reaction sites may be located either directly on the $g\text{-C}_3\text{N}_4$ surface, where the photoexcitation occurs, or across the interface of another semiconductor or cocatalyst [113]. Accordingly, the primary role of the $g\text{-C}_3\text{N}_4$ in photocatalysis is to absorb an incident photon, produce electron hole pairs and transfer them to its surface or to a cocatalyst. Indeed, $g\text{-C}_3\text{N}_4$ is chemically active only when the photoinduced electron hole pair is consumed simultaneously before recombination occurs in a fraction of a nanosecond. The band-gap excitation and formation

of free charge carriers an electron and a hole are followed by a few deexcitation pathways (Figure 1.11).

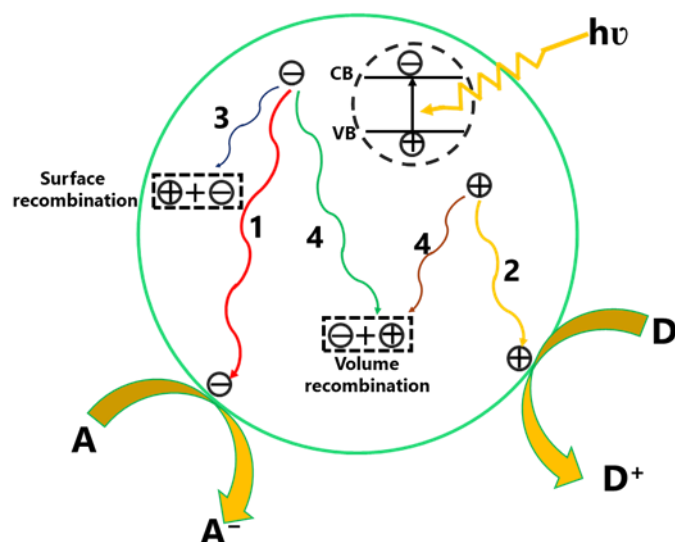


Figure 1.11 Schematic illustration of photoexcited electron–hole pairs in g-C₃N₄ with possible decay pathways. A and D denote electron acceptor and electron donor.

It is notable that the successful migration of charge carriers to the acceptor molecules, which leads to the desired redox reactions (pathways 1 and 2, respectively), also competes with the recombination processes [112]. For instance, the recombination process can take place via two different paths, as follows: (1) the carriers can recombine with their counterparts of opposite charge trapped on the surface (surface recombination), and (2) the recombination of two carriers can occur in the bulk of g-C₃N₄ pathway 4 (volume recombination) [114]. These recombination processes are the drawbacks of photocatalytic efficacy. When the recombination process occurs, the excited electrons revert to the VB, dissipating the energy as heat without reacting with the adsorbed species

on the surface of g-C₃N₄. There are also some disadvantages to g-C₃N₄, which are given below [115,116].

- Small surface areas/ active sides
- High surface inertness
- Insufficient light harvesting
- Slow reaction kinetics
- Moderate oxidation ability
- Low carrier mobility

1.4.1 Modification of g-C₃N₄

In simple terms, a photocatalytic reaction on a semiconductor includes at least five main steps: i) light absorption by the semiconductor, ii) formation of photogenerated electron–hole pairs, iii) migration and recombination of the photogenerated electron–hole pairs, iv) adsorption of reactants and desorption of products, and v) occurrence of redox reactions on the semiconductor surface. Among them, the recombination of electron–hole pairs plays a negative role in the photocatalytic processes [117,118]. During photocatalytic reaction, the photogenerated electron–hole pairs can either transfer to the photocatalyst surface and initiate redox reactions. To overcome this problem modification is necessary. Modification is useful technique to enhance the physiochemical characteristics of semiconductor for various application. In this work we will discuss modification of g-C₃N₄. As shown in Figure 1.12, the fabrication of g-C₃N₄ can usually be classified into a few categories.

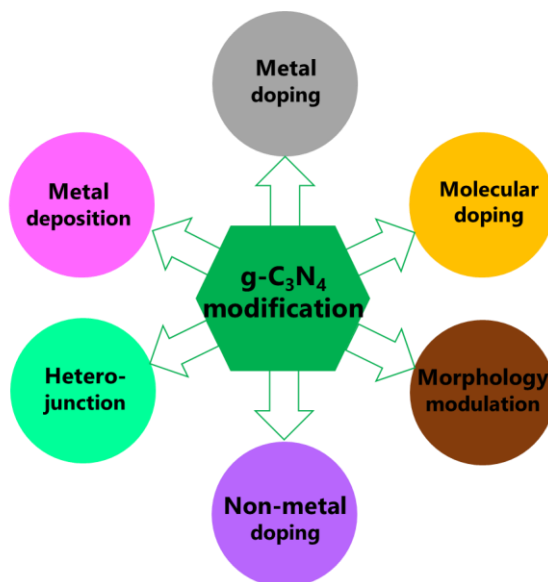


Figure 1.12 Common modification methods of g-C₃N₄.

1.4.1.1 Metal doping

An intended introduction of metal atoms into the photocatalyst (g-C₃N₄) crystal lattice in order to modify its optical, electrical, or catalytic properties is known as elemental doping. It is an efficient method for modifying the band structure of photocatalysts, expanding the light absorption zone, and improving charge separation. It is also a promising method to enhance the photocatalytic activity and performance of g-C₃N₄ for multiple applications such as water splitting, pollutant reduction and degradation, and hydrogen production. There are two main types of elemental doping: namely metal doping and non-metal doping [112,113]. For metal doping, different metals can be used as dopants in g-C₃N₄, including transition metals such as iron (Fe), cobalt (Co), nickel (Ni), platinum (Pt), and noble metals like silver (Ag), gold (Au), and palladium (Pd). Metal doping may enhance the delocalization of π -conjugated electrons in g-C₃N₄ and accelerate carrier mobility, lifetime, and photoelectronic separation. Additionally, it can improve the photocatalytic performance of g-C₃N₄ by reducing its band gap and increasing its optical absorption capacity,

particularly in visible light [119,120]. Generally, metal dopants act as electron traps, and the simultaneous addition of dopants improves the photocatalytic performance of g-C₃N₄ by enhancing the separation of photogenerated electrons and holes and expanding the optical absorption region. Therefore, doping metallic elements with bare g-C₃N₄ is an effective method [121].

For example, the way in which noble metal (e.g., Ag) doping enhances the photocatalytic activity of g-C₃N₄ is described here. When UV/visible light is irradiated on the g-C₃N₄, it efficiently absorbs photons and produces VB holes (h^+) and CB electrons (e^-). Therefore, h^+ remains at the VB of the photocatalyst, and e^- is moved to the CB of the photocatalyst. If the Ag is doped on the photocatalyst, it is situated between the photocatalyst valance and the conduction band. As a result, the CB electrons in the photocatalyst rapidly transfer to Ag because they can easily trap the electrons [122–124]. Therefore, the recombination rate of photogenerated e^-h^+ decreases while the life-time of photogenerated electrons increases

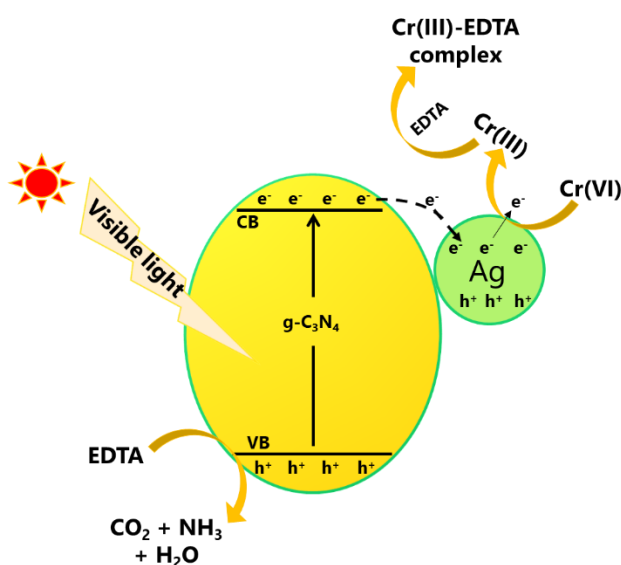


Figure 1.13 Schematic diagram of possible photocatalytic mechanism for the reduction of Cr(VI) by g-C₃N₄ by the introduction of Ag metal in the presence of EDTA.

Of note, Ag exhibits the surface plasmon resonance (SPR) effect, and the band structure of silver matches that of g-C₃N₄ [125,126]. When g-C₃N₄ is modified with Ag, a pair of electrons of N may readily move to the Ag outermost shell to form a rigid N-Ag bond, which would efficiently isolate the photogenerated e⁻-h⁺ [125].

1.4.1.2 Non-metal doping

Similar to metal doping, the non-metal could also be used to modify g-C₃N₄. Non-metal doping is the process of doping certain non-metal elements into the structural framework of g-C₃N₄. This changed the g-C₃N₄ photocatalyst's electronic and textural characteristics and enhanced the separation efficiency of photogenerated charge carriers, which in turn increased the photocatalytic performance [119,127]. Various non-metals such as halogens (F, Cl, Br, I), boron (B), oxygen (O), nitrogen (N), carbon (C), sulfur (S), and phosphorus (P) have been reported as dopants on g-C₃N₄ material [128]. This non-metal doping generally allows metal to tune the band structure, produce more active sites, and extend the absorption of visible irradiation. Non-metal elements have higher electronegativity and ionization energies apart from the metal-free characteristic. So they readily form covalent bonds with other substances by accepting electrons. Moreover, non-metal doping can play a role in reducing the effects of thermal changes in chemical states [117,127].

1.4.1.3 Metal deposition (co-catalyst)

A number of studies revealed that one of the potential ways to increase the photocatalytic activity was deposition of metal on pure g-C₃N₄ as co-catalyst. A Schottky junction forms at the interface between metal nanoparticles and g-C₃N₄ semiconductor when they come into contact because of the differing work function, which modifies the electron distribution on the semiconductor surface [119,129,130]. During photocatalytic processes, the primary role of metal is to receive photogenerated electrons from the CB of g-C₃N₄. Hence, the photocatalytic reaction ability of g-

C₃N₄ is enhanced by the reduction of electron hole pair recombination and the improvement of visible light absorption ability [119].

1.4.1.4 Molecular Doping

It has been demonstrated that doping organic small molecules into the g-C₃N₄ skeleton is a viable strategy for efficiently promoting the separation of photogenerated charge carriers in order to increase photocatalytic activity [131,132]. The band gaps of g-C₃N₄ can be narrowed by thermal co-polymerization of its aromatic co-monomers and precursors, extending its visible light absorption edge and improving solar usage. Through the chemical bonding effect, an organic small molecule with an aromatic ring can be introduced into the skeleton of bare g-C₃N₄, effectively regulating electronic band structure by modifying the hybridization and delocalization states of molecular orbitals to improve charge transfer and separation [131,133]. In the meantime, the aromatic doped ring organic small molecule exhibits a strong electron-withdrawing impact to cause a charge redistribution in the g-C₃N₄ plane, which helps to increase the effectiveness of photogenerated charge carrier separation [131,134,135].

Therefore, molecular doping of g-C₃N₄ can increase its photocatalytic activity by changing a number of its characteristics, including its wider visible light sensitivity, narrower bandgap, larger adsorption capacity, and better charge separation efficiency and transfer kinetics [131].

1.4.1.5 Heterojunction

A heterojunction is often the interface region of two different semiconductors with uneven band structures. Compared with the doping mentioned above, heterojunction of g-C₃N₄ with a suitable semiconductor is a better option to enhance the photocatalytic performance by optimizing the local electronic structure of g-C₃N₄. Especially through the construction of heterojunctions, charge separation efficiencies can be dramatically accelerated [136]. Various semiconductors form

heterojunctions with g-C₃N₄, such as carbon materials (grapheme, carbon nanotubes, fullerenes), metal oxides (TiO₂, SnO₂, Cu₂O, ZnO, NiFe₂O₄, Fe₂O₃), metal sulfides (CdS, ZnS, MoS₂), bismuth-based compounds (BiPO₄, BiVO₄, Bi₂WO₆), silver-based compounds (Ag₂O, Ag₃PO₄, Ag₃VO₄), and multi-element rare earth oxides (Zn₂GeO₄, SrTiO₃), etc [119,137–139].

The band alignment at the interface has a significant impact on the heterojunction's characteristics. The heterojunction can be classified into four categories based on the differences in band structure position and charge transfer mechanism between the two semiconductors: Type I, Type II, Type III, and the heterojunction Z-scheme (Figure 1.14) [140,141] . In the bare g-C₃N₄ photocatalytic system, excited electrons have a tendency to move from the conduction band (CB) to the valence band (VB) and recombine with the holes there. These tendencies hampered the photocatalytic reaction. Effective charge transfer on the interface between the two semiconductors can be achieved when a semiconductor with the suitable energy band structure is in close contact with g-C₃N₄. This can increase the material's stability and widen its light absorption range by facilitating the fast separation and transfer of photogenerated electron-hole pairs in space. In the case of type I heterojunction, the VB and CB positions of semiconductor A are more positive and negative, respectively, than the relevant energy bands of semiconductor B. Therefore, excited electrons and holes transfer to CB and VB of semiconductor B, which inhibits the fast separation of photoexcited electron hole pairs under light irradiation. The redox reaction also takes place on semiconductor B, which has a lower redox potential. This lowers the redox capacity of the materials. For Type II heterojunction, both VB and CB of semiconductor A are located above the CB of semiconductor B without crossing each other, i.e., the band gap does not overlap. This prevents the transfer and separation of photogenerated electron and hole pairs between semiconductors A and B. On the other hand, for type II heterojunctions, the CB and VB positions

of semiconductor A are higher than those of semiconductor B. Hence, the electrons in semiconductor A tend to move to the CB of semiconductor B, where the band position is more positive under light irradiation. This results in a spatial separation of charge carriers. Therefore, recombination of the electron-hole pair could be hampered, and the lifetime of the electron could be enhanced [119,140,142]. The Z-scheme heterojunction is similar to the Type II heterojunction regarding energy level position interleaving. The difference between Type II and Z-scheme heterojunction is in the charge transfer mechanism. Under light irradiation, CB electrons from semiconductor B can transfer directly to the VB of semiconductor A and neutralize holes there. As a result, the oxidizing power of holes increases, as does the reducing power of electrons [140,143].

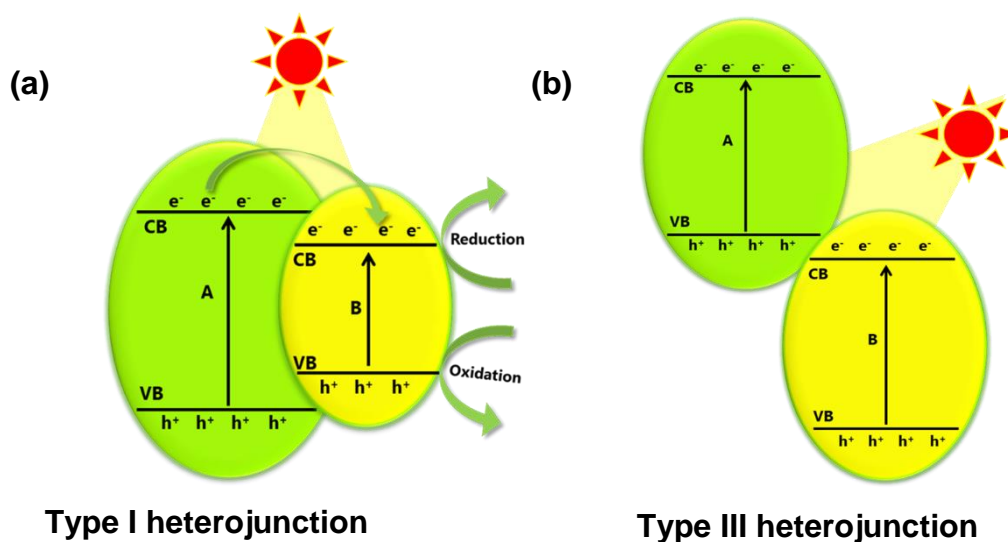


Figure 1.14 Charge transfer mechanism of (a) Type I, (b) Type III heterojunctions.

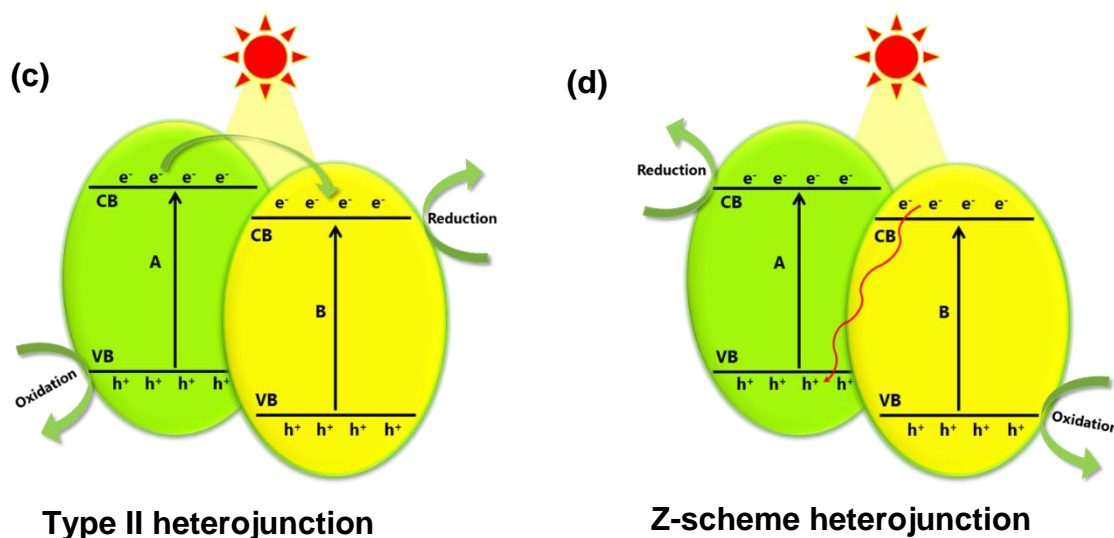


Figure 1.14 Charge transfer mechanism of (c) Type II, and (d) Z-scheme heterojunctions.

For example, the way in which second semiconductor (e.g., ZnO) introduction enhances the photocatalytic performance of g-C₃N₄ is described here. If the g-C₃N₄ is exposed to visible light, it absorbs photon energy and generates conduction band electrons and valance band holes. If the second semiconductor is doped on the g-C₃N₄, VB electrons of the g-C₃N₄ are transferred to the CB of ZnO through the interfacial charge transfer (IFCT) mechanism until their fermi-level energies are equal [144,145]. Furthermore, the photogenerated CB electrons of g-C₃N₄ rapidly moved to the CB of ZnO. These accumulated electrons on the CB of ZnO can readily reduce toxic heavy metals (e.g., Cr(VI)) [146].

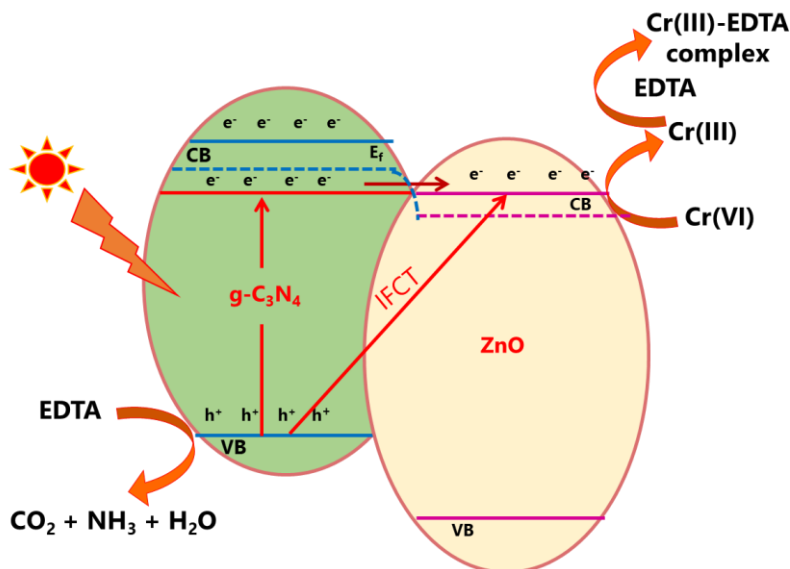


Figure 1.15 Charge transfer in the conventional Type II $g\text{-C}_3\text{N}_4$ based heterojunction systems constructed by coupling $g\text{-C}_3\text{N}_4$ to a second semiconductor ZnO, for the reduction of Cr(VI) in the presence of EDTA.

Notably, ZnO is a potential photocatalyst due to its low cost, high oxidative capability, non-toxicity, and appropriate band position for redox behavior [147]. In addition, compared to other oxides, ZnO may be simpler to synthesize using a calcination technique like $g\text{-C}_3\text{N}_4$ [148].

1.4.1.6 Morphology Modulation

Morphological control has emerged as a useful technique for improving the optical and chemical properties of $g\text{-C}_3\text{N}_4$ in order to achieve optimal photocatalytic properties. In general, the photocatalytic process usually takes place on the surface of the photocatalyst. By modifying the band structure, it is possible to obtain the specific surface area and structure of $g\text{-C}_3\text{N}_4$. Since then, the electron hole transfer efficiency of $g\text{-C}_3\text{N}_4$ has significantly increased [149]. Thus, numerous investigations tried to improve the morphology of $g\text{-C}_3\text{N}_4$ by controlling the techniques

of preparation. Currently, the reported $\text{g-C}_3\text{N}_4$ can be classified into the subsequent groups according to its dimensions [150,151]:

1. 0-dimensional $\text{g-C}_3\text{N}_4$ (e.g., $\text{g-C}_3\text{N}_4$ quantum dots)
2. 1-dimensional $\text{g-C}_3\text{N}_4$ (e.g., $\text{g-C}_3\text{N}_4$ tubes)
3. 2-dimensional $\text{g-C}_3\text{N}_4$ (e.g., $\text{g-C}_3\text{N}_4$ nanosheets)
4. 3-dimensional $\text{g-C}_3\text{N}_4$ (e.g., nanoporous $\text{g-C}_3\text{N}_4$ microspheres)

1.5 Objectives of the Research

● General Objectives

To fabricate and characterize the ZnO/g-C₃N₄ composites and Ag doped g-C₃N₄, and evaluate the application of prepared semiconductors for the photocatalytic reduction of Cr(VI).

● Specific Objectives

- To fabricate the different types of ZnO/g-C₃N₄ composites by simple calcination technique and characterize using various analytical technique such as TGA, FTIR, XRD, XPS, SEM, TEM, UV-Vis DRS, PL, EIS and nitrogen adsorption and desorption isotherm.
- To fabricate the different types of Ag doped g-C₃N₄ by simple calcination technique and characterize using various analytical technique such as TGA, FTIR, XRD, XPS, SEM, TEM, UV-Vis DRS, PL, EIS, Mott-Schottky analysis, and nitrogen adsorption and desorption isotherm.
- To investigate the photocatalytic Cr(VI) reduction under visible light radiation using prepared ZnO/g-C₃N₄ composites and Ag doped g-C₃N₄.
- To study the kinetic parameters of photocatalytic Cr(VI) reduction reactions using both ZnO/g-C₃N₄ composites and Ag doped g-C₃N₄.
- To investigate the stability and reusability of the prepared semiconductors on photocatalytic Cr(VI) reduction reactions.
- To propose the respective photocatalytic degradation and adsorption mechanism.

1.6 References

1. Worku, Z.; Tibebu, S.; Nure, J.F.; Tibebu, S.; Moyo, W.; Ambaye, A.D.; Nkambule, T.T.I. Adsorption of Chromium from Electroplating Wastewater Using Activated Carbon Developed from Water Hyacinth. *BMC Chem.* **2023**, *17*, 85, doi:10.1186/s13065-023-00993-4.
2. Long, Z.; Huang, Y.; Zhang, W.; Shi, Z.; Yu, D.; Chen, Y.; Liu, C.; Wang, R. Effect of Different Industrial Activities on Soil Heavy Metal Pollution, Ecological Risk, and Health Risk. *Environ. Monit. Assess.* **2021**, *193*, 20, doi:10.1007/s10661-020-08807-z.
3. Hama Aziz, K.H.; Mustafa, F.S.; Omer, K.M.; Hama, S.; Hamarawf, R.F.; Rahman, K.O. Heavy Metal Pollution in the Aquatic Environment: Efficient and Low-Cost Removal Approaches to Eliminate Their Toxicity: A Review. *RSC Adv.* **2023**, *13*, 17595–17610, doi:10.1039/D3RA00723E.
4. Akpor, O.B. Heavy Metal Pollutants in Wastewater Effluents: Sources, Effects and Remediation. *Adv. Biosci. Bioeng.* **2014**, *2*, 37, doi:10.11648/j.abb.20140204.11.
5. Das, T.K.; Poater, A. Review on the Use of Heavy Metal Deposits from Water Treatment Waste towards Catalytic Chemical Syntheses. *Int. J. Mol. Sci.* **2021**, *22*, 13383, doi:10.3390/ijms222413383.
6. Schwarzenbach, R.P.; Escher, B.I.; Fenner, K.; Hofstetter, T.B.; Johnson, C.A.; von Gunten, U.; Wehrli, B. The Challenge of Micropollutants in Aquatic Systems. *Science (80-.)*. **2006**, *313*, 1072–1077, doi:10.1126/science.1127291.
7. Fu, F.; Wang, Q. Removal of Heavy Metal Ions from Wastewaters: A Review. *J. Environ.*

- Manage.* **2011**, 92, 407–418, doi:10.1016/j.jenvman.2010.11.011.
8. Leyva Ramos, R. Adsorption of zinc(II) from an Aqueous Solution onto Activated Carbon. *J. Hazard. Mater.* **2002**, 90, 27–38, doi:10.1016/S0304-3894(01)00333-8.
 9. Tamjidi, S.; Esmaili, H.; Kamyab Moghadas, B. Application of Magnetic Adsorbents for Removal of Heavy Metals from Wastewater: A Review Study. *Mater. Res. Express* **2019**, 6, 102004, doi:10.1088/2053-1591/ab3ffb.
 10. Chowdhury, S.R.; Yanful, E.K. Arsenic and Chromium Removal by Mixed Magnetite–maghemite Nanoparticles and the Effect of Phosphate on Removal. *J. Environ. Manage.* **2010**, 91, 2238–2247, doi:10.1016/j.jenvman.2010.06.003.
 11. Ukhurebor, K.E.; Aigbe, U.O.; Onyancha, R.B.; Nwankwo, W.; Osibote, O.A.; Paumo, H.K.; Ama, O.M.; Adetunji, C.O.; Siloko, I.U. Effect of Hexavalent Chromium on the Environment and Removal Techniques: A Review. *J. Environ. Manage.* **2021**, 280, 111809, doi:10.1016/j.jenvman.2020.111809.
 12. Coetzee, J.J.; Bansal, N.; Chirwa, E.M.N. Chromium in Environment, Its Toxic Effect from Chromite-Mining and Ferrochrome Industries, and Its Possible Bioremediation. *Expo. Heal.* **2020**, 12, 51–62, doi:10.1007/s12403-018-0284-z.
 13. Ullah, S.; Liu, Q.; Wang, S.; Jan, A.U.; Sharif, H.M.A.; Ditta, A.; Wang, G.; Cheng, H. Sources, Impacts, Factors Affecting Cr Uptake in Plants, and Mechanisms behind Phytoremediation of Cr-Contaminated Soils. *Sci. Total Environ.* **2023**, 899, 165726, doi:10.1016/j.scitotenv.2023.165726.
 14. Owlad, M.; Aroua, M.K.; Daud, W.A.W.; Baroutian, S. Removal of Hexavalent Chromium-

- Contaminated Water and Wastewater: A Review. *Water. Air. Soil Pollut.* **2009**, 200, 59–77, doi:10.1007/s11270-008-9893-7.
15. Saha, R.; Nandi, R.; Saha, B. Sources and Toxicity of Hexavalent Chromium. *J. Coord. Chem.* **2011**, 64, 1782–1806, doi:10.1080/00958972.2011.583646.
 16. Bakshi, A.; Panigrahi, A.K. A Comprehensive Review on Chromium Induced Alterations in Fresh Water Fishes. *Toxicol. Reports* **2018**, 5, 440–447, doi:10.1016/j.toxrep.2018.03.007.
 17. Coplen, T.B.; Böhlke, J.K.; De Bièvre, P.; Ding, T.; Holden, N.E.; Hopple, J.A.; Krouse, H.R.; Lamberty, A.; Peiser, H.S.; Revesz, K.; et al. Isotope-Abundance Variations of Selected Elements (IUPAC Technical Report). *Pure Appl. Chem.* **2002**, 74, 1987–2017, doi:10.1351/pac200274101987.
 18. Tumolo, M.; Ancona, V.; De Paola, D.; Losacco, D.; Campanale, C.; Massarelli, C.; Uricchio, V.F. Chromium Pollution in European Water, Sources, Health Risk, and Remediation Strategies: An Overview. *Int. J. Environ. Res. Public Health* **2020**, 17, 5438, doi:10.3390/ijerph17155438.
 19. Liang, J.; Huang, X.; Yan, J.; Li, Y.; Zhao, Z.; Liu, Y.; Ye, J.; Wei, Y. A Review of the Formation of Cr(VI) via Cr(III) Oxidation in Soils and Groundwater. *Sci. Total Environ.* **2021**, 774, 145762, doi:10.1016/j.scitotenv.2021.145762.
 20. Kamila, S.; Shaw, P.; Islam, S.; Chattopadhyay, A. Ecotoxicology of Hexavalent Chromium in Fish: An Updated Review. *Sci. Total Environ.* **2023**, 890, 164395, doi:10.1016/j.scitotenv.2023.164395.

21. Pellerin, C.; Booker, S.M. Reflections on Hexavalent Chromium: Health Hazards of an Industrial Heavyweight. *Environ. Health Perspect.* **2000**, *108*, doi:10.1289/ehp.108-a402.
22. Genchi, G.; Lauria, G.; Catalano, A.; Carocci, A.; Sinicropi, M.S. The Double Face of Metals: The Intriguing Case of Chromium. *Appl. Sci.* **2021**, *11*, 638, doi:10.3390/app11020638.
23. Unceta, N.; Séby, F.; Malherbe, J.; Donard, O.F.X. Chromium Speciation in Solid Matrices and Regulation: A Review. *Anal. Bioanal. Chem.* **2010**, *397*, 1097–1111, doi:10.1007/s00216-009-3417-1.
24. Djellabi, R.; Su, P.; Elimian, E.A.; Poliukhova, V.; Nouacer, S.; Abdelhafeez, I.A.; Abderrahim, N.; Aboagye, D.; Andhalkar, V.V.; Nabgan, W.; et al. Advances in Photocatalytic Reduction of Hexavalent Chromium: From Fundamental Concepts to Materials Design and Technology Challenges. *J. Water Process Eng.* **2022**, *50*, 103301, doi:10.1016/j.jwpe.2022.103301.
25. Buters, J.; Biedermann, T. Chromium(VI) Contact Dermatitis: Getting Closer to Understanding the Underlying Mechanisms of Toxicity and Sensitization! *J. Invest. Dermatol.* **2017**, *137*, 274–277, doi:10.1016/j.jid.2016.11.015.
26. Sharma, P.; Singh, S.P.; Parakh, S.K.; Tong, Y.W. Health Hazards of Hexavalent Chromium (Cr (VI)) and Its Microbial Reduction. *Bioengineered* **2022**, *13*, 4923–4938, doi:10.1080/21655979.2022.2037273.
27. Vaiopoulou, E.; Gikas, P. Regulations for Chromium Emissions to the Aquatic Environment in Europe and Elsewhere. *Chemosphere* **2020**, *254*, 126876,

- doi:10.1016/j.chemosphere.2020.126876.
28. Dhal, B.; Thatoi, H.N.; Das, N.N.; Pandey, B.D. Chemical and Microbial Remediation of Hexavalent Chromium from Contaminated Soil and Mining/metallurgical Solid Waste: A Review. *J. Hazard. Mater.* **2013**, *250-251*, 272–291, doi:10.1016/j.jhazmat.2013.01.048.
 29. Hackbarth, F. V.; Maass, D.; de Souza, A.A.U.; Vilar, V.J.P.; de Souza, S.M.A.G.U. Removal of Hexavalent Chromium from Electroplating Wastewaters Using Marine Macroalga *Pelvetia Canaliculata* as Natural Electron Donor. *Chem. Eng. J.* **2016**, *290*, 477–489, doi:10.1016/j.cej.2016.01.070.
 30. Lilli, M.A.; Moraetis, D.; Nikolaidis, N.P.; Karatzas, G.P.; Kalogerakis, N. Characterization and Mobility of Geogenic Chromium in Soils and River Bed Sediments of Asopos Basin. *J. Hazard. Mater.* **2015**, *281*, 12–19, doi:10.1016/j.jhazmat.2014.07.037.
 31. Hashem, M.A.; Islam, A.; Mohsin, S.; Nur-A-Tomal, M.S. Green Environment Suffers by Discharging of High-Chromium-Containing Wastewater from the Tanneries at Hazaribagh, Bangladesh. *Sustain. Water Resour. Manag.* **2015**, *1*, 343–347, doi:10.1007/s40899-015-0033-4.
 32. Mohiuddin, K.M.; Ogawa, Y.; Zakir, H.M.; Otomo, K.; Shikazono, N. Heavy Metals Contamination in Water and Sediments of an Urban River in a Developing Country. *Int. J. Environ. Sci. Technol.* **2011**, *8*, 723–736, doi:10.1007/BF03326257.
 33. Gao, Z.; Geng, Y.; Zeng, X.; Tian, X.; Yao, T.; Song, X.; Su, C. Evolution of the Anthropogenic Chromium Cycle in China. *J. Ind. Ecol.* **2022**, *26*, 592–608, doi:10.1111/jiec.13207.

34. Shanker, A.K.; Venkateswarlu, B. Chromium: Environmental Pollution, Health Effects and Mode of Action. In *Encyclopedia of Environmental Health*; Elsevier, 2011; pp. 650–659.
35. Cocârță, D.M.; Neamțu, S.; Reșetar Deac, A.M. Carcinogenic Risk Evaluation for Human Health Risk Assessment from Soils Contaminated with Heavy Metals. *Int. J. Environ. Sci. Technol.* **2016**, *13*, 2025–2036, doi:10.1007/s13762-016-1031-2.
36. Shekhawat, K.; Chatterjee, S.; Joshi, B. Chromium Toxicity and Its Health Hazards. *Int. J. Adv. Res.* **2015**, *3*, 167–172.
37. Yang, W.; Song, W.; Li, J.; Zhang, X. Bioleaching of Heavy Metals from Wastewater Sludge with the Aim of Land Application. *Chemosphere* **2020**, *249*, 126134, doi:10.1016/j.chemosphere.2020.126134.
38. Shekhawat, A.; Kahu, S.; Saravanan, D.; Jugade, R. Synergistic Behaviour of Ionic Liquid Impregnated Sulphate-Crosslinked Chitosan towards Adsorption of Cr(VI). *Int. J. Biol. Macromol.* **2015**, *80*, 615–626, doi:10.1016/j.ijbiomac.2015.07.035.
39. Martin, S.; Griswold, W. NHuman Health Effects of Heavy Metalso Title. *Environ. Sci. Technol. Briefs Citizens* **2009**, *15*, 1–6.
40. Liu, D.; Zou, J.; Wang, M.; Jiang, W. Hexavalent Chromium Uptake and Its Effects on Mineral Uptake, Antioxidant Defence System and Photosynthesis in *Amaranthus Viridis L.* *Bioresour. Technol.* **2008**, *99*, 2628–2636, doi:10.1016/j.biortech.2007.04.045.
41. Oliveira, H. Chromium as an Environmental Pollutant: Insights on Induced Plant Toxicity. *J. Bot.* **2012**, *2012*, 1–8, doi:10.1155/2012/375843.

42. Sadegh, H.; Ali, G.A.M.; Gupta, V.K.; Makhoulf, A.S.H.; Shahryari-ghoshekandi, R.; Nadagouda, M.N.; Sillanpää, M.; Megiel, E. The Role of Nanomaterials as Effective Adsorbents and Their Applications in Wastewater Treatment. *J. Nanostructure Chem.* **2017**, 7, 1–14, doi:10.1007/s40097-017-0219-4.
43. Jun, B.-M.; Lee, H.-K.; Park, S.; Kim, T.-J. Purification of Uranium-Contaminated Radioactive Water by Adsorption: A Review on Adsorbent Materials. *Sep. Purif. Technol.* **2021**, 278, 119675, doi:10.1016/j.seppur.2021.119675.
44. Masindi, V.; Mkhonza, P.; Tekere, M. Sources of Heavy Metals Pollution. In; 2021; pp. 419–454.
45. Figueiredo, H.; Quintelas, C. Tailored Zeolites for the Removal of Metal Oxyanions: Overcoming Intrinsic Limitations of Zeolites. *J. Hazard. Mater.* **2014**, 274, 287–299, doi:10.1016/j.jhazmat.2014.04.012.
46. Pakade, V.E.; Tavengwa, N.T.; Madikizela, L.M. Recent Advances in Hexavalent Chromium Removal from Aqueous Solutions by Adsorptive Methods. *RSC Adv.* **2019**, 9, 26142–26164, doi:10.1039/C9RA05188K.
47. Tee, W.T.; Loh, N.Y.L.; Lai, K.C.; Hiew, B.Y.Z.; Gan, S.; Lee, L.Y. Application of 3D Heteroatom-Doped Graphene in Adsorptive Removal of Water Pollutants: Review on Hydrothermal Synthesis and Its Influencing Factors. *Sep. Purif. Technol.* **2023**, 320, 124072, doi:10.1016/j.seppur.2023.124072.
48. Duan, C.; Ma, T.; Wang, J.; Zhou, Y. Removal of Heavy Metals from Aqueous Solution Using Carbon-Based Adsorbents: A Review. *J. Water Process Eng.* **2020**, 37, 101339,

doi:10.1016/j.jwpe.2020.101339.

49. Fernández, B.; Ayala, J.; del Valle, E.; Martínez-Blanco, D.; Castañón, A.M.; Menéndez-Aguado, J.M. Recycling of Waste Toner Powder as Adsorbent to Remove Aqueous Heavy Metals. *Materials (Basel)*. **2022**, *15*, 4150, doi:10.3390/ma15124150.
50. Pohl, A. Removal of Heavy Metal Ions from Water and Wastewaters by Sulfur-Containing Precipitation Agents. *Water, Air, Soil Pollut.* **2020**, *231*, 503, doi:10.1007/s11270-020-04863-w.
51. Malik, L.A.; Bashir, A.; Qureashi, A.; Pandith, A.H. Detection and Removal of Heavy Metal Ions: A Review. *Environ. Chem. Lett.* **2019**, *17*, 1495–1521, doi:10.1007/s10311-019-00891-z.
52. Skousen, J. Overview of Acid Mine Drainage Treatment with Chemicals. In *Acid Mine Drainage, Rock Drainage, and Acid Sulfate Soils*; Wiley, 2014; pp. 325–337.
53. Egiebor, N.O.; Oni, B. Acid Rock Drainage Formation and Treatment: A Review. *Asia-Pacific J. Chem. Eng.* **2007**, *2*, 47–62, doi:10.1002/apj.57.
54. Lewis, A.E. Review of Metal Sulphide Precipitation. *Hydrometallurgy* **2010**, *104*, 222–234, doi:10.1016/j.hydromet.2010.06.010.
55. Shim, H.Y.; Lee, K.S.; Lee, D.S.; Jeon, D.S.; Park, M.S.; Shin, J.S.; Lee, Y.K.; Goo, J.W.; Kim, S.B.; Chung, D.Y. Application of Electrocoagulation and Electrolysis on the Precipitation of Heavy Metals and Particulate Solids in Washwater from the Soil Washing. *J. Agric. Chem. Environ.* **2014**, *03*, 130–138, doi:10.4236/jacen.2014.34015.

56. Aziz, H.A.; Adlan, M.N.; Ariffin, K.S. Heavy Metals (Cd, Pb, Zn, Ni, Cu and Cr(III)) Removal from Water in Malaysia: Post Treatment by High Quality Limestone. *Bioresour. Technol.* **2008**, *99*, 1578–1583, doi:10.1016/j.biortech.2007.04.007.
57. Takht Ravanchi, M.; Kaghazchi, T.; Kargari, A. Application of Membrane Separation Processes in Petrochemical Industry: A Review. *Desalination* **2009**, *235*, 199–244, doi:10.1016/j.desal.2007.10.042.
58. Cevallos-Mendoza, J.; Amorim, C.; Rodríguez-Díaz, J.; Montenegro, M. Removal of Contaminants from Water by Membrane Filtration: A Review. *Membranes (Basel)*. **2022**, *12*, 570, doi:10.3390/membranes12060570.
59. Rezakazemi, M.; Khajeh, A.; Mesbah, M. Membrane Filtration of Wastewater from Gas and Oil Production. *Environ. Chem. Lett.* **2018**, *16*, 367–388, doi:10.1007/s10311-017-0693-4.
60. Qasem, N.A.A.; Mohammed, R.H.; Lawal, D.U. Removal of Heavy Metal Ions from Wastewater: A Comprehensive and Critical Review. *npj Clean Water* **2021**, *4*, 36, doi:10.1038/s41545-021-00127-0.
61. Zubair, M.M.; Saleem, H.; Zaidi, S.J. Recent Progress in Reverse Osmosis Modeling: An Overview. *Desalination* **2023**, *564*, 116705, doi:10.1016/j.desal.2023.116705.
62. Samaei, S.M.; Gato-Trinidad, S.; Altaee, A. Performance Evaluation of Reverse Osmosis Process in the Post-Treatment of Mining Wastewaters: Case Study of Costerfield Mining Operations, Victoria, Australia. *J. Water Process Eng.* **2020**, *34*, 101116, doi:10.1016/j.jwpe.2019.101116.

63. He, M.; Wang, L.; Lv, Y.; Wang, X.; Zhu, J.; Zhang, Y.; Liu, T. Novel Polydopamine/metal Organic Framework Thin Film Nanocomposite Forward Osmosis Membrane for Salt Rejection and Heavy Metal Removal. *Chem. Eng. J.* **2020**, 389, 124452, doi:10.1016/j.cej.2020.124452.
64. Cui, Y.; Ge, Q.; Liu, X.-Y.; Chung, T.-S. Novel Forward Osmosis Process to Effectively Remove Heavy Metal Ions. *J. Memb. Sci.* **2014**, 467, 188–194, doi:10.1016/j.memsci.2014.05.034.
65. Ibarra-Rodríguez, D.; Lizardi-Mendoza, J.; López-Maldonado, E.A.; Oropeza-Guzmán, M.T. Capacity of “nopal” Pectin as a Dual Coagulant-Flocculant Agent for Heavy Metals Removal. *Chem. Eng. J.* **2017**, 323, 19–28, doi:10.1016/j.cej.2017.04.087.
66. Verma, A.K.; Dash, R.R.; Bhunia, P. A Review on Chemical Coagulation/flocculation Technologies for Removal of Colour from Textile Wastewaters. *J. Environ. Manage.* **2012**, 93, 154–168, doi:10.1016/j.jenvman.2011.09.012.
67. Matilainen, A.; Vepsäläinen, M.; Sillanpää, M. Natural Organic Matter Removal by Coagulation during Drinking Water Treatment: A Review. *Adv. Colloid Interface Sci.* **2010**, 159, 189–197, doi:10.1016/j.cis.2010.06.007.
68. Chang, Q.; Zhang, M.; Wang, J. Removal of Cu²⁺ and Turbidity from Wastewater by Mercaptoacetyl Chitosan. *J. Hazard. Mater.* **2009**, 169, 621–625, doi:10.1016/j.jhazmat.2009.03.144.
69. Xu, D.; Zhou, B.; Yuan, R. Optimization of Coagulation-Flocculation Treatment of Wastewater Containing Zn(II) and Cr(VI). *IOP Conf. Ser. Earth Environ. Sci.* **2019**, 227,

- 052049, doi:10.1088/1755-1315/227/5/052049.
70. Zewail, T.M.; Yousef, N.S. Kinetic Study of Heavy Metal Ions Removal by Ion Exchange in Batch Conical Air Spouted Bed. *Alexandria Eng. J.* **2015**, *54*, 83–90, doi:10.1016/j.aej.2014.11.008.
 71. Abo-Farha, S.A.; Abdel-Aal, A.Y.; Ashour, I.A.; Garamon, S.E. Removal of Some Heavy Metal Cations by Synthetic Resin Purolite C100. *J. Hazard. Mater.* **2009**, *169*, 190–194, doi:10.1016/j.jhazmat.2009.03.086.
 72. Al-Asheh, S.; Aidan, A. A Comprehensive Method of Ion Exchange Resins Regeneration and Its Optimization for Water Treatment. In *Promising Techniques for Wastewater Treatment and Water Quality Assessment*; IntechOpen, 2021.
 73. Tenório, J.A.; Espinosa, D.C.. Treatment of Chromium Plating Process Effluents with Ion Exchange Resins. *Waste Manag.* **2001**, *21*, 637–642, doi:10.1016/S0956-053X(00)00118-5.
 74. Kang, S.-Y.; Lee, J.-U.; Moon, S.-H.; Kim, K.-W. Competitive Adsorption Characteristics of Co^{2+} , Ni^{2+} , and Cr^{3+} by IRN-77 Cation Exchange Resin in Synthesized Wastewater. *Chemosphere* **2004**, *56*, 141–147, doi:10.1016/j.chemosphere.2004.02.004.
 75. Cavaco, S.A.; Fernandes, S.; Quina, M.M.; Ferreira, L.M. Removal of Chromium from Electroplating Industry Effluents by Ion Exchange Resins. *J. Hazard. Mater.* **2007**, *144*, 634–638, doi:10.1016/j.jhazmat.2007.01.087.
 76. Li, X.; Gao, X.; Ai, L.; Jiang, J. Mechanistic Insight into the Interaction and Adsorption of Cr(VI) with Zeolitic Imidazolate Framework-67 Microcrystals from Aqueous Solution.

- Chem. Eng. J.* **2015**, 274, 238–246, doi:10.1016/j.cej.2015.03.127.
77. Reddy, K.H.; Reddy, A.R. Removal of Heavy Metal Ions Using the Chelating Polymers Derived by the Condensation of poly(3-hydroxy-4-acetylphenyl Methacrylate) with Different Diamines. *J. Appl. Polym. Sci.* **2003**, 88, 414–421, doi:10.1002/app.11717.
 78. ADHOUM, N.; MONSER, L.; BELLAKHAL, N.; BELGAIED, J. Treatment of Electroplating Wastewater Containing Cu^{2+} , Zn^{2+} and Cr(VI) by Electrocoagulation. *J. Hazard. Mater.* **2004**, 112, 207–213, doi:10.1016/j.jhazmat.2004.04.018.
 79. Rajkumar, D.; Palanivelu, K. Electrochemical Treatment of Industrial Wastewater. *J. Hazard. Mater.* **2004**, 113, 123–129, doi:10.1016/j.jhazmat.2004.05.039.
 80. Moussa, D.T.; El-Naas, M.H.; Nasser, M.; Al-Marri, M.J. A Comprehensive Review of Electrocoagulation for Water Treatment: Potentials and Challenges. *J. Environ. Manage.* **2017**, 186, 24–41, doi:10.1016/j.jenvman.2016.10.032.
 81. Khan, S.U.; Islam, D.T.; Farooqi, I.H.; Ayub, S.; Basheer, F. Hexavalent Chromium Removal in an Electrocoagulation Column Reactor: Process Optimization Using CCD, Adsorption Kinetics and pH Modulated Sludge Formation. *Process Saf. Environ. Prot.* **2019**, 122, 118–130, doi:10.1016/j.psep.2018.11.024.
 82. Ammar, H.B.; Brahim, M. Ben; Abdelhédi, R.; Samet, Y. Green Electrochemical Process for Metronidazole Degradation at BDD Anode in Aqueous Solutions via Direct and Indirect Oxidation. *Sep. Purif. Technol.* **2016**, 157, 9–16, doi:10.1016/j.seppur.2015.11.027.
 83. Azubuike, C.C.; Chikere, C.B.; Okpokwasili, G.C. Bioremediation Techniques—classification Based on Site of Application: Principles, Advantages, Limitations and

- Prospects. *World J. Microbiol. Biotechnol.* **2016**, 32, 180, doi:10.1007/s11274-016-2137-x.
84. Prasad, S.; Yadav, K.K.; Kumar, S.; Gupta, N.; Cabral-Pinto, M.M.S.; Rezaia, S.; Radwan, N.; Alam, J. Chromium Contamination and Effect on Environmental Health and Its Remediation: A Sustainable Approaches. *J. Environ. Manage.* **2021**, 285, 112174, doi:10.1016/j.jenvman.2021.112174.
 85. Yan, G.; Gao, Y.; Xue, K.; Qi, Y.; Fan, Y.; Tian, X.; Wang, J.; Zhao, R.; Zhang, P.; Liu, Y.; et al. Toxicity Mechanisms and Remediation Strategies for Chromium Exposure in the Environment. *Front. Environ. Sci.* **2023**, 11, doi:10.3389/fenvs.2023.1131204.
 86. Srivastava, S.; Thakur, I.S. Isolation and Process Parameter Optimization of *Aspergillus* Sp. for Removal of Chromium from Tannery Effluent. *Bioresour. Technol.* **2006**, 97, 1167–1173, doi:10.1016/j.biortech.2005.05.012.
 87. Qu, M.; Chen, J.; Huang, Q.; Chen, J.; Xu, Y.; Luo, J.; Wang, K.; Gao, W.; Zheng, Y. Bioremediation of Hexavalent Chromium Contaminated Soil by a Bioleaching System with Weak Magnetic Fields. *Int. Biodeterior. Biodegradation* **2018**, 128, 41–47, doi:10.1016/j.ibiod.2016.08.022.
 88. Hossan, S.; Hossain, S.; Islam, M.R.; Kabir, M.H.; Ali, S.; Islam, M.S.; Imran, K.M.; Moniruzzaman, M.; Mou, T.J.; Parvez, A.K.; et al. Bioremediation of Hexavalent Chromium by Chromium Resistant Bacteria Reduces Phytotoxicity. *Int. J. Environ. Res. Public Health* **2020**, 17, 6013, doi:10.3390/ijerph17176013.
 89. Ahmad, K.; Ghatak, H.R.; Ahuja, S.M. A Review on Photocatalytic Remediation of Environmental Pollutants and H₂ Production through Water Splitting: A Sustainable

- Approach. *Environ. Technol. Innov.* **2020**, *19*, 100893, doi:10.1016/j.eti.2020.100893.
90. Ni, M.; Leung, M.K.H.; Leung, D.Y.C.; Sumathy, K. A Review and Recent Developments in Photocatalytic Water-Splitting Using TiO₂ for Hydrogen Production. *Renew. Sustain. Energy Rev.* **2007**, *11*, 401–425, doi:10.1016/j.rser.2005.01.009.
 91. Gao, X.; Meng, X. Photocatalysis for Heavy Metal Treatment: A Review. *Processes* **2021**, *9*, 1729, doi:10.3390/pr9101729.
 92. Abdelhafeez, I.A.; Ramakrishna, S. Promising Sustainable Models Toward Water, Air, and Solid Sustainable Management in the View of SDGs. *Mater. Circ. Econ.* **2021**, *3*, 21, doi:10.1007/s42824-021-00039-x.
 93. Lin, H.; Xiao, Y.; Geng, A.; Bi, H.; Xu, X.; Xu, X.; Zhu, J. Research Progress on Graphitic Carbon Nitride/Metal Oxide Composites: Synthesis and Photocatalytic Applications. *Int. J. Mol. Sci.* **2022**, *23*, 12979, doi:10.3390/ijms232112979.
 94. Meichtry, J.M.; Brusa, M.; Mailhot, G.; Grela, M.A.; Litter, M.I. Heterogeneous Photocatalysis of Cr(VI) in the Presence of Citric Acid over TiO₂ Particles: Relevance of Cr(V)–citrate Complexes. *Appl. Catal. B Environ.* **2007**, *71*, 101–107, doi:10.1016/j.apcatb.2006.09.002.
 95. Hasija, V.; Raizada, P.; Singh, P.; Verma, N.; Khan, A.A.P.; Singh, A.; Selvasembian, R.; Kim, S.Y.; Hussain, C.M.; Nguyen, V.-H.; et al. Progress on the Photocatalytic Reduction of Hexavalent Cr (VI) Using Engineered Graphitic Carbon Nitride. *Process Saf. Environ. Prot.* **2021**, *152*, 663–678, doi:10.1016/j.psep.2021.06.042.
 96. Ola, O.; Maroto-Valer, M.M. Review of Material Design and Reactor Engineering on TiO₂

- Photocatalysis for CO₂ Reduction. *J. Photochem. Photobiol. C Photochem. Rev.* **2015**, *24*, 16–42, doi:10.1016/j.jphotochemrev.2015.06.001.
97. Daghrir, R.; Drogui, P.; Robert, D. Modified TiO₂ For Environmental Photocatalytic Applications: A Review. *Ind. Eng. Chem. Res.* **2013**, *52*, 3581–3599, doi:10.1021/ie303468t.
 98. Zhu, S.; Wang, D. Photocatalysis: Basic Principles, Diverse Forms of Implementations and Emerging Scientific Opportunities. *Adv. Energy Mater.* **2017**, *7*, doi:10.1002/aenm.201700841.
 99. Yu, H.; Ma, Q.; Gao, C.; Liao, S.; Zhang, Y.; Quan, H.; Zhai, R. Petal-like g-C₃N₄ Enhances the Photocatalyst Removal of Hexavalent Chromium. *Catalysts* **2023**, *13*, 641, doi:10.3390/catal13030641.
 100. Miao, H.; Zhang, W.; Wang, T.; Yang, Z.; Kong, C. g-C₃N₄-Based Nanocomposites for the Photocatalytic Degradation of VOCs: A Review. *Prog. Nat. Sci. Mater. Int.* **2023**, *33*, 407–424, doi:10.1016/j.pnsc.2023.08.004.
 101. Islam, J.B.; Islam, M.R.; Furukawa, M.; Tateishi, I.; Katsumata, H.; Kaneco, S. Ag-Modified g-C₃N₄ with Enhanced Activity for the Photocatalytic Reduction of Hexavalent Chromium in the Presence of EDTA under Ultraviolet Irradiation. *Environ. Technol.* **2023**, *44*, 3627–3640, doi:10.1080/09593330.2022.2068379.
 102. Zhu, J.; Xiao, P.; Li, H.; Carabineiro, S.A.C. Graphitic Carbon Nitride: Synthesis, Properties, and Applications in Catalysis. *ACS Appl. Mater. Interfaces* **2014**, *6*, 16449–16465, doi:10.1021/am502925j.

-
103. Huang, H.; Yang, S.; Vajtai, R.; Wang, X.; Ajayan, P.M. Pt-Decorated 3D Architectures Built from Graphene and Graphitic Carbon Nitride Nanosheets as Efficient Methanol Oxidation Catalysts. *Adv. Mater.* **2014**, *26*, 5160–5165, doi:10.1002/adma.201401877.
104. Majdoub, M.; Anfar, Z.; Amedlous, A. Emerging Chemical Functionalization of g-C₃N₄: Covalent/Noncovalent Modifications and Applications. *ACS Nano* **2020**, *14*, 12390–12469, doi:10.1021/acsnano.0c06116.
105. Goettmann, F.; Fischer, A.; Antonietti, M.; Thomas, A. Metal-Free Catalysis of Sustainable Friedel–Crafts Reactions: Direct Activation of Benzene by Carbon Nitrides to Avoid the Use of Metal Chlorides and Halogenated Compounds. *Chem. Commun.* **2006**, 4530–4532, doi:10.1039/B608532F.
106. Wang, X.; Maeda, K.; Thomas, A.; Takanabe, K.; Xin, G.; Carlsson, J.M.; Domen, K.; Antonietti, M. A Metal-Free Polymeric Photocatalyst for Hydrogen Production from Water under Visible Light. *Nat. Mater.* **2009**, *8*, 76–80, doi:10.1038/nmat2317.
107. Wang, Y.; Wang, X.; Antonietti, M. Polymeric Graphitic Carbon Nitride as a Heterogeneous Organocatalyst: From Photochemistry to Multipurpose Catalysis to Sustainable Chemistry. *Angew. Chemie Int. Ed.* **2012**, *51*, 68–89, doi:10.1002/anie.201101182.
108. Cao, S.; Yu, J. g-C₃N₄ -Based Photocatalysts for Hydrogen Generation. *J. Phys. Chem. Lett.* **2014**, *5*, 2101–2107, doi:10.1021/jz500546b.
109. Baudys, M.; Paušová, Š.; Praus, P.; Brezová, V.; Dvoranová, D.; Barbieriková, Z.; Krýsa, J. Graphitic Carbon Nitride for Photocatalytic Air Treatment. *Materials (Basel)*. **2020**, *13*,

- 3038, doi:10.3390/ma13133038.
110. Zhang, Y.; Pan, Q.; Chai, G.; Liang, M.; Dong, G.; Zhang, Q.; Qiu, J. Synthesis and Luminescence Mechanism of Multicolor-Emitting g-C₃N₄ Nanopowders by Low Temperature Thermal Condensation of Melamine. *Sci. Rep.* **2013**, *3*, 1943, doi:10.1038/srep01943.
111. Blaskiewicz, S.F.; Francisco, J.L.; Marken, F.; Mascaro, L.H. Carbon Nitrides in Photoelectrochemistry: State of the Art and Perspectives Beyond Water Splitting. *ACS Appl. Energy Mater.* **2024**, *7*, 3021–3038, doi:10.1021/acsaem.3c02623.
112. Ong, W.-J.; Tan, L.-L.; Ng, Y.H.; Yong, S.-T.; Chai, S.-P. Graphitic Carbon Nitride (g-C₃N₄)-Based Photocatalysts for Artificial Photosynthesis and Environmental Remediation: Are We a Step Closer To Achieving Sustainability? *Chem. Rev.* **2016**, *116*, 7159–7329, doi:10.1021/acs.chemrev.6b00075.
113. Singh, P.P.; Srivastava, V. Recent Advances in Visible-Light Graphitic Carbon Nitride (g-C₃N₄) Photocatalysts for Chemical Transformations. *RSC Adv.* **2022**, *12*, 18245–18265, doi:10.1039/D2RA01797K.
114. Habisreutinger, S.N.; Schmidt-Mende, L.; Stolarczyk, J.K. Photocatalytic Reduction of CO₂ on TiO₂ and Other Semiconductors. *Angew. Chemie Int. Ed.* **2013**, *52*, 7372–7408, doi:10.1002/anie.201207199.
115. Adegoke, K.A.; Maxakato, N.W. Efficient Strategies for Boosting the Performance of 2D Graphitic Carbon Nitride Nanomaterials during Photoreduction of Carbon Dioxide to Energy-Rich Chemicals. *Mater. Today Chem.* **2022**, *23*, 100605,

doi:10.1016/j.mtchem.2021.100605.

116. Das, S.; Chowdhury, A. Recent Advancements of g-C₃N₄-Based Magnetic Photocatalysts towards the Degradation of Organic Pollutants: A Review. *Nanotechnology* **2022**, *33*, 072004, doi:10.1088/1361-6528/ac3614.
117. Wudil, Y.S.; Ahmad, U.F.; Gondal, M.A.; Al-Osta, M.A.; Almohammed, A.; Sa'id, R.S.; Hrahsheh, F.; Haruna, K.; Mohamed, M.J.S. Tuning of Graphitic Carbon Nitride (g-C₃N₄) for Photocatalysis: A Critical Review. *Arab. J. Chem.* **2023**, *16*, 104542, doi:10.1016/j.arabjc.2023.104542.
118. Wang, G.; Lv, S.; Shen, Y.; Li, W.; Lin, L.; Li, Z. Advancements in Heterojunction, Cocatalyst, Defect and Morphology Engineering of Semiconductor Oxide Photocatalysts. *J. Mater.* **2024**, *10*, 315–338, doi:10.1016/j.jmat.2023.05.014.
119. Gao, R.-H.; Ge, Q.; Jiang, N.; Cong, H.; Liu, M.; Zhang, Y.-Q. Graphitic Carbon Nitride (g-C₃N₄)-Based Photocatalytic Materials for Hydrogen Evolution. *Front. Chem.* **2022**, *10*, 1048504, doi:10.3389/fchem.2022.1048504.
120. Pattanayak, D.S.; Pal, D.; Mishra, J.; Thakur, C. Noble Metal-free Doped Graphitic Carbon Nitride (g-C₃N₄) for Efficient Photodegradation of Antibiotics: Progress, Limitations, and Future Directions. *Environ. Sci. Pollut. Res.* **2022**, *30*, 25546–25558, doi:10.1007/s11356-022-20170-9.
121. Jin, J.; Liang, Q.; Ding, C.; Li, Z.; Xu, S. Simultaneous Synthesis-Immobilization of Ag Nanoparticles Functionalized 2D g-C₃N₄ Nanosheets with Improved Photocatalytic Activity. *J. Alloys Compd.* **2017**, *691*, 763–771, doi:10.1016/j.jallcom.2016.08.302.

122. Li, Y.; Liu, Z.; Li, Z.; Wang, Q. Renewable Biomass-Derived Carbon-Supported g-C₃N₄ Doped with Ag for Enhanced Photocatalytic Reduction of CO₂. *J. Colloid Interface Sci.* **2022**, *606*, 1311–1321, doi:10.1016/j.jcis.2021.08.176.
123. Liu, R.; Yang, W.; He, G.; Zheng, W.; Li, M.; Tao, W.; Tian, M. Ag-Modified g-C₃N₄ Prepared by a One-Step Calcination Method for Enhanced Catalytic Efficiency and Stability. *ACS Omega* **2020**, *5*, 19615–19624, doi:10.1021/acsomega.0c02161.
124. Qi, K.; Li, Y.; Xie, Y.; Liu, S.; Zheng, K.; Chen, Z.; Wang, R. Ag Loading Enhanced Photocatalytic Activity of g-C₃N₄ Porous Nanosheets for Decomposition of Organic Pollutants. *Front. Chem.* **2019**, *7*, doi:10.3389/fchem.2019.00091.
125. Nguyen, T.T.; Bui, H.T.; Nguyen, G.T.; Hoang, T.N.; Van Tran, C.; Ho, P.H.; Hoai Nguyen, P.T.; Kim, J.Y.; Chang, S.W.; Chung, W.J.; et al. Facile Preparation of Porphyrin@ g-C₃N₄/Ag Nanocomposite for Improved Photocatalytic Degradation of Organic Dyes in Aqueous Solution. *Environ. Res.* **2023**, *231*, 115984, doi:10.1016/j.envres.2023.115984.
126. He, Q.; Zhou, F.; Zhan, S.; Yang, Y.; Liu, Y.; Tian, Y.; Huang, N. Enhancement of Photocatalytic and Photoelectrocatalytic Activity of Ag Modified Mpg-C₃N₄ Composites. *Appl. Surf. Sci.* **2017**, *391*, 423–431, doi:10.1016/j.apsusc.2016.07.005.
127. Mishra, A.; Mehta, A.; Basu, S.; Shetti, N.P.; Reddy, K.R.; Aminabhavi, T.M. Graphitic Carbon Nitride (g-C₃N₄)–based Metal-Free Photocatalysts for Water Splitting: A Review. *Carbon N. Y.* **2019**, *149*, 693–721, doi:10.1016/j.carbon.2019.04.104.
128. Jiang, L.; Yuan, X.; Pan, Y.; Liang, J.; Zeng, G.; Wu, Z.; Wang, H. Doping of Graphitic Carbon Nitride for Photocatalysis: A Review. *Appl. Catal. B Environ.* **2017**, *217*, 388–406,

- doi:10.1016/j.apcatb.2017.06.003.
129. Naseri, A.; Samadi, M.; Pourjavadi, A.; Moshfegh, A.Z.; Ramakrishna, S. Graphitic Carbon Nitride (g-C₃N₄)-Based Photocatalysts for Solar Hydrogen Generation: Recent Advances and Future Development Directions. *J. Mater. Chem. A* **2017**, *5*, 23406–23433, doi:10.1039/C7TA05131J.
130. Qi, K.; Liu, S.; Zada, A. Graphitic Carbon Nitride, a Polymer Photocatalyst. *J. Taiwan Inst. Chem. Eng.* **2020**, *109*, 111–123, doi:10.1016/j.jtice.2020.02.012.
131. Zhou, X.; Xu, B.; Zhang, J.; Zhao, Q.; Li, C.; Dong, H.; Wang, X.; Yang, J. Regulated Effect of Organic Small Molecular Doped in Carbon Nitride Skeleton for Boosting Photocatalytic Hydrogen Evolution. *Int. J. Hydrogen Energy* **2021**, *46*, 38299–38309, doi:10.1016/j.ijhydene.2021.09.096.
132. Jin, X.; Zhang, L.; Fan, X.; Tian, J.; Wang, M.; Shi, J. A Photo-Excited Electron Transfer Hyperchannel Constructed in Pt-Dispersed Pyrimidine-Modified Carbon Nitride for Remarkably Enhanced Water-Splitting Photocatalytic Activity. *Appl. Catal. B Environ.* **2018**, *237*, 888–894, doi:10.1016/j.apcatb.2018.06.035.
133. Ho, W.; Zhang, Z.; Lin, W.; Huang, S.; Zhang, X.; Wang, X.; Huang, Y. Copolymerization with 2,4,6-Triaminopyrimidine for the Rolling-up the Layer Structure, Tunable Electronic Properties, and Photocatalysis of g-C₃N₄. *ACS Appl. Mater. Interfaces* **2015**, *7*, 5497–5505, doi:10.1021/am509213x.
134. Bellamkonda, S.; Shanmugam, R.; Gangavarapu, R.R. Extending the π -Electron Conjugation in 2D Planar Graphitic Carbon Nitride: Efficient Charge Separation for Overall

- Water Splitting. *J. Mater. Chem. A* **2019**, 7, 3757–3771, doi:10.1039/C8TA10580D.
135. Li, Z.; Zhou, S.; Yang, Q.; Zhang, Z.; Fang, X. Insight into the Enhanced Hydrogen Evolution Activity of 2,4-Diaminopyrimidine-Doped Graphitic Carbon Nitride Photocatalysts. *J. Phys. Chem. C* **2019**, 123, 2228–2237, doi:10.1021/acs.jpcc.8b10252.
136. Zhang, L.; Zhang, J.; Yu, H.; Yu, J. Emerging S-Scheme Photocatalyst. *Adv. Mater.* **2022**, 34, doi:10.1002/adma.202107668.
137. Dong, F.; Zhao, Z.; Xiong, T.; Ni, Z.; Zhang, W.; Sun, Y.; Ho, W.-K. In Situ Construction of g-C₃N₄/g-C₃N₄ Metal-Free Heterojunction for Enhanced Visible-Light Photocatalysis. *ACS Appl. Mater. Interfaces* **2013**, 5, 11392–11401, doi:10.1021/am403653a.
138. Alaghmandfard, A.; Ghandi, K. A Comprehensive Review of Graphitic Carbon Nitride (g-C₃N₄)–Metal Oxide-Based Nanocomposites: Potential for Photocatalysis and Sensing. *Nanomaterials* **2022**, 12, 294, doi:10.3390/nano12020294.
139. Gogoi, D.; Shah, A.K.; Qureshi, M.; Golder, A.K.; Peela, N.R. Silver Grafted Graphitic-Carbon Nitride Ternary Hetero-Junction Ag/ g-C₃N₄ (Urea)- g-C₃N₄ (Thiourea) with Efficient Charge Transfer for Enhanced Visible-Light Photocatalytic Green H₂ Production. *Appl. Surf. Sci.* **2021**, 558, 149900, doi:10.1016/j.apsusc.2021.149900.
140. Chen, L.; Maigbay, M.A.; Li, M.; Qiu, X. Synthesis and Modification Strategies of g-C₃N₄ Nanosheets for Photocatalytic Applications. *Adv. Powder Mater.* **2024**, 3, 100150, doi:10.1016/j.apmate.2023.100150.
141. Low, J.; Yu, J.; Jaroniec, M.; Wageh, S.; Al-Ghamdi, A.A. Heterojunction Photocatalysts. *Adv. Mater.* **2017**, 29, doi:10.1002/adma.201601694.

142. Luo, Y.; Zhu, Y.; Han, Y.; Ye, H.; Liu, R.; Lan, Y.; Xue, M.; Xie, X.; Yu, S.; Zhang, L.; et al. g-C₃N₄-Based Photocatalysts for Organic Pollutant Removal: A Critical Review. *Carbon Res.* **2023**, 2, 14, doi:10.1007/s44246-023-00045-5.
143. Xu, Z.; Shi, Y.; Li, L.; Sun, H.; Amin, M.S.; Guo, F.; Wen, H.; Shi, W. Fabrication of 2D/2D Z-Scheme Highly Crystalline Carbon Nitride/ δ -Bi₂O₃ Heterojunction Photocatalyst with Enhanced Photocatalytic Degradation of Tetracycline. *J. Alloys Compd.* **2022**, 895, 162667, doi:10.1016/j.jallcom.2021.162667.
144. Lu, X.; Quan, L.; Hou, H.; Qian, J.; Liu, Z.; Zhang, Q. Fabrication of 1D/2D Y-Doped CeO₂/ZnIn₂S₄ S-Scheme Photocatalyst for Enhanced Photocatalytic H₂ Evolution. *J. Alloys Compd.* **2022**, 925, 166552, doi:10.1016/j.jallcom.2022.166552.
145. Liao, G.; Li, C.; Li, X.; Fang, B. Emerging Polymeric Carbon Nitride Z-Scheme Systems for Photocatalysis. *Cell Reports Phys. Sci.* **2021**, 2, 100355, doi:10.1016/j.xcrp.2021.100355.
146. Liu, W.; Wang, M.; Xu, C.; Chen, S. Facile Synthesis of g-C₃N₄/ZnO Composite with Enhanced Visible Light Photooxidation and Photoreduction Properties. *Chem. Eng. J.* **2012**, 209, 386–393, doi:10.1016/j.cej.2012.08.033.
147. Kalisamy, P.; Hossain, M.S.; Macadangdang Jr., R.R.; Madhubala, V.; Palanivel, B.; Venkatachalam, M.; Massoud, E.E.S.; Sreedevi, G. ZnO Coupled F-Doped g-C₃N₄: Z-Scheme Heterojunction for Visible-Light Driven Photocatalytic Degradation Reaction. *Inorg. Chem. Commun.* **2022**, 135, 109102, doi:10.1016/j.inoche.2021.109102.
148. Zhang, S.; Su, C.; Ren, H.; Li, M.; Zhu, L.; Ge, S.; Wang, M.; Zhang, Z.; Li, L.; Cao, X.

- In-Situ Fabrication of g-C₃N₄/ZnO Nanocomposites for Photocatalytic Degradation of Methylene Blue: Synthesis Procedure Does Matter. *Nanomaterials* **2019**, 9, 215, doi:10.3390/nano9020215.
149. Chen, Z.; Guo, F.; Sun, H.; Shi, Y.; Shi, W. Well-Designed Three-Dimensional Hierarchical Hollow Tubular g-C₃N₄/ZnIn₂S₄ Nanosheets Heterostructure for Achieving Efficient Visible-Light Photocatalytic Hydrogen Evolution. *J. Colloid Interface Sci.* **2022**, 607, 1391–1401, doi:10.1016/j.jcis.2021.09.095.
150. Si, Y.; Sun, Z.; Huang, L.; Chen, M.; Wu, L. A “ship-in-a-Bottle” Strategy to Fabricate Highly Crystallized Nanoporous Graphitic C₃N₄ Microspheres under Pressurized Conditions. *J. Mater. Chem. A* **2019**, 7, 8952–8959, doi:10.1039/C9TA00151D.
151. Bandyopadhyay, A.; Ghosh, D.; Kaley, N.M.; Pati, S.K. Photocatalytic Activity of g-C₃N₄ Quantum Dots in Visible Light: Effect of Physicochemical Modifications. *J. Phys. Chem. C* **2017**, 121, 1982–1989, doi:10.1021/acs.jpcc.6b11520.

CHAPTER TWO

Facile Synthesis of ZnO/g-C₃N₄ with Enhanced Photocatalytic Performance for the Reduction of Cr(VI) in Presence of EDTA Under Visible Light Irradiation

2.1 Introduction

The existence of toxic heavy metals in land and water has become a global concern in the past few decade [1,2]. Chromium is considered one of the most typical toxic heavy metal, which is widely used in different industries such as electroplating, steel fabricating, metal finishing, leather tanning, mining of chromium ores, fertilizing, dyeing and painting as a raw material [2,3]. These industries discharge directly chromium containing waste streams, which lead to serious problem in environment and human health [4]. Though chromium exists in various oxidation states (from +2 to +6), but trivalent chromium Cr(III) and hexavalent chromium Cr(VI) forms are highly stable [5]. In particular, Cr(VI) species are extremely poisonous, carcinogenic and tough to degrade [6,7]. On the other hand, Cr(III) species are less harmful and easy to remove from water through precipitating as $\text{Cr}(\text{OH})_3$ in neutral or alkaline condition [8,9]. Many researchers have suggested that untreated Cr(VI) attacks on skin, respiratory system, kidneys, eyes, liver and other organs [10]. Hence, increased levels of hexavalent chromium have required to control immediately with a proper green approach and eco-friendly materials.

To date, several treatment techniques including membrane filtration, adsorption, reverse osmosis, photocatalytic reduction, chemical precipitation and ion exchange have been performed for the treatment of Cr(VI) [11]. Among them, the photocatalytic reduction is an efficacious technique for Cr(VI) treatment, because of its unique advantages such as acceptable cost, simple process, less secondary pollution, eco-friendliness and energy saving [12]. In order to effectively reduce Cr(VI) in the wastewater, it is crucial to fabricate cost effective, reasonable and highly efficient photocatalysts. Several types of photocatalysts such as metal oxide, non-metallic substances and heterojunction have been reported for the treatment of Cr(VI) containing waste streams [13].

In recent year, graphitic carbon nitride (g-C₃N₄) is a metal-free visible-light active photocatalyst, which attracts huge interest due to its unique electronic structure, non-toxicity, low cost and favorable stability [14]. Moreover, conduction band potential of g-C₃N₄ is more negative than the reduction edge potential position of Cr⁶⁺/Cr³⁺ [$E^0(\text{Cr}^{6+}/\text{Cr}^{3+}) = +1.23 \text{ V}$ versus NHE], producing that the photo-generated electrons in g-C₃N₄ able to reduce Cr(VI) to Cr(III) [15]. However, pure g-C₃N₄ has poor photocatalytic activity because of its fast recombination rate of e⁻-h⁺ pairs and poor dispersion efficiency [16,17]. So as to overcome these disadvantages of g-C₃N₄, several semiconductors were selected to construct heterojunction composites with g-C₃N₄ for photocatalytic Cr(VI) reduction [12,13,17–20]. Sun et al. (2019) prepared N-TiO₂/g-C₃N₄@diatomite hybrid photocatalyst through impregnation method to enhance the Cr(VI) reduction [17]. Patnaik et al. (2018) fabricated g-C₃N₄/ZnFe₂O₄ photocatalyst, which was applied into efficient photocatalytic Cr (VI) reduction under visible light irradiation [18]. Zhao et al. (2021) synthesized g-C₃N₄/C/Fe₂O₃ photocatalyst for efficient Cr(VI) reduction under artificial solar irradiation [19].

ZnO is a promising photocatalyst owing to lower cost, non-toxicity, high oxidative ability and appropriate band position for redox behavior [21]. High recombination rate of photogenerated charge carriers can decrease the photocatalytic activity of ZnO. Furthermore, ZnO is only active for UV light due to its high band gap. To minimize the high recombination rate of photogenerated charge carriers modification of ZnO nanoparticles, heterostructure with other semiconductor and doping with metals and nonmetals have been widely used [22–25]. Additionally, ZnO can be easier to synthesis by calcination method such as g-C₃N₄, compared with than other oxides [26]. Therefore, combining g-C₃N₄ with ZnO is a facile way to improve the formation of active radical species and separation efficiency of photo-generated of e⁻-h⁺ pairs, resulting to enhanced photocatalytic performance [14]. There are many works reported about the g-C₃N₄/ZnO composite, which mostly emphasize the photocatalytic degradation of

organic pollutants. Contrarily, only few works reported the photocatalytic Cr(VI) reduction by g-C₃N₄/ZnO composite [15,27,28]. Yuan et al. (2016) reported the preparation of g-C₃N₄ nanosheets/ZnO nanocomposites with enhanced photocatalytic Cr(VI) reduction under visible light irradiation [27]. Yan et al. (2019) constructed a few layer g-C₃N₄/flower-like ZnO heterojunction for visible light photocatalytic reduction of Cr(VI) [28]. Liu et al. (2012) prepared g-C₃N₄/ZnO composite with enhanced visible light photooxidation and photoreduction properties [15]. It is noted in these researches that the main component of composites was ZnO. Furthermore, the preparation of reported ZnO/g-C₃N₄ composites were mainly complex processes, in which g-C₃N₄ was prepared firstly and then combined with ZnO. Hence, the fabrication of the ZnO doped g-C₃N₄ by facile and convenient method for Cr(VI) reduction has been rarely reported.

The current work has mainly dealt with a simple and convenient method to prepare ZnO/g-C₃N₄ containing g-C₃N₄ as main component by a single-step calcination and characterized by several techniques. Since there is little information regarding the photocatalytic Cr(VI) reduction with ZnO/g-C₃N₄ with EDTA hole scavenger, the photocatalytic Cr(VI) reduction in presence of EDTA under visible light irradiation was investigated. Moreover, the effects of various factors (solution pH, initial concentration, EDTA concentration, catalytic dosages) on Cr(VI) reduction were systematically studied.

2.2 Experimental

2.2.1 Chemicals

All chemicals were analytical grade, and were used in the experiments without further purification. A standard stock solution of Cr(VI) 1000 µg mL⁻¹ as K₂Cr₂O₇ was bought from FUJIFILM Wako Pure Chemical Crop., Japan. Acetone (C₃H₆O) and disodium ethylenediamine tetraacetic acid (EDTA-2Na) were purchased from Kishida Chemical Co.

Ltd., Japan. Sulphuric acid and 1,5-diphenylcarbazide were obtained in analytical grade from FUJIFILM Wako pure chemical Crop., Japan. The stock solution of 1,5-diphenylcarbazide ($10\text{ }\mu\text{g L}^{-1}$) was prepared from 1 g of 1,5-diphenylcarbazide and 100 mL of acetone, and was used until color change.

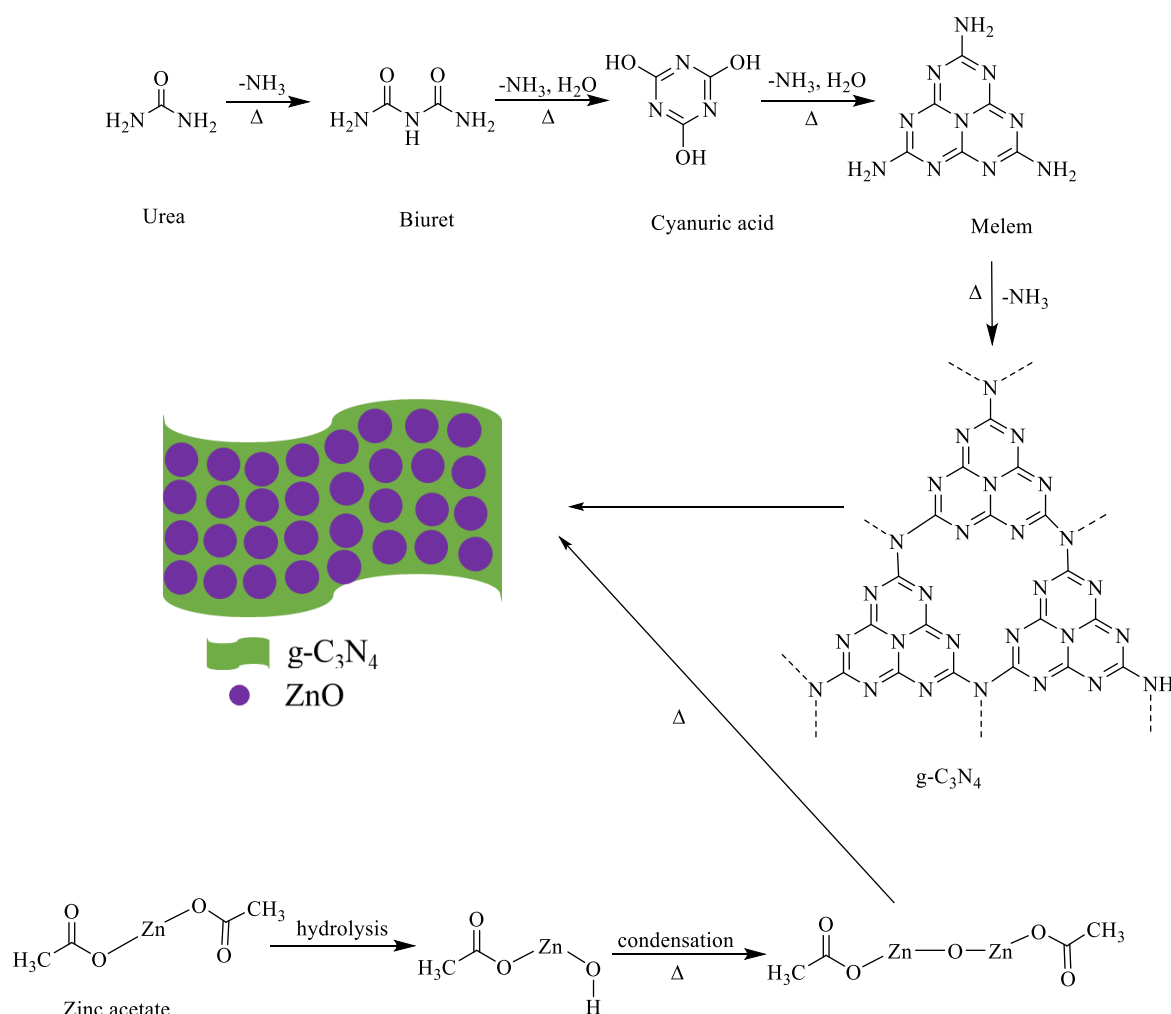
2.2.2 Synthesis of ZnO/g-C₃N₄ Composite

To synthesize ZnO/g-C₃N₄ composite, 20 g of urea and 1 g of zinc acetate dehydrate were put into a porcelain crucible, and 5 mL of pure water was added to make a slurry. After covering, the crucible was placed in an electric furnace and directly heated to 550 °C at 2 °C min⁻¹ heating rate, held at 550 °C for 2 hours, and cooled to room temperature. The dark yellow ZnO/g-C₃N₄ composite was collected and ground into fine powder, and used without any further action. During the formation of the ZnO/g-C₃N₄ composite, stepwise decomposition of urea and zinc acetate are proposed in Scheme 2.1.

In order check the calcination temperature programs the ZnO/g-C₃N₄ composite was also prepared by two-step calcination. Briefly, the first calcination temperature were 100, 200 and 300 °C during 2 hours, followed by a second heating step at 550 °C for 2 hours. Various ZnO doping were fabricated by mixing the amount of zinc acetate dehydrate from 0.1 to 2 g into 20 g of urea using two-step calcination of 200 °C for 2 hours, followed by 550 °C for 2 hours. The heating rates were 2 °C min⁻¹ for two-step calcinations.

2.2.3 Synthesis of ZnO and g-C₃N₄

Pure g-C₃N₄ and ZnO were also synthesized using the same following procedure as above. Briefly, 20 g of urea and 1 g of zinc acetate dehydrate were put into a porcelain crucible, and add 5 mL of water (separately). Then, the crucible was placed in an electric furnace and directly heated at 550 °C for 2 hours with 2 °C min⁻¹ heating rate. The pale yellow g-C₃N₄ and white ZnO were collected and ground into fine powder.



Scheme 2.1 Schematic diagram for the formation of the ZnO/g-C₃N₄ Composite.

2.2.4 Characterization

The synthesized ZnO/g-C₃N₄ composite was characterized by TGA (thermogravimetric analysis), XRD (X-ray Diffraction), FTIR (Fourier Transform Infrared), BET (Brunauer-Emmett-Teller) surface area, SEM (Scanning Electron Microscopy), TEM (Transmission Electron Microscopy), XPS (X-ray Photoelectron Spectroscopy), UV-Visible DRS (Diffuse Reflection Spectroscopy), PL (Photoluminescence) and EIS (Electrochemical Impedance Spectroscopy). Percentage of ZnO content in the synthesized ZnO/g-C₃N₄ composite was analyzed by TGA in the temperature range 25 to 950 °C with heating rate 10°C min⁻¹ in air on the SII EXSTAR 6000 thermal analysis system (TG/DTA 6200, Japan). The XRD patterns

were visualized by Rigaku RINT Ultima-IV diffractometer (Japan) using Cu K α radiation at 2θ range of 10-80° in a scan rate of 0.04°/s. The functional groups of the photocatalyst were measured using SPECTRUM 100 FTIR spectrometer (Perkin Elmer, Japan) with ATR (Attenuated Total Reflection) assembly. The XPS measurement was conducted on a PHI Quantera SXM photoelectron spectrometer (Japan) with Al K α radiation. The N₂ adsorption-desorption isotherms and BJH pore size distributions of photocatalysts were studied by BELSORP-miniII apparatus (MicrotracBEL, Japan). The specific surface area, average pore size and total pore volume were evaluated through the Brunauer-Emmett-Teller (BET) equilibrium equation and Barrett-Joyner-Halenda (BJH) modeling. The UV–visible DRS was performed by a JASCO V-750 UV–visible instrument (Japan) equipped with an integrating sphere attachment, using BaSO₄ as the reference. For PL spectra a Shimadzu RF-5300PC system (Japan) was used at excitation wavelength 340 nm. The EIS measurement was carried out on an electrochemical Versa STAT 3 workstation (Princeton Applied Research, Japan) equipped with a conventional three-electrode system. The working electrode was prepared by coated an FTO glass plate from uniform photocatalyst slurry with nafion solution. As electrolyte 0.5 mol L⁻¹ Na₂SO₄ aqueous solution was used. The electrode made from Pt wire and an Ag/AgCl (saturated KCl) were used as the counter and reference electrodes, respectively.

2.2.5 Photocatalytic Reduction of Cr(VI) to Cr(III)

The photocatalytic reduction reactions were performed in a 50 mL pyrex vessel reactor under visible light irradiation. As the visible light source, a LED (405 nm) light with a UV cut off filter ($\lambda < 400$ nm) was used. First, 40 mg of ZnO/g-C₃N₄ was added into 30 mL aqueous solution of 20 ppm Cr(VI). Then, as a hole scavenger, EDTA (500 ppm) was dispersed in the solution. To achieve adsorption-desorption equilibrium between catalyst and Cr(VI), the suspension was allowed for 30 min in the dark with vigorous stirring. During the photocatalytic

reaction, 1.5 mL of the suspension was collected at 30 min interval for the analysis. The suspension was centrifuged for 4 min to removal the photocatalyst before analysis. The concentration of Cr (VI) was determined using a UV-visible spectrophotometer (AS ONE Corp., ASV11D, Japan) according to 1,5-diphenyl carbazide colorimetric method (Islam et al. 2022). The solution (300 μ L), 2 mol L⁻¹ H₂SO₄ (500 μ L,) and 10 g L⁻¹ 1,5-diphenyl carbazide (200 μ L) were transferred into a 20 mL volumetric flask, diluted with distilled water and left for 5 minutes. Then, the absorbance was measured with a UV-visible spectrophotometer at 540 nm. Lastly, percent of hexavalent chromium Cr(VI) reduction efficiency was determined, according to the equation (2.1).

$$\text{Reduction efficiency (\%)} = \frac{C_0 - C}{C_0} \times 100\% \quad (2.1)$$

where C₀ and C are the concentration of Cr(VI) at time 0 and t, respectively. The reproducibility of the photocatalytic reduction test (relative standard deviation) was within RSD 10% for more than 3 of run numbers.

2.3 Results and Discussion

2.3.1 Structural Investigation of Synthesized Composite

TGA was conducted from room temperature to 950 °C to investigate the thermal stability and exact ZnO content in the synthesized ZnO/g-C₃N₄ composite. The TGA curve shows two weight loss stages (Figure 2.1). The initial weight loss was observed until about 200 °C which could be assigned to the loss of absorbed water on the ZnO/g-C₃N₄ composite surface. The main weight loss was found between 400 to 610 °C for the burning of g-C₃N₄, because ZnO decomposition temperature is higher than 900 °C [29]. From the TGA, the total amount of ZnO was obtained as 30% in the composite.

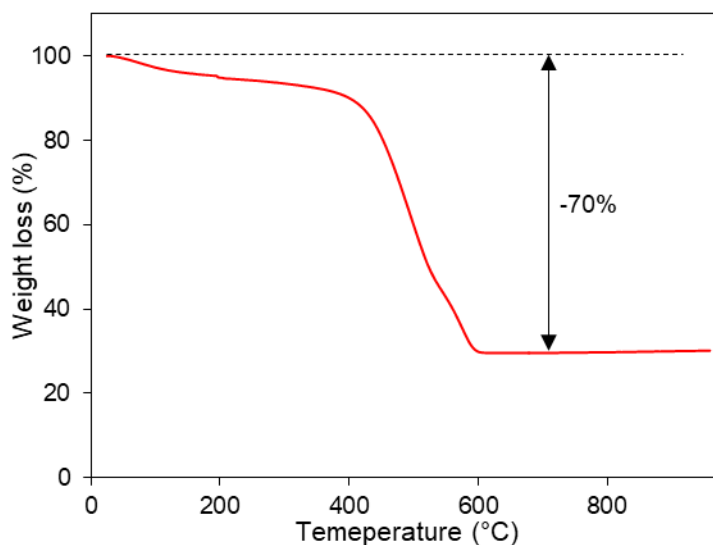


Figure 2.1 TG analysis curve for ZnO/g-C₃N₄ composite until 950 °C at a heating rate of 10 °C min⁻¹.

Figure 2.2a depicts the XRD patterns of ZnO, g-C₃N₄ and ZnO/g-C₃N₄ composite. The diffraction peaks appeared at $2\theta = 31.37^\circ$, 34.4° , 36.22° , 47.54° , 56.60° and 62.8° lead to the staking of the hexagonal wurtzite structure of ZnO, corresponding to the diffraction planes (100), (002), (101), (102), (110) and (103), respectively [30]. Besides, for pure g-C₃N₄ two pronounced diffraction peaks observed at 27.6° and 13.2° can be belonged to planes (002) and (100), respectively. These XRD peaks indicated that pure g-C₃N₄ has inter-planar stacking of the conjugated aromatic system and an in-plane structural packing motif of tri-s-triazine units [31]. However, the diffraction peak could not be observed for ZnO/g-C₃N₄ composite. It indicated that crystal growth of g-C₃N₄ has hampered after the introduction of ZnO [32].

FTIR analysis was carried out to investigate the bonding nature of ZnO, g-C₃N₄ and ZnO/g-C₃N₄ composite (Figure 2.2b). The pure g-C₃N₄ showed an intense band at 811 cm^{-1} due to the out-of plane bending mode of triazine rings [33]. There are several strong bands appeared in the region $1200\text{--}1650\text{ cm}^{-1}$, which attributed to the stretching modes of heterocyclic C–N and C=N bond in g-C₃N₄ [34]. Also, a broad peak appeared at $3000\text{--}3400\text{ cm}^{-1}$ region due

to the N–H stretching of uncondensed amino groups and O–H stretching vibrations which come from absorbed H₂O molecule [35].

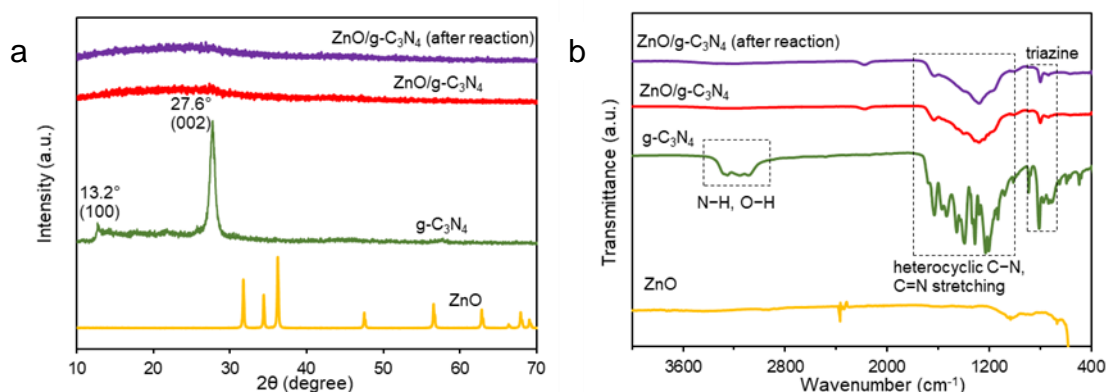


Figure 2.2 (a) XRD patterns and (b) FTIR spectra for ZnO, g-C₃N₄, ZnO/g-C₃N₄ and ZnO/g-C₃N₄ after reaction.

However, FTIR spectra was not clear for ZnO. Further, the ZnO/g-C₃N₄ composite presented a lower peak intensity at 1200-1650 cm⁻¹ which merges into a broad absorption band owing to ZnO crystallization [32]. A new weak peak observed at 2194 cm⁻¹ because ZnO content break the triazine unit (sp² C–N bonds such as N=C–N and C–N=C) and formed new C–N bonds [32]. Compared with pure g-C₃N₄, ZnO/g-C₃N₄ composite shows that the band at 811 cm⁻¹ was red shifted, affirming that strong interaction between g-C₃N₄ and ZnO [36]. The

above analysis confirmed the composition of ZnO/g-C₃N₄.

To examine the surface morphology of the synthesized catalyst ZnO/g-C₃N₄, SEM and TEM were used. Figure 2.3 represents the SEM images of ZnO, g-C₃N₄, ZnO/g-C₃N₄ and ZnO/g-C₃N₄ after reaction. Figure 2.3a showed that the appearance of ZnO is spherical and rod-like structure. The pure g-C₃N₄ exhibited smooth surface with sheet like structure (Figure 2.3b).

In Figure 2.3c it can be seen that when ZnO particles were dispersed on pure g-C₃N₄, the surface of ZnO/g-C₃N₄ became hazy. This SEM image indicated that ZnO particles are covered with g-C₃N₄, which strongly affects the photocatalytic activity of ZnO/g-C₃N₄ [37].

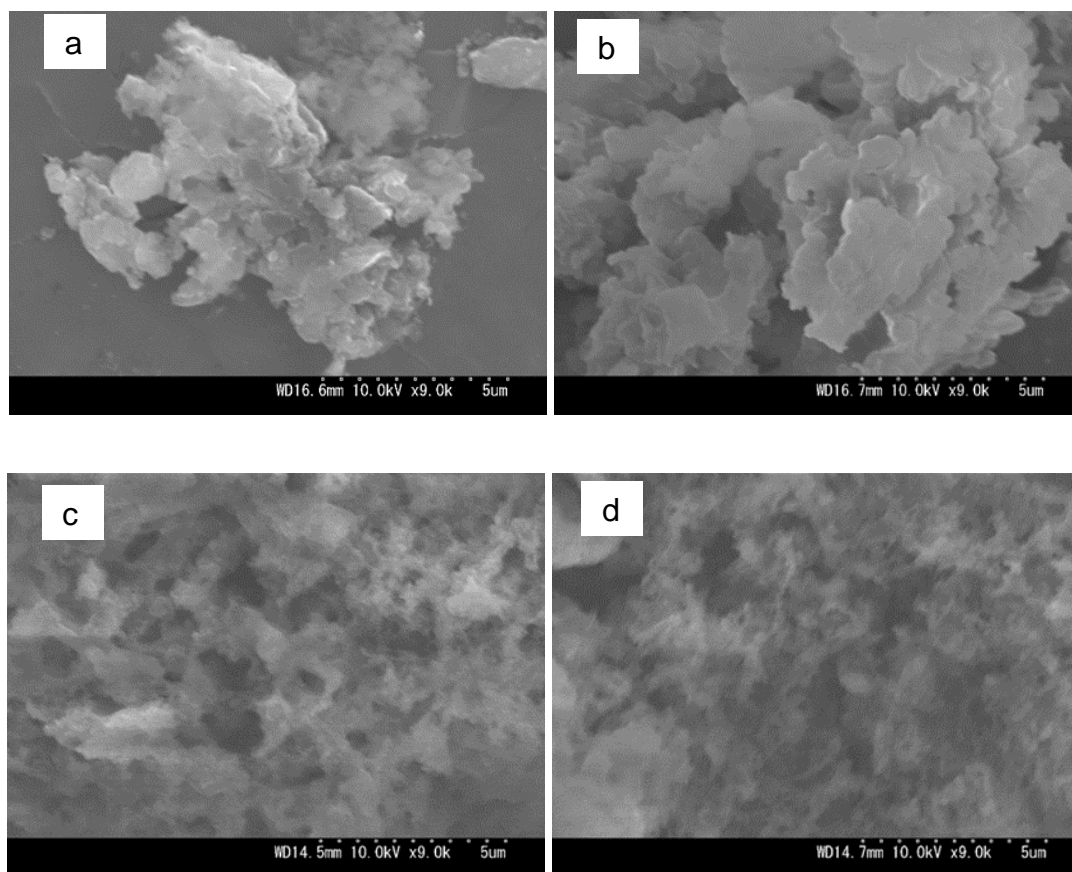


Figure 2.3 SEM images of (a) ZnO, (b) g-C₃N₄, (c) ZnO/g-C₃N₄ and (d) ZnO/g-C₃N₄ after reaction.

Figure 2.4 presents the TEM images of synthesized composite, pure g-C₃N₄ and ZnO. Figures 2.4a and 2.4b illustrated that ZnO has nano-rod with hexagonal shape and sheet like layer structure of g-C₃N₄. Similar surface morphologies of ZnO and g-C₃N₄ were observed in SEM image. In addition, TEM image of ZnO/g-C₃N₄ composite (Figure 2.4c) clearly exhibited that hexagonal ZnO evenly dispersed on the surface of sheet like g-C₃N₄. This image indicated the formation of heterojunctions between the two semiconductors. As a result, since charge transfers are increased, the heterojunctions may improve photocatalytic performance [38,39]. The SEM (Figure 2.3d) and TEM (Figure 2.4d) images of ZnO/g-C₃N₄ after reaction were similar to that of ZnO/g-C₃N₄ before reaction.

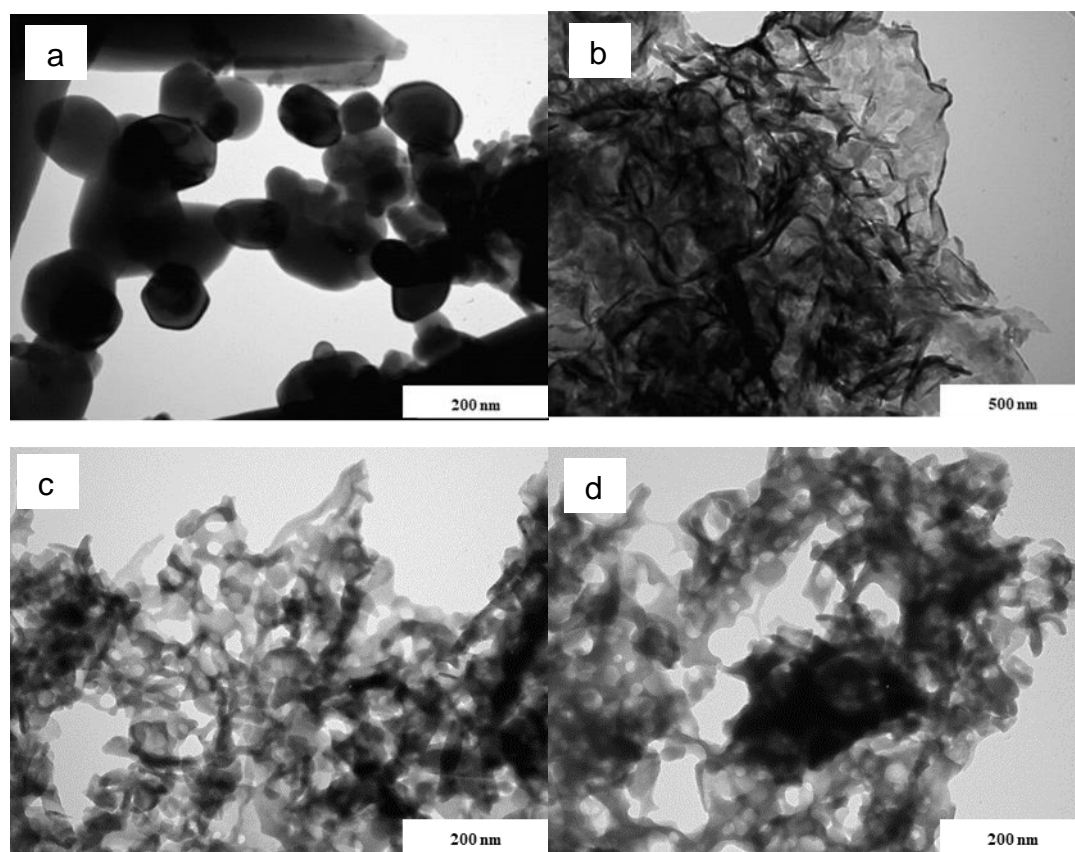


Figure 2.4 TEM images of (a) ZnO, (b) g-C₃N₄, (c) ZnO/g-C₃N₄ and (d) ZnO/g-C₃N₄ after reaction.

XPS was conducted to clarify the surface chemical composition and the presence of ZnO in the composite (Figure 2.5). The survey spectra of ZnO/g-C₃N₄ composite revealed the presence of N, C, O, and Zn elements, signifying the purity of composite (Figure 2.5a). Figure 2.5b demonstrated that the high resolution C 1s spectra of ZnO/g-C₃N₄ is deconvoluted the four peak. The peak at 284.1, 285.3, 287.6 and 289.1 eV corresponded to sp² C=C bond, sp³ C–N bond, sp² bonded C in triazine rings as N=C–N and unavoidable oxidized carbon as O–C=O bond, respectively [30]. In case of N 1s, there are three peaks, as showed in Figure 2.5c. The peak positioned at 398.3 eV is ascribed to C=N–C groups indicating presence of triazine rings. The peak at 399.8 eV can be assigned to the bridging N atoms in N–(C)₃ bond. The peak at 403.8 eV might result from charging effects or positive charge localized in heterocycles [16].

Moreover, the composite showed little chemical shift in the binding energies of C 1s and N 1s spectra, compare with pure g-C₃N₄ (Figures 2.5b and 2.5c). The XPS O 1s spectra represent two peaks located at 531.2 and 532.5 eV due to the O²⁻ ions in Zn–O bond and surface O–H groups or absorbed H₂O of the composite, respectively.

In contrast, for high resolution O 1s spectrum, there was only one peak at 532.2 eV found for pure g-C₃N₄, resulting from absorbed surface H₂O (Figure 2.5d) [40]. For the Zn 2p spectrum (Figure 2.5e), two strong peaks at 1021.8 and 1044.9 eV arisen from Zn 2p_{3/2} and Zn 2p_{1/2}, respectively, indicating Zn–O bonds of the composite which was not observed for pure g-C₃N₄ [26]. The difference in binding energy between Zn 2p_{3/2} and Zn 2p_{1/2} was 23.1 eV, which was in good agreement with standard reference value for ZnO. Also, the presence of Zn LMM auger peaks indicates Zn–N bonds in the composite ZnO/g-C₃N₄ [41]. Therefore, from XPS analysis, it can be assumed that the heterojunction composite formed between two semiconductors of g-C₃N₄ and ZnO.

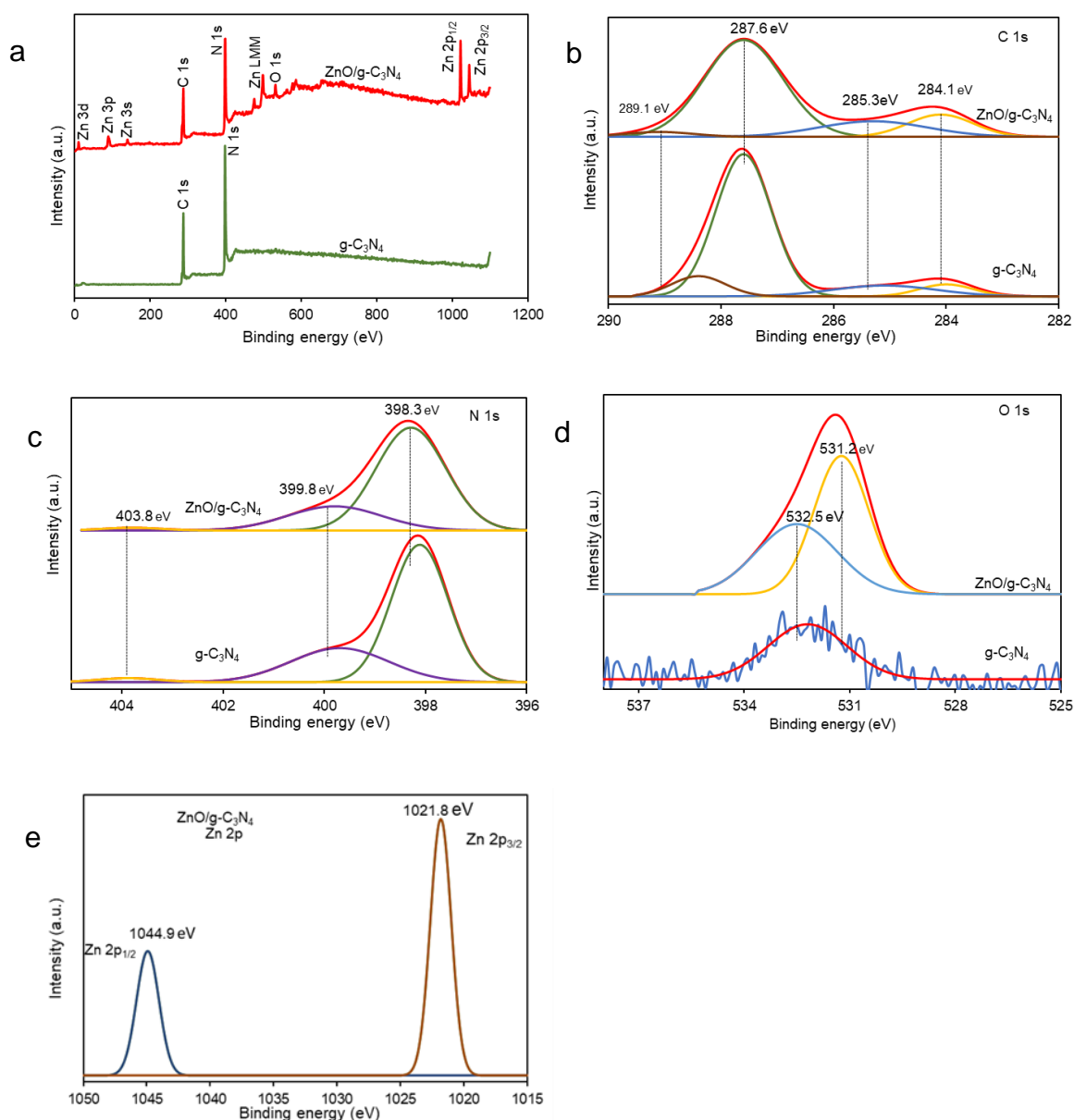


Figure 2.5 XPS spectra of g-C₃N₄, and ZnO/g-C₃N₄ composite. (a) survey spectra of ZnO/g-C₃N₄ composite and g-C₃N₄, high resolution; (b) C1s, (c) N1s, and (d) O1s XPS spectra of ZnO/g-C₃N₄ and g-C₃N₄; (f) Zn 2p peaks of ZnO/g-C₃N₄ composite.

N₂ adsorption-desorption isotherms and BJH pore size distributions were used to inspect surface area and porous nature of the synthesized g-C₃N₄ and composite of ZnO/g-C₃N₄ (Figure 2.6). The adsorption isotherm of g-C₃N₄ and ZnO/g-C₃N₄ composite showed type IV isotherms with H3 hysteresis loops, indicating g-C₃N₄, and ZnO/g-C₃N₄ composite has

mesoporous structure [42]. For comparison, the calculated specific surface area, pore volume and average pore diameter are charted in Table 2.1. From Table 2.1, specific surface area and pore volume of composite ZnO/g-C₃N₄ were lower, however average pore diameter was higher than that of g-C₃N₄, as previously reported [43]. Since ZnO particles showed the silt-like pores of g-C₃N₄, their pores could be evident of strong association between g-C₃N₄ and ZnO.

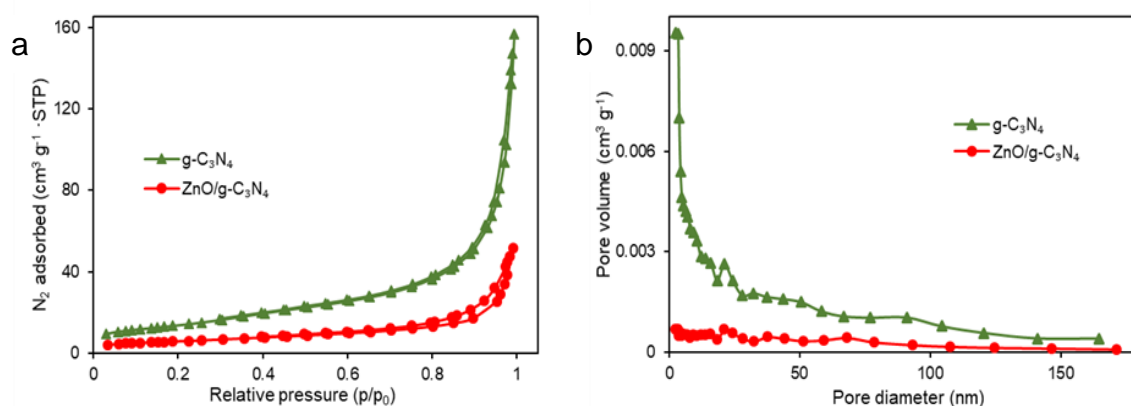


Figure 2.6 (a) N₂ adsorption-desorption isotherms and (b) pore size distribution curves of g-C₃N₄ and ZnO/g-C₃N₄ composite.

Table 2.1 Surface area, pore size and pore volume of the g-C₃N₄ and ZnO/g-C₃N₄ composite

Photocatalyst	BET			BJH		
	S/m ²	V _{pore} /cm ³	D _{pore} /nm	S/m ²	V _{pore} /cm ³	D _{pore} /nm
	g ⁻¹	g ⁻¹	m	g ⁻¹	g ⁻¹	nm
g-C ₃ N ₄	52.9	0.270	16.7	60.9	0.225	2.59
ZnO/g-C ₃ N ₄	21.4	0.0794	14.9	18.0	0.0766	3.32

2.3.2 Optical Properties

UV-visible DRS was performed to investigate the optical absorption properties of

synthesized composites (Figure 2.7). The reflectance spectra were transformed to the absorbance which is based on the Kubelka-Munk equation (Figure 2.7a). The result revealed that pure ZnO has strong adsorption in the ultra-violet region and pure g-C₃N₄ has adsorption wavelength around 430 nm. The adsorption edge of ZnO/g-C₃N₄ was red shifted, indicating that visible light performance of g-C₃N₄ enhanced after the introduction of ZnO [37]. Hence, the optical band gap energy for ZnO, g-C₃N₄ and ZnO/g-C₃N₄ were about 3.20, 2.89 and 2.48 eV from the evaluation using Tauc plots, respectively (Figures 2.7b and 2.7c) [42]. The narrow band gap energy of ZnO/g-C₃N₄ confirmed that the synthesized composite could lead to better charge transfer between g-C₃N₄ and ZnO, resulting improved visible-light photocatalytic activity [32].

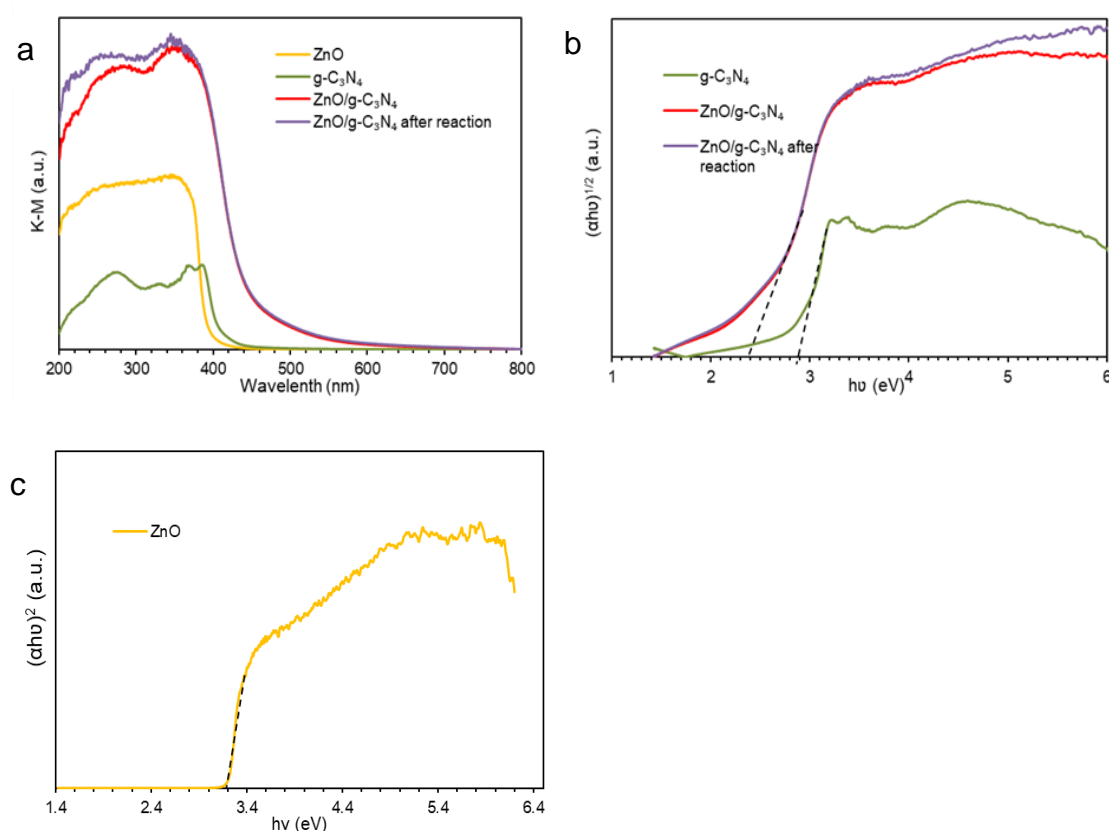


Figure 2.7 (a) UV-visible DRS for ZnO, g-C₃N₄, ZnO/g-C₃N₄ and ZnO/g-C₃N₄ after reaction; and Tauc plot (b) for g-C₃N₄, ZnO/g-C₃N₄, ZnO/g-C₃N₄ after reaction and (c) for ZnO.

To give insight to the charge separation behavior, PL analysis of the photocatalyst were carried out with excitation wavelength of 340 nm (Figure 2.8a). In general, the intensity peak of PL spectra is associated with the recombination process of photogenerated e^-h^+ pairs. The lower intensity signifies the slower photogenerated e^-h^+ pairs recombination [18,44]. ZnO and g-C₃N₄ showed distinct peak intensity, suggesting that rapid recombination of the photo-generated electrons and holes. In contrast, the peak intensity of ZnO/g-C₃N₄ was lowered drastically, indicating that the recombination rate of e^-h^+ pairs was suppressed remarkably and it could improve photocatalytic activity [45,46].

EIS was carried out to investigate the charge transfer behavior of the synthesized photocatalyst. A smaller semicircle implies that charge-transfer resistance is lower at the electrode surface and faster separation of photogenerated e^-h^+ pairs [47]. The results of EIS presented that the radius of the semicircle Nyquist plots of the ZnO/g-C₃N₄ composite was smaller than the radius of pure g-C₃N₄ (Figure 2.8b), illustrating that the composite showed an effective charge separation efficiency of the photogenerated carriers [21]. Therefore, the EIS result was consistent with PL analysis.

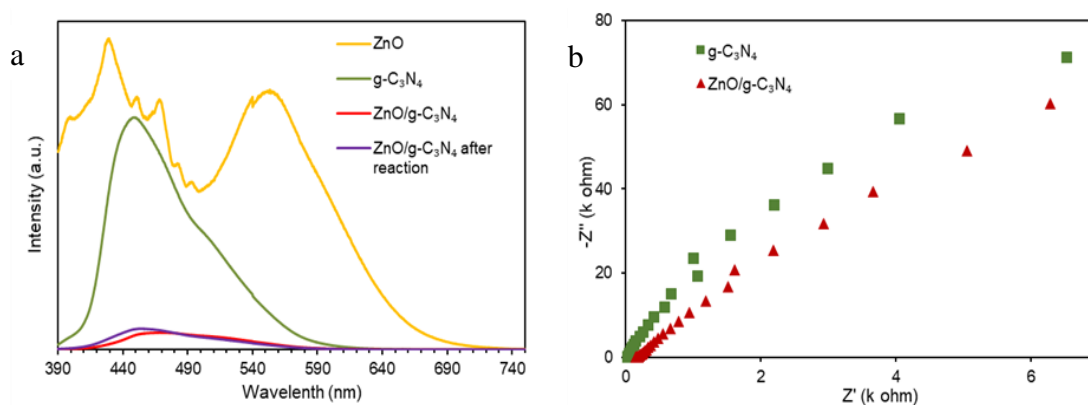


Figure 2.8 (a) Photoluminescence spectra of ZnO, g-C₃N₄, ZnO/g-C₃N₄ and ZnO/g-C₃N₄ after reaction and (b) Nyquist plots of g-C₃N₄ and ZnO/g-C₃N₄.

2.3.3 Photocatalytic Activity

The photocatalytic reduction of Cr(VI) by g-C₃N₄ and ZnO/g-C₃N₄ in the absence and presence of EDTA was scrutinized under visible light irradiation (Figure 2.9a). The result revealed that a negligible Cr(VI) reduction was found with g-C₃N₄ in the absence of EDTA. Also, Cr(VI) reduction was very low with bare ZnO/g-C₃N₄. In the addition of EDTA, the photocatalytic reduction of Cr(VI) was completely observed with ZnO/g-C₃N₄, whereas 79% reduction of Cr(VI) was observed with g-C₃N₄ after 3 hours of visible light irradiation.

The effect of ZnO content on the reduction of Cr(VI) was investigated by varying the amount of zinc acetate (0.1, 0.2, 0.5, 1 and 2 g) as precursor of ZnO (Figure 2.9b). The result showed that ZnO played significant role on the photocatalytic reduction of Cr(VI). In addition, the photocatalytic performance was accelerated by increasing zinc acetate content until 1 g.

However, the photocatalytic performance decreased in the case of 2 g of zinc acetate, indicating that excess amount of ZnO produced can act as the center of e^-h^+ pairs recombination [32]. Consequently, the optimal weight of zinc acetate as ZnO precursor was 1 g in the preparation of ZnO/g-C₃N₄ composite.

During the formation of g-C₃N₄ from urea intermediate compounds cyanic acid, cyanuric acid and melamine may be formed [48,49]. To inspect the effect of intermediate compounds formation on photocatalytic Cr(VI) reduction, the composite was prepared by two-step calcination process at different intermediate temperatures. As shown in Figure 2.9c, the photocatalytic efficiency using the calcination with two steps were similar or worse relative to that with one step, since the mechanism of g-C₃N₄ formation could hardly affect the composite performance. Due to the easy handling, the single-step heating was selected as the optimal calcination process to synthesize the catalyst.

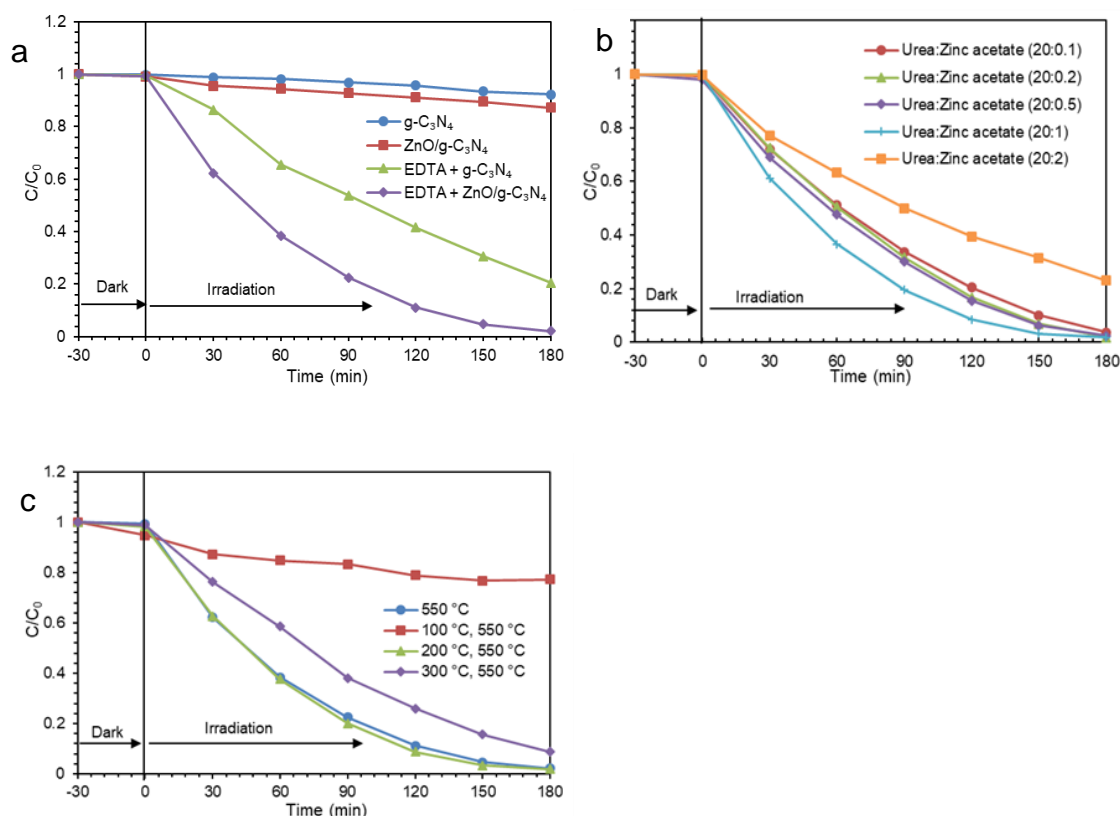


Figure 2.9 (a) Photocatalytic reduction of Cr(VI) with several conditions. (b) Effect of zinc acetate amount as ZnO precursor. (c) Effect of heating temperature programs of the composite. Photocatalytic reduction of Cr(VI) by ZnO/g-C₃N₄ in presence of EDTA; Cr(VI): 20 ppm, EDTA: 500 ppm, ZnO/g-C₃N₄: 40 mg.

The existence of an effective hole scavengers is the important key for the removal of Cr(VI) by photocatalytic reduction. Hence, EDTA was used as hole scavenger. The photocatalytic Cr(VI) reduction and EDTA oxidation was observed with different concentrations of EDTA, as shown in Figure 2.10a. In the absent of EDTA, the photocatalytic reduction efficiency of Cr(VI) with ZnO/g-C₃N₄ was very low after 3 hours of visible light irradiation. The results may be due to a variety of reasons such as re-oxidation of Cr(III) to Cr(VI) or the rapid electron-hole pair recombination by oxidizing agent ($\bullet OH$). The oxidizing agent can be produced when holes are react with water [50,51]



The photocatalytic reduction efficiency of Cr(VI) significantly increased, when the hole scavenger EDTA was added. With increasing the initial concentration of EDTA from 100 to 500 ppm, the photocatalytic Cr(VI) reduction increased from 60% to 98%. This fact was ascribed to it that EDTA has advantage of consuming holes produced in valance band and inhibited $\text{e}^- - \text{h}^+$ pair recombination. Thus, the electrons of conduction band can contribute to the reduction of Cr(VI) [11]. However, the photocatalytic reduction of Cr(VI) and oxidation of EDTA slightly decreased after the addition of EDTA of more than 500 ppm. The reason may be owing to it that ZnO/g-C₃N₄ particles are covered by the high concentration of EDTA molecules instead of chromium [52].

In order to illustrate the reaction kinetics, the photocatalytic reduction of Cr(VI) has been analyzed by Langmuir-Hinshelwood model. The plots of $\ln(C_0/C)$ versus irradiation time (min) for Cr(VI) reduction displayed in Figure 2.10b, which exhibits linear relationship. The linear fitting curve observed here represented that the photocatalytic reduction of Cr(VI) obeys the pseudo-first-order kinetics [15,53]. The kinetic equation can be expressed by equation (2.5).

$$\ln C_0/C = kt \quad (2.5)$$

where C_0 is the initial concentration of Cr(VI) and C is the concentration of Cr(VI) at time t . Then, k is the apparent reaction rate constant, which can be computed from the slop of the linear correlation. The reaction rate constants, half-life of substrate and correlation coefficients (R^2) are listed in Table 2.2. From Table 2.2, it was found that with increasing EDTA concentration from 0 to 500 ppm, the reaction rate constant was increased from 7×10^{-4} to

$1.75 \times 10^{-2} \text{ min}^{-1}$. Over the value, the reaction rate slightly decreased at the EDTA concentration of 1000 ppm.

Table 2.2 Kinetic parameters for the photocatalytic reduction of Cr(VI)

Concentration of EDTA (ppm)	Rate constant (min^{-1})	$t_{1/2}$ (min)	R^2
0	7×10^{-4}	990.0	0.9287
100	5.3×10^{-3}	130.8	0.8517
250	1.17×10^{-2}	59.2	0.9996
300	1.3×10^{-2}	53.3	0.9922
500	1.75×10^{-2}	39.6	0.9917
1000	1.63×10^{-2}	42.5	0.9938

To appraise the effect of the catalyst dose, photocatalytic reduction of Cr(VI) was studied by varying the catalyst amount from 10 to 50 mg. The results are shown in Figure 2.10c. With increasing catalyst amount from 10 to 40 mg, the photocatalytic Cr(VI) reduction increased from 87% to 98%. Then, the efficiency decreased to 96% when the catalyst amount was 50 mg. The available free active site is fewer at lower amount of catalyst. Because the active sites are increased by increasing catalyst dose, the photocatalytic Cr(VI) reduction could enhance [54]. However, when the photocatalyst was overdosed, the number of active sites on the photocatalyst may become almost constant due to the scattering of light photons and poor light penetration through the catalyst surface [55]. Therefore, in the view point of cost-effective reason, 40 mg of catalyst was chosen as optimum amount.

To evaluate the optimized value of Cr(VI) concentration, the photocatalytic performance of the prepared ZnO/g-C₃N₄ was studied on various initial concentration of Cr(VI) with 5 to 30 ppm. Figure 2.10d shows the highest reduction was achieved in the case with the initial concentration of 20 ppm. It was observed that photocatalytic Cr(VI) reduction increases with the increasing of initial concentration of Cr(VI) from 5 to 20 ppm. The results may be due to it that with increasing the Cr concentration the adsorption and mass transfer of Cr raise

[5,56]. However, with the further increasing of initial concentration of Cr(VI) to 30 ppm, Cr(VI) reduction decreases. At higher initial concentration of Cr(VI), the decrease in reduction efficiency may be owing to the saturation of Cr adsorption [55]. On the other hand, the reduction amount of chromium increased with the increasing initial concentration of Cr(VI) (Figure 2.10e).

The initial pH value shows notable influence on photocatalytic reduction. At various initial pH values (pH=2, 3, 4, 6, 8), the photocatalytic reduction of Cr(VI) was studied (Figure 2.10f). It was observed that best results was achieved in acidic condition (at pH 2). The photocatalytic reduction efficiency decreased with increasing pH value. The photocatalytic Cr(VI) reduction efficiency at pH 2 was obtained 98% after 2 hours irradiation. The reduction efficiencies decreased with pH after 3 hours irradiation. Normally, in the aqueous solution, Cr(VI) ions exist in form of $\text{H}_2\text{CrO}_4(\text{aq})$, HCrO_7^- , $\text{Cr}_2\text{O}_7^{2-}$, HCrO_4^- , and CrO_4^{2-} at different pH [57]. It has been reported that HCrO_7^- and $\text{Cr}_2\text{O}_7^{2-}$ are the stable forms of Cr(VI) under acidic conditions while CrO_4^{2-} is stable form at alkaline conditions [5,58].

The photocatalytic Cr(VI) reduction is as follows:



The effect of pH indicated that as per Le Chatelier's principle acidic pH (i.e., more H^+ , less OH^-) favors the reduction of Cr(VI) to Cr(III) [47]. Because at lower pH the $\text{ZnO/g-C}_3\text{N}_4$ were positively charged due to the adsorption of excess of H^+ ions, the photocatalyst surface electrostatically attracted to negatively charged $\text{Cr}_2\text{O}_7^{2-}$ and CrO_4^{2-} , giving the enhanced photocatalytic Cr(VI) reduction. Contrary, in alkaline medium photocatalytic Cr(VI) reduction declined since $\text{ZnO/g-C}_3\text{N}_4$ surfaces acquired negative charge due to the adsorption of OH^- ,

which could repel electrostatically $\text{Cr}_2\text{O}_7^{2-}$ and CrO_4^{2-} [59,60]. Furthermore, in alkaline medium, the formation of $\text{Cr}(\text{OH})_3$ on the photocatalyst surface could block active sites of the catalyst, resulting in the decline of the photocatalytic reduction performance [47,61].

The photocatalyst stability during repeated photocatalytic process is an essential factor for practical application. Hence, the stability of $\text{ZnO/g-C}_3\text{N}_4$ composite was studied for the photocatalytic reduction of $\text{Cr}(\text{VI})$ in presence of EDTA under visible light irradiation up to fifth runs. As given in Figure 2.10 g, a slight decrease in catalytic efficiency was observed after the fifth run. The decrease in photocatalytic performance may be due to the minor surface modification or intermediate formed on the surface of the heterostructure composite. Additionally, XRD, FTIR, DRS, PL spectra of $\text{ZnO/g-C}_3\text{N}_4$ composite scarcely has the obvious difference between before and after photocatalytic reaction. The SEM and TEM images of $\text{ZnO/g-C}_3\text{N}_4$ composite before and after photocatalytic reaction are almost same. These results indicated that $\text{ZnO/g-C}_3\text{N}_4$ composite has good stability in photocatalytic reduction.

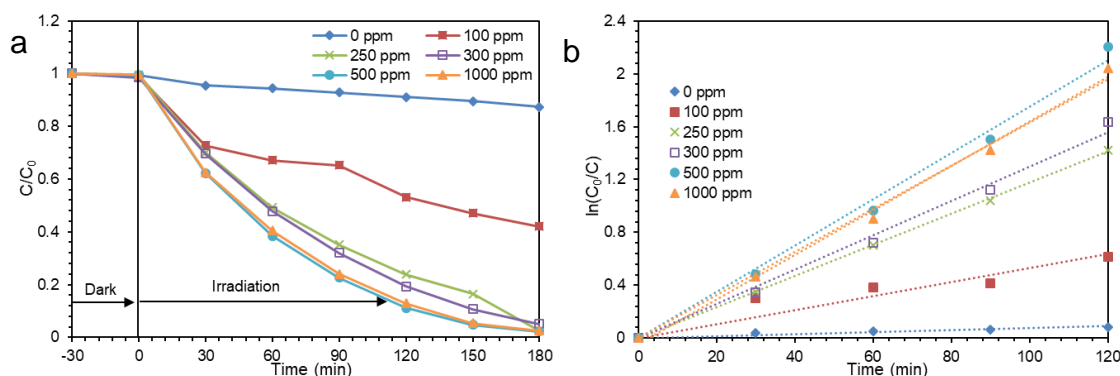


Figure 2.10 Effect of (a) concentration of EDTA and (b) Plot of $\ln(C_0/C)$ verses irradiation time at different concentration of EDTA on the photocatalytic reduction of $\text{Cr}(\text{VI})$ by $\text{ZnO/g-C}_3\text{N}_4$ in the presence of EDTA.

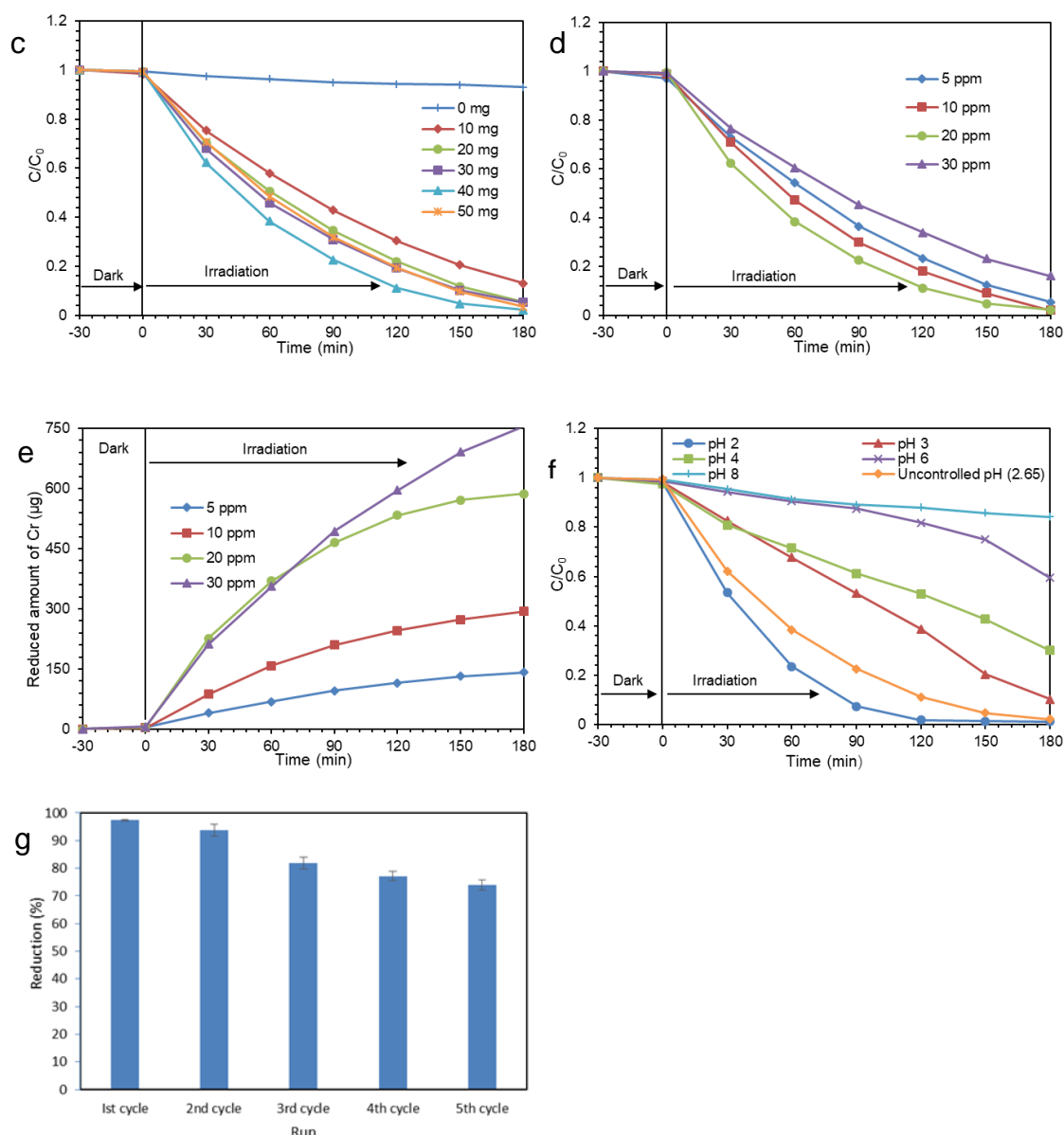


Figure 2.10 Effect of (c) photocatalyst dosage, (d) initial concentration of Cr(VI) and (f) initial pH on the photocatalytic Cr(VI) reduction by ZnO/g-C₃N₄. (e) Reduced amount of Cr at different concentrations of Cr(VI) on the photocatalytic reduction of Cr(VI) by ZnO/g-C₃N₄ in the presence of EDTA. (g) Reusability of ZnO/g-C₃N₄.

The photocatalytic Cr(VI) reduction efficiency of synthesized ZnO/g-C₃N₄ composite in the present study is compared with previous reports (Table 2.3). From Table 2.3, it is observed that the synthesized ZnO/g-C₃N₄ composite in present study showed excellent photocatalytic activity compared to other composites.

Table 2.3 Photocatalytic reduction of Cr(VI) activity of synthesized ZnO/g-C₃N₄ composite and some other reported composite

Photocatalyst (Scavenger)	Cr(VI) solution (mg L ⁻¹)	light	Irradiation time (min)	% of Reduction	Rate constant (min ⁻¹)	Reusability	References
ZnO/g-C ₃ N ₄ (EDTA)	20	Visible	180	98	0.0175	5	Current Study
g-C ₃ N ₄ nanosheets/ZnO	-	Visible	240	70	-	5	[27]
g-C ₃ N ₄ /ZnO	6.5	Visible	100	75.5	-	5	[15]
few layer g-C ₃ N ₄ /flower-like ZnO	10	Visible	120	95	-	5	[28]
N-TiO ₂ / g-C ₃ N ₄ diatomite	5	Visible	300	-	0.0100	-	[17]
Ag-modified g-C ₃ N ₄ (EDTA)	10	UV	120	100	0.1200	-	[16]

2.3.4 Possible Reaction Mechanisms

The photocatalytic performance of the synthesized composite ZnO/g-C₃N₄ is interpreted by Figure 2.12. If the photocatalyst is irradiated by visible light, it absorbs incident energy of a photon and produces conduction band electrons (e⁻) and valance band holes (h⁺). It is known that photocatalytic activity is related with the band gap structure of the photocatalyst. Therefore, it is essential to elucidate the conduction band and valence band of the photocatalyst. It was observed that the band gap energies (E_g) of ZnO, g-C₃N₄ and ZnO/g-C₃N₄ were about 3.20, 2.89, and 2.38 eV, respectively (Figure 2.7). On the other hand, from valance band XPS (VB XPS), VB edge potential of composite was found as about +1.7 eV (Figure 2.11). The contact potential difference between sample and analyzer were evaluated based on the equation (2.9) [62].

$$E_{NHE}/V = \Phi_{WF} + \Phi_{sample} - 4.44 \quad (2.9)$$

where, E_{NHE} , Φ_{WF} , and Φ_{sample} are the VB potential of the sample, electron work function of the analyzer (4.33 eV) and VB position of the sample (eV) determined using VB-XPS, respectively. Therefore, the VB edge potential of composite was estimated as +1.59 eV.

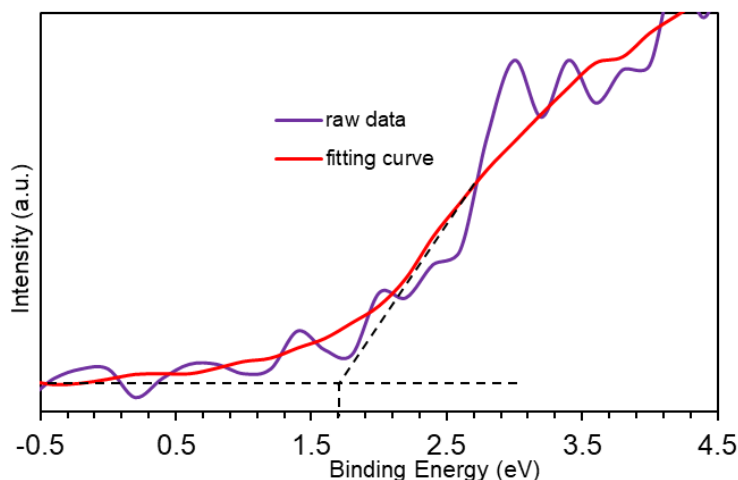


Figure 2.11 VB XPS spectra of ZnO/g-C₃N₄ composite.

Furthermore, when the ZnO deposited on the g-C₃N₄, electrons of g-C₃N₄ shifted to ZnO through the interface until their fermi level energies are equal [63,64]. After that, an intermediate band in the mid band gap may be aroused in the composite. The intermediate band position might be equal to the CB edge potential (E_{CB}) of ZnO. Hence, the conduction band edge potential (E_{CB}) of g-C₃N₄ and intermediate band position as well as E_{CB} of ZnO can be calculated by the equation (2.10).

$$E_{CB} = E_{VB} - E_g \quad (2.10)$$

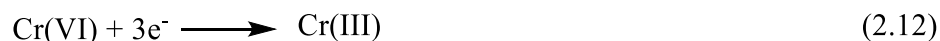
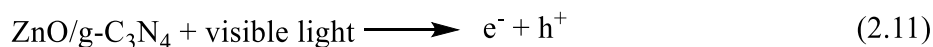
where, E_g is the band gap energy [62].

The E_{CB} of g-C₃N₄ were determined as -1.30 eV. The intermediate band energy position of the composite was calculated as -0.79 eV, which is equal to E_{CB} of ZnO. The E_{VB} of ZnO was evaluated as 2.41 eV.

According to the above experimental results, the possible two mechanisms are proposed for the photocatalytic reduction of Cr(VI) by ZnO/g-C₃N₄ composite. First, the typical charge transfer mechanism is shown in Figure 2.12a. Briefly, the position of CB edge potential of g-C₃N₄ is more negative than that of ZnO. Hence, the photogenerated CB electrons of g-C₃N₄ rapidly transferred to CB of ZnO. These accumulated electrons on the CB of ZnO can readily reduce Cr(VI) into Cr(III), because the reduction edge potential position of Cr⁶⁺/Cr³⁺ [E^0 (Cr⁶⁺/Cr³⁺) = +1.23 V versus NHE] [15].

The proposed possible second mechanism is shown in Figure 2.12b. In short, after visible light irradiation, VB electrons of g-C₃N₄ are migrated to the intermediate band energy of the composite through interfacial charge transfer (IFCT) mechanism. Furthermore, the electrons are transferred to the CB of ZnO. These aggregated electrons on the CB of ZnO can reduce Cr(VI) into Cr(III).

Moreover, when EDTA was added to the photocatalytic process for both mechanisms, EDTA can capture generated holes and restrain the fast photogenerated e^-h^+ pairs recombination. After completing the reaction, the pale pink color of the solution after 3 hours signifies that Cr(VI) was reduced to Cr(III) and [Cr(III)–EDTA] complex was formed by the complexation of reduced Cr(III) and EDTA [16]. The related photocatalytic reactions of Cr(VI) reduction with ZnO/g-C₃N₄ composite under visible light irradiation are expressed as following reactions:



In addition, O₂ species may exist in the reaction process. CB electrons of ZnO are reacted with environmental O₂ and yields $\cdot\text{O}_2^-$ radicals, because of edge potential difference [$E^0(\text{O}_2/\cdot\text{O}_2^-) = -0.33$ eV versus NHE]. $\cdot\text{O}_2^-$ radicals produced from the reduction of O₂ by photoelectrons increase Cr(VI) reduction as following reactions [65].



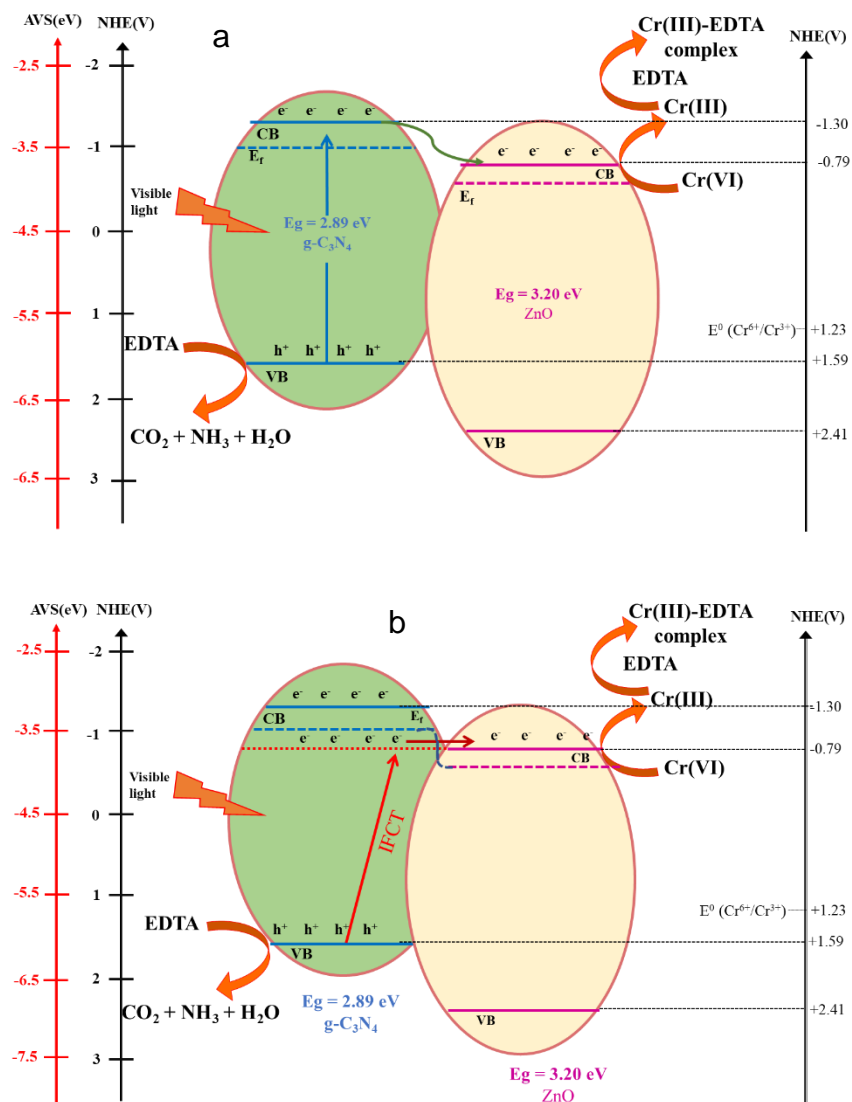


Figure 2.12 Proposed mechanisms for photocatalytic reduction of Cr(VI) by ZnO/g-C₃N₄ in presence of EDTA.

2.4 Conclusions

The photocatalytic reduction of Cr(VI) in presence of EDTA under illumination of visible light can be enhanced by using ZnO/g-C₃N₄. TGA, XRD, FTIR, SEM, TEM, XPS, BET and BJH analysis clearly suggested that the ZnO/g-C₃N₄ composite was successfully synthesized. In

addition, narrow band gap, lower PL intensity and smaller arc radius were analyzed by UV-visible DRS, PL and EIS measurement, respectively. The evidence indicated the improved photocatalytic activity of ZnO/g-C₃N₄ was attributed to the higher charge separation and lower electron-hole pairs recombination. The photocatalytic efficiency of Cr(VI) by ZnO/g-C₃N₄ was significantly better than that obtained with pure g-C₃N₄. Moreover, the photocatalyst has good recyclability and photostability.

2.5 References

1. Diao, Z.-H.; Yan, L.; Dong, F.-X.; Chen, Z.-L.; Guo, P.-R.; Qian, W.; Zhang, W.-X.; Liang, J.-Y.; Huang, S.-T.; Chu, W. Ultrasound-Assisted Catalytic Reduction of Cr(VI) by an Acid Mine Drainage Based nZVI Coupling with FeS₂ System from Aqueous Solutions: Performance and Mechanism. *J. Environ. Manage.* **2021**, *278*, 111518, doi:10.1016/j.jenvman.2020.111518.
2. Fu, R.; Yang, Y.; Xu, Z.; Zhang, X.; Guo, X.; Bi, D. The Removal of Chromium (VI) and Lead (II) from Groundwater Using Sepiolite-Supported Nanoscale Zero-Valent Iron (S-NZVI). *Chemosphere* **2015**, *138*, 726–734, doi:10.1016/j.chemosphere.2015.07.051.
3. Ali, I.; Kim, J.-O. Visible-Light-Assisted Photocatalytic Activity of Bismuth-TiO₂ Nanotube Composites for Chromium Reduction and Dye Degradation. *Chemosphere* **2018**, *207*, 285–292, doi:10.1016/j.chemosphere.2018.05.075.
4. Prabakaran, E.; Pillay, K. Self-Assembled Silver Nanoparticles Decorated on Exfoliated Graphitic Carbon Nitride/Carbon Sphere Nanocomposites as a Novel Catalyst for Catalytic Reduction of Cr(VI) to Cr(III) from Wastewater and Reuse for Photocatalytic Applications. *ACS Omega* **2021**, *6*, 35221–35243, doi:10.1021/acsomega.1c00866.
5. Murali, A.; Sarswat, P.K.; Free, M.L. Adsorption-Coupled Reduction Mechanism in ZnO-Functionalized MWCNTs Nanocomposite for Cr (VI) Removal and Improved Anti-Photocorrosion for Photocatalytic Reduction. *J. Alloys Compd.* **2020**, *843*, 155835, doi:10.1016/j.jallcom.2020.155835.
6. Arputharaj, E.; Kumar, A.S.K.; Tseng, W.-L.; Jiang, S.-J.; Huang, Y.-L.; Dahms, H.-U. Self-Assembly of Poly(ethyleneimine)-Modified g-C₃N₄ Nanosheets with Lysozyme Fibrils for Chromium Detoxification. *Langmuir* **2021**, *37*, 7147–7155,

- doi:10.1021/acs.langmuir.1c00716.
7. Zhao, Z.; An, H.; Lin, J.; Feng, M.; Murugadoss, V.; Ding, T.; Liu, H.; Shao, Q.; Mai, X.; Wang, N.; et al. Progress on the Photocatalytic Reduction Removal of Chromium Contamination. *Chem. Rec.* **2019**, *19*, 873–882, doi:10.1002/tcr.201800153.
 8. Djellabi, R.; Ghorab, F.M.; Nouacer, S.; Smara, A.; Khireddine, O. Cr(VI) Photocatalytic Reduction under Sunlight Followed by Cr(III) Extraction from TiO₂ Surface. *Mater. Lett.* **2016**, *176*, 106–109, doi:10.1016/j.matlet.2016.04.090.
 9. Dong, Y.; Wang, P.; Gan, L.; Li, B.; Wen, H. Enhanced Removal of Aqueous Cr(VI) Using Optimized Fe Complex on EDTA Modified Cotton Fiber via Photocatalytic Reduction and Adsorption Hybrid Functions. *Cellulose* **2019**, *26*, 7383–7397, doi:10.1007/s10570-019-02598-4.
 10. Naimi-Joubani, M.; Shirzad-Siboni, M.; Yang, J.-K.; Gholami, M.; Farzadkia, M. Photocatalytic Reduction of Hexavalent Chromium with Illuminated ZnO/TiO₂ Composite. *J. Ind. Eng. Chem.* **2015**, *22*, 317–323, doi:10.1016/j.jiec.2014.07.025.
 11. Liu, B.; Wu, Y.; Han, X.; Lv, J.; Zhang, J.; Shi, H. Facile Synthesis of g-C₃N₄/amine-Functionalized MIL-101(Fe) Composites with Efficient Photocatalytic Activities under Visible Light Irradiation. *J. Mater. Sci. Mater. Electron.* **2018**, *29*, 17591–17601, doi:10.1007/s10854-018-9862-x.
 12. Song, X.-Y.; Chen, Q.-L. Facile Preparation of g-C₃N₄/Bi₂WO₆ Hybrid Photocatalyst with Enhanced Visible Light Photoreduction of Cr(VI). *J. Nanoparticle Res.* **2019**, *21*, 183, doi:10.1007/s11051-019-4632-0.
 13. He, H.; Li, J.; Yu, C.; Luo, Z. Surface Decoration of Microdisk-like g-C₃N₄/diatomite with Ag/AgCl Nanoparticles for Application in Cr(VI) Reduction. *Sustain. Mater. Technol.*

- 2019**, 22, e00127, doi:10.1016/j.susmat.2019.e00127.
14. Qamar, M.A.; Javed, M.; Shahid, S.; Sher, M. Fabrication of g-C₃N₄/transition Metal (Fe, Co, Ni, Mn and Cr)-Doped ZnO Ternary Composites: Excellent Visible Light Active Photocatalysts for the Degradation of Organic Pollutants from Wastewater. *Mater. Res. Bull.* **2022**, 147, 111630, doi:10.1016/j.materresbull.2021.111630.
 15. Liu, W.; Wang, M.; Xu, C.; Chen, S. Facile Synthesis of g-C₃N₄/ZnO Composite with Enhanced Visible Light Photooxidation and Photoreduction Properties. *Chem. Eng. J.* **2012**, 209, 386–393, doi:10.1016/j.cej.2012.08.033.
 16. Islam, J.B.; Islam, M.R.; Furukawa, M.; Tateishi, I.; Katsumata, H.; Kaneco, S. Ag-Modified g-C₃N₄ with Enhanced Activity for the Photocatalytic Reduction of Hexavalent Chromium in the Presence of EDTA under Ultraviolet Irradiation. *Environ. Technol.* **2022**, doi:10.1080/09593330.2022.2068379.
 17. Sun, Q.; Hu, X.; Zheng, S.; Zhang, J.; Sheng, J. Effect of Calcination on Structure and Photocatalytic Property of N-TiO₂/g-C₃N₄@diatomite Hybrid Photocatalyst for Improving Reduction of Cr(VI). *Environ. Pollut.* **2019**, 245, 53–62, doi:10.1016/j.envpol.2018.10.121.
 18. Patnaik, S.; Das, K.K.; Mohanty, A.; Parida, K. Enhanced Photo Catalytic Reduction of Cr (VI) over Polymer-Sensitized g-C₃N₄/ZnFe₂O₄ and Its Synergism with Phenol Oxidation under Visible Light Irradiation. *Catal. Today* **2018**, 315, 52–66, doi:10.1016/j.cattod.2018.04.008.
 19. Zhao, L.; Guo, L.; Tang, Y.; Zhou, J.; Shi, B. Novel g-C₃N₄/C/Fe₂O₃ Composite for Efficient Photocatalytic Reduction of Aqueous Cr(VI) under Light Irradiation. *Ind. Eng. Chem. Res.* **2021**, 60, 13594–13603, doi:10.1021/acs.iecr.1c02411.
 20. Yi, X.-H.; Ma, S.-Q.; Du, X.-D.; Zhao, C.; Fu, H.; Wang, P.; Wang, C.-C. The Facile

- Fabrication of 2D/3D Z-Scheme g-C₃N₄/UiO-66 Heterojunction with Enhanced Photocatalytic Cr(VI) Reduction Performance under White Light. *Chem. Eng. J.* **2019**, 375, 121944, doi:10.1016/j.cej.2019.121944.
21. Kalisamy, P.; Hossain, M.S.; Macadangdang Jr., R.R.; Madhubala, V.; Palanivel, B.; Venkatachalam, M.; Massoud, E.E.S.; Sreedevi, G. ZnO Coupled F-Doped g-C₃N₄: Z-Scheme Heterojunction for Visible-Light Driven Photocatalytic Degradation Reaction. *Inorg. Chem. Commun.* **2022**, 135, 109102, doi:10.1016/j.inoche.2021.109102.
 22. Singh, J.; Soni, R.K. Efficient Charge Separation in Ag Nanoparticles Functionalized ZnO nanoflakes/CuO Nanoflowers Hybrids for Improved Photocatalytic and SERS Activity. *Colloids Surfaces A Physicochem. Eng. Asp.* **2021**, 626, 127005, doi:10.1016/j.colsurfa.2021.127005.
 23. Singh, J.; Soni, R.K. Controlled Synthesis of CuO Decorated Defect Enriched ZnO Nanoflakes for Improved Sunlight-Induced Photocatalytic Degradation of Organic Pollutants. *Appl. Surf. Sci.* **2020**, 521, 146420, doi:10.1016/j.apsusc.2020.146420.
 24. Singh, J.; Kumar, S.; Rishikesh; Manna, A.K.; Soni, R.K. Fabrication of ZnO–TiO₂ Nanohybrids for Rapid Sunlight Driven Photodegradation of Textile Dyes and Antibiotic Residue Molecules. *Opt. Mater. (Amst.)* **2020**, 107, 110138, doi:10.1016/j.optmat.2020.110138.
 25. Singh, J.; Juneja, S.; Palsaniya, S.; Manna, A.K.; Soni, R.K.; Bhattacharya, J. Evidence of Oxygen Defects Mediated Enhanced Photocatalytic and Antibacterial Performance of ZnO Nanorods. *Colloids Surfaces B Biointerfaces* **2019**, 184, 110541, doi:10.1016/j.colsurfb.2019.110541.
 26. Zhang, S.; Su, C.; Ren, H.; Li, M.; Zhu, L.; Ge, S.; Wang, M.; Zhang, Z.; Li, L.; Cao, X.

- In-Situ Fabrication of g-C₃N₄/ZnO Nanocomposites for Photocatalytic Degradation of Methylene Blue: Synthesis Procedure Does Matter. *Nanomaterials* **2019**, 9, 215, doi:10.3390/nano9020215.
27. Yuan, X.; Zhou, C.; Jing, Q.; Tang, Q.; Mu, Y.; Du, A.-K. Facile Synthesis of G-C₃N₄ nanosheets/ZnO Nanocomposites with Enhanced Photocatalytic Activity in Reduction of Aqueous chromium(VI) under Visible Light. *Nanomaterials* **2016**, 6, 173, doi:10.3390/nano6090173.
 28. Yan, X.; Li, J.; Ai, T.; Su, X.; Wang, Z.; Zhao, P. Few Layer G-C₃N₄ Decorated Flower-like ZnO for Visible Light Photocatalytic Reduction of Cr(VI). *J. Mater. Sci. Mater. Electron.* **2019**, 30, 8577–8584, doi:10.1007/s10854-019-01178-3.
 29. Li, L.; Sun, S.-Q.; Wang, Y.-X.; Wang, C.-Y. Facile Synthesis of ZnO/g-C₃N₄ Composites with Honeycomb-like Structure by H₂ Bubble Templates and Their Enhanced Visible Light Photocatalytic Performance. *J. Photochem. Photobiol. A Chem.* **2018**, 355, 16–24, doi:10.1016/j.jphotochem.2017.12.016.
 30. Ismael, M. The Photocatalytic Performance of the ZnO/g-C₃N₄ Composite Photocatalyst toward Degradation of Organic Pollutants and Its Inactivity toward Hydrogen Evolution: The Influence of Light Irradiation and Charge Transfer. *Chem. Phys. Lett.* **2020**, 739, 136992, doi:10.1016/j.cplett.2019.136992.
 31. Sun, Q.; Sun, Y.; Zhou, M.; Cheng, H.; Chen, H.; Dorus, B.; Lu, M.; Le, T. A 2D/3D G-C₃N₄/ZnO Heterojunction Enhanced Visible-Light Driven Photocatalytic Activity for Sulfonamides Degradation. *Ceram. Int.* **2022**, 48, 7283–7290, doi:10.1016/j.ceramint.2021.11.289.
 32. Paul, D.R.; Gautam, S.; Panchal, P.; Nehra, S.P.; Choudhary, P.; Sharma, A. ZnO-Modified

- G-C₃N₄: A Potential Photocatalyst for Environmental Application. *ACS Omega* **2020**, *5*, 3828–3838, doi:10.1021/acsomega.9b02688.
33. Yue, B.; Li, Q.; Iwai, H.; Kako, T.; Ye, J. Hydrogen Production Using Zinc-Doped Carbon Nitride Catalyst Irradiated with Visible Light. *Sci. Technol. Adv. Mater.* **2011**, *12*, 034401, doi:10.1088/1468-6996/12/3/034401.
 34. Moussa, H.; Chouchene, B.; Gries, T.; Balan, L.; Mozet, K.; Medjahdi, G.; Schneider, R. Growth of ZnO Nanorods on Graphitic Carbon Nitride gCN Sheets for the Preparation of Photocatalysts with High Visible-Light Activity. *ChemCatChem* **2018**, *10*, 4973–4983, doi:10.1002/cctc.201801206.
 35. Zhu, Y.-P.; Li, M.; Liu, Y.-L.; Ren, T.-Z.; Yuan, Z.-Y. Carbon-Doped ZnO Hybridized Homogeneously with Graphitic Carbon Nitride Nanocomposites for Photocatalysis. *J. Phys. Chem. C* **2014**, *118*, 10963–10971, doi:10.1021/jp502677h.
 36. Kumaresan, N.; Sinthiya, M.M.A.; Sarathbavan, M.; Ramamurthi, K.; Sethuraman, K.; Babu, R.R. Synergetic Effect of G-C₃N₄/ZnO Binary Nanocomposites Heterojunction on Improving Charge Carrier Separation through 2D/1D Nanostructures for Effective Photocatalytic Activity under the Sunlight Irradiation. *Sep. Purif. Technol.* **2020**, *244*, 116356, doi:10.1016/j.seppur.2019.116356.
 37. Kim, N. Van; Nga, N.T.V.; Phuong, T.T.T.; Tuan, N. Le; Vien, V. Synthesis of G-C₃N₄/ZnO Composites with Enhanced Photocatalytic Activity under Visible Light. *Vietnam J. Chem.* **2018**, *56*, 220–225, doi:10.1002/vjch.201800017.
 38. Alharthi, F.A.; Alghamdi, A.A.; Alanazi, H.S.; Alsyahi, A.A.; Ahmad, N. Photocatalytic Degradation of the Light Sensitive Organic Dyes: Methylene Blue and Rose Bengal by Using Urea Derived g-C₃N₄/ZnO Nanocomposites. *Catalysts* **2020**, *10*, 1457,

- doi:10.3390/catal10121457.
39. Mathialagan, A.; Manavalan, M.; Venkatachalam, K.; Mohammad, F.; Oh, W.C.; Sagadevan, S. Fabrication and Physicochemical Characterization of g-C₃N₄/ZnO Composite with Enhanced Photocatalytic Activity under Visible Light. *Opt. Mater. (Amst)*. **2020**, *100*, 109643, doi:10.1016/j.optmat.2019.109643.
 40. Zhong, Q.; Lan, H.; Zhang, M.; Zhu, H.; Bu, M. Preparation of Heterostructure g-C₃N₄/ZnO Nanorods for High Photocatalytic Activity on Different Pollutants (MB, RhB, Cr(VI) and Eosin). *Ceram. Int.* **2020**, *46*, 12192–12199, doi:10.1016/j.ceramint.2020.01.265.
 41. Jingyu, H.; Ran, Y.; Zhaohui, L.; Yuanqiang, S.; Lingbo, Q.; Nti Kani, A.; Kani, A.N. In-Situ Growth of ZnO Globular on g-C₃N₄ to Fabrication Binary Heterojunctions and Their Photocatalytic Degradation Activity on Tetracyclines. *Solid State Sci.* **2019**, *92*, 60–67, doi:10.1016/j.solidstatesciences.2019.02.009.
 42. Zhang, Z.; Sun, Y.; Wang, Y.; Yang, Y.; Wang, P.; Shi, L.; Feng, L.; Fang, S.; Liu, Q.; Ma, L.; et al. Synthesis and Photocatalytic Activity of g-C₃N₄/ZnO Composite Microspheres under Visible Light Exposure. *Ceram. Int.* **2022**, *48*, 3293–3302, doi:10.1016/j.ceramint.2021.10.104.
 43. Yu, W.; Xu, D.; Peng, T. Enhanced Photocatalytic Activity of G-C₃N₄ for Selective CO₂ Reduction to CH₃OH via Facile Coupling of ZnO: A Direct Z-Scheme Mechanism. *J. Mater. Chem. A* **2015**, *3*, 19936–19947, doi:10.1039/C5TA05503B.
 44. Ma, R.; Zhang, S.; Li, L.; Gu, P.; Wen, T.; Khan, A.; Li, S.; Li, B.; Wang, S.; Wang, X. Enhanced Visible-Light-Induced Photoactivity of Type-II CeO₂/g-C₃N₄ Nanosheet toward Organic Pollutants Degradation. *ACS Sustain. Chem. Eng.* **2019**, *7*, 9699–9708, doi:10.1021/acssuschemeng.9b01477.

45. Li, G.; Wu, Y.; Zhang, M.; Chu, B.; Huang, W.; Fan, M.; Dong, L.; Li, B. Enhanced Removal of Toxic Cr(VI) in Wastewater by Synthetic $\text{TiO}_2/\text{g-C}_3\text{N}_4$ Microspheres/rGO Photocatalyst under Irradiation of Visible Light. *Ind. Eng. Chem. Res.* **2019**, *58*, 8979–8989, doi:10.1021/acs.iecr.8b05990.
46. Guan, R.; Li, J.; Zhang, J.; Zhao, Z.; Wang, D.; Zhai, H.; Sun, D. Photocatalytic Performance and Mechanistic Research of $\text{ZnO/g-C}_3\text{N}_4$ on Degradation of Methyl Orange. *ACS Omega* **2019**, *4*, 20742–20747, doi:10.1021/acsomega.9b03129.
47. Luo, S.; Li, S.; Zhang, S.; Cheng, Z.; Nguyen, T.T.; Guo, M. Visible-Light-Driven Z-Scheme Protonated $\text{G-C}_3\text{N}_4/\text{wood Flour biochar/BiVO}_4$ Photocatalyst with Biochar as Charge-Transfer Channel for Enhanced RhB Degradation and Cr(VI) Reduction. *Sci. Total Environ.* **2022**, *806*, 150662, doi:10.1016/j.scitotenv.2021.150662.
48. Paul, D.R.; Sharma, R.; Nehra, S.P.; Sharma, A. Effect of Calcination Temperature, pH and Catalyst Loading on Photodegradation Efficiency of Urea Derived Graphitic Carbon Nitride towards Methylene Blue Dye Solution. *RSC Adv.* **2019**, *9*, 15381–15391, doi:10.1039/c9ra02201e.
49. Muthukumaran, M.; Prasath, P.V.; Kulandaivelu, R.; Sagadevan, S.; Mohammad, F.; Oh, W.C. Fabrication of Nitrogen-Rich Graphitic Carbon nitride/ Cu_2O ($\text{G-C}_3\text{N}_4@\text{Cu}_2\text{O}$) Composite and Its Enhanced Photocatalytic Activity for Organic Pollutants Degradation. *J. Mater. Sci. Mater. Electron.* **2020**, *31*, 2257–2268, doi:10.1007/s10854-019-02757-0.
50. Rosli, S.A.; Alias, N.; Bashrom, N.; Ismail, S.; Tan, W.K.; Kawamura, G.; Matsuda, A.; Lockman, Z. Hexavalent Chromium Removal via Photoreduction by Sunlight on Titanium–dioxide Nanotubes Formed by Anodization with a Fluorinated Glycerol–water Electrolyte. *Catalysts* **2021**, *11*, 376, doi:10.3390/catal11030376.

51. Islam, J.B.; Furukawa, M.; Tateishi, I.; Kawakami, S.; Katsumata, H.; Kaneco, S. Enhanced Photocatalytic Reduction of Toxic Cr(VI) with Cu Modified ZnO Nanoparticles in Presence of EDTA under UV Illumination. *SN Appl. Sci.* **2019**, *1*, 1–11, doi:10.1007/s42452-019-1282-x.
52. Hsu, H.-T.; Chen, S.-S.; Tang, Y.-F.; Hsi, H.-C. Enhanced Photocatalytic Activity of chromium(VI) Reduction and EDTA Oxidization by Photoelectrocatalysis Combining Cationic Exchange Membrane Processes. *J. Hazard. Mater.* **2013**, *248-249*, 97–106, doi:10.1016/j.jhazmat.2012.12.058.
53. Li, H.; Wu, T.; Cai, B.; Ma, W.; Sun, Y.; Gan, S.; Han, D.; Niu, L. Efficiently Photocatalytic Reduction of Carcinogenic Contaminant Cr (VI) upon Robust AgCl: Ag Hollow Nanocrystals. *Appl. Catal. B Environ.* **2015**, *164*, 344–351, doi:10.1016/j.apcatb.2014.09.049.
54. Kumar, K.V.A.; Vinodkumar, T.; Selvaraj, M.; Suryakala, D.; Subrahmanyam CH Visible Light-Induced Catalytic Abatement of 4-Nitrophenol and Rhodamine B Using ZnO/g-C₃N₄ catalyst. *J. Chem. Sci.* **2021**, *133*, 41.
55. Saravanakumar, K.; Karthik, R.; Chen, S.-M.; Kumar, J.V.; Prakash, K.; Muthuraj, V. Construction of Novel Pd/CeO₂/g-C₃N₄ Nanocomposites as Efficient Visible-Light Photocatalysts for Hexavalent Chromium Detoxification. *J. Colloid Interface Sci.* **2017**, *504*, 514–526, doi:10.1016/j.jcis.2017.06.003.
56. Sun, J.; Hou, Y.; Yu, Z.; Tu, L.; Yan, Y.; Qin, S.; Chen, S.; Lan, D.; Zhu, H.; Wang, S. Visible-Light-Driven Z-Scheme Zn₃In₂S₆/AgBr Photocatalyst for Boosting Simultaneous Cr (VI) Reduction and Metronidazole Oxidation: Kinetics, Degradation Pathways and Mechanism. *J. Hazard. Mater.* **2021**, *419*, 126543, doi:10.1016/j.jhazmat.2021.126543.

-
57. Nanda, B.; Pradhan, A.C.; Parida, K.M. Fabrication of Mesoporous CuO/ZrO₂-MCM-41 Nanocomposites for Photocatalytic Reduction of Cr(VI). *Chem. Eng. J.* **2017**, *316*, 1122–1135, doi:10.1016/j.cej.2016.11.080.
58. Yin, H.; Fan, T.; Cao, Y.; Li, P.; Yao, X.; Liu, X. Construction of Three-Dimensional MgIn₂S₄ Nanoflowers/two-Dimensional Oxygen-Doped G-C₃N₄ Nanosheets Direct Z-Scheme Heterojunctions for Efficient Cr(VI) Reduction: Insight into the Role of Superoxide Radicals. *J. Hazard. Mater.* **2021**, *420*, 126567, doi:10.1016/j.jhazmat.2021.126567.
59. Hu, X.; Zhao, Y.; Wang, H.; Cai, X.; Hu, X.; Tang, C.; Liu, Y.; Yang, Y. Decontamination of Cr(VI) by Graphene oxide@TiO₂ in an Aerobic Atmosphere: Effects of pH, Ferric Ions, Inorganic Anions, and Formate. *J. Chem. Technol. Biotechnol.* **2018**, *93*, 2226–2233, doi:10.1002/jctb.5565.
60. Babu, P.; Mohanty, S.; Naik, B.; Parida, K. Serendipitous Assembly of Mixed Phase BiVO₄ on B-Doped G-C₃N₄: An Appropriate P-N Heterojunction for Photocatalytic O₂ Evolution and Cr(VI) Reduction. *Inorg. Chem.* **2019**, *58*, 12480–12491, doi:10.1021/acs.inorgchem.9b02309.
61. Yi, X.-H.; Wang, F.-X.; Du, X.-D.; Wang, P.; Wang, C.-C. Facile Fabrication of BUC-21/g-C₃N₄ Composites and Their Enhanced Photocatalytic Cr(VI) Reduction Performances under Simulated Sunlight. *Appl. Organomet. Chem.* **2019**, *33*, e4621, doi:10.1002/aoc.4621.
62. Katsumata, H.; Islam Molla, M.A.; Islam, J.B.; Tateishi, I.; Furukawa, M.; Kaneco, S. Dual Z-Scheme Heterojunction g-C₃N₄/Ag₃PO₄/AgBr Photocatalyst with Enhanced Visible-Light Photocatalytic Activity. *Ceram. Int.* **2022**, *48*, 21898–21905, doi:10.1016/j.ceramint.2022.04.176.

63. Liao, G.; Li, C.; Li, X.; Fang, B. Emerging Polymeric Carbon Nitride Z-Scheme Systems for Photocatalysis. *Cell Reports Phys. Sci.* 2021, 2, 100355.
64. Lu, X.; Quan, L.; Hou, H.; Qian, J.; Liu, Z.; Zhang, Q. Fabrication of 1D/2D Y-Doped CeO₂/ZnIn₂S₄ S-Scheme Photocatalyst for Enhanced Photocatalytic H₂ Evolution. *J. Alloys Compd.* **2022**, 925, 166552, doi:10.1016/j.jallcom.2022.166552.
65. Zhang, H.; Luo, Y.-H.; Chen, F.-Y.; Geng, W.-Y.; Lu, X.-X.; Zhang, D.-E. Enhancing the Spatial Separation of Photogenerated Charges on Fe-Based MOFs via Structural Regulation for Highly-Efficient Photocatalytic Cr(VI) Reduction. *J. Hazard. Mater.* **2022**, 441, 129875, doi:10.1016/j.jhazmat.2022.129875.

CHAPTER THREE

Facile Fabrication of Ag/g-C₃N₄ Photocatalyst with Visible Light Responsive Efficiency for Cr(VI) Reduction in Presence of EDTA

3.1 Introduction

An increased level of heavy metal contamination resulting from industrial activities is a serious environmental issue [1–4]. Hexavalent chromium (Cr(VI)) is a highly toxic heavy metal with a stern emission standard limit ($\leq 0.05 \text{ mg L}^{-1}$) [5]. Most Cr(VI) is emanated from numerous industries such as textiles, steel manufacturing, metals plating, dye, leather tanning, and other chemical industries [6–9]. Cr(VI) is harmful to living organisms because of its extreme toxicity and leads to various diseases, including lung cancer, skin irritation, chromate ulcers, pulmonary congestion, vomiting, and perforated nasal septa [10,11]. In contrast to Cr(VI), Cr(III) has 500–1000 times less toxicity and mobility as micronutrients for the human being [12–14]. Therefore, it is highly advantageous to convert Cr(VI) to Cr(III) from wastewater as Cr(III) is both environmentally benign and necessary for plant and human life. [15,16]. Currently, researchers are becoming more interested in using semiconductor-based photocatalytic technology to remove Cr(VI). It is regarded as a promising approach to reducing Cr(VI) to Cr(III) because of its acceptable cost, high efficiency, simple process, and high repeatability [17]. Researchers are also looking for visible light-responsive photocatalysts that can efficiently and cost-effectively remove Cr(VI). Graphitic carbon nitride (g-C₃N₄) is a polymeric semiconductor that has a characteristic graphite-like layered structure, sp² hybridization, and band gap of 2.7 eV. It is also a potential photocatalyst with chemical and thermal stability as well as visible light emission (460 nm) [18,19]. However, the performance of bare g-C₃N₄ is restrained by the quick e⁻-h⁺ pair recombination at a photoexcited g-C₃N₄ and its small specific surface area [20–22]. To circumvent this problem, several approaches, such as surface modification, metal and nonmetal doping, molecular doping, and the formation of heterojunction with other semiconductors have been applied to enhance the visible light-induced photocatalytic efficiency of g-C₃N₄ [23–35]. Doping with nonmetal and metal elements on the g-C₃N₄ surface has recently received increasing attention in the photocatalytic

reduction of Cr(VI) under visible light irradiation. For instance, Wu et al. (2019) fabricated g-C₃N₄ with Pd nanocones by the one-pot hydrothermal method, which showed boosting photocatalytic performance for Cr(VI) reduction induced by visible light irradiation. Wang et al. (2020) prepared Br-doped g-C₃N₄ and showed that it had higher photocatalytic performance in the reduction of Cr(VI). Patnaik et al. (2020) effectively decorated Au-Pd alloyed nanoparticles on mesoporous silica-modified g-C₃N₄ by the simple one-pot calcination approach and observed appreciable photocatalytic performance in Cr(VI) reduction.

In this aspect, to enhance the photocatalytic efficacy of g-C₃N₄, it could be fabricated with the noble metal Ag. This is because Ag has a surface plasmon resonance (SPR) effect and the band structure of silver matches that of g-C₃N₄ [39,40]. When g-C₃N₄ is fabricated with Ag, a pair of electrons of N might easily migrate to the Ag outermost shell to form a rigid N–Ag bond, which would effectively separate the photogenerated e⁻–h⁺ [40]. Several studies on the Ag/g-C₃N₄ composite have been reported, most of which focus on the photodegradation of organic pollutants, disinfection microorganisms, and H₂ production. Min et al. (2016) synthesized Ag/g-C₃N₄ composite by coupling the coordination-driven assembly of precursors and the calcination method for photodegradation of rhodamine B (RhB). Muñoz-Batista et al. (2016) reported the preparation of Ag/g-C₃N₄ composite for biocidal activity against *Escherichia coli* under UV and visible light irradiation. Zhang et al. (2016) constructed Ag-modified g-C₃N₄ composites with improved visible-light photocatalytic efficiency for the degradation of diclofenac and found excellent stability. Ren et al. (2021) prepared Ag/g-C₃N₄ composite by polymerization and the silver mirror reaction process for enhanced photocatalytic H₂ production. Although Islam et al. (2023) reported on the photocatalytic reduction of Cr(VI) using Ag-modified g-C₃N₄ under UV illumination, visible light-driven photocatalytic Cr(VI) reduction by Ag/g-C₃N₄ composites has been rarely reported.

Apart from this fabrication process, the addition of sacrificial electron donors (formic acid, EDTA, oxalic acid, and citric acid) can also be considered to improve the photocatalytic Cr(VI) reduction. EDTA showed a significant effect on improving the photocatalytic Cr(VI) reduction compared with other sacrificial electron donors, EDTA showed a significant impact on enhancing the photocatalytic Cr(VI) reduction. Further, EDTA can have an impact on particle size and morphologies due to the chelating effect of EDTA and metal ions in solution [16,46].

The majority of the Ag/g-C₃N₄ photocatalysts were prepared using thermal exfoliation and photo-reduction techniques, and the experimentation procedure was rather challenging. In this study, an easy approach to producing Ag/g-C₃N₄ photocatalyst is suggested.

In this work, Ag/g-C₃N₄ was synthesized from AgNO₃ and urea in one step through calcination and studied the reduction performance of Cr(VI) in the presence of EDTA under visible light irradiation. The synthesized catalyst was characterized by several techniques, like thermogravimetric analysis (TGA), X-ray diffraction (XRD), fourier transform infrared (FTIR), X-ray photoelectron spectroscopy (XPS), Brunauer-Emmett-Teller (BET) surface area, scanning electron microscopy (SEM), transmission electron microscopy (TEM), energy-dispersive X-ray spectroscopy (EDS), UV-visible diffuse reflection spectroscopy (DRS), photoluminescence (PL) spectroscopy and electrochemical impedance spectroscopy (EIS). A probable photocatalytic Cr(VI) reduction mechanism was also proposed and discussed. To the best of our knowledge, visible light induced photocatalytic Cr(VI) reduction from aqueous solution using simply synthesized Ag/g-C₃N₄ in presence of the EDTA has not been reported.

3.2 Materials and Methods

3.2.1 Chemicals and Materials

Urea, Cr(VI) standard solution (1000 ppm) as K₂Cr₂O₇, silver nitrate, sulphuric acid, and 1,5-diphenylcarbazide were bought from FUJIFILM Wako Pure Chemical Crop., Osaka,

Japan. Disodium ethylenediamine tetraacetic acid (EDTA-2Na) and acetone (C_3H_6O) were obtained from Kishida Chemical Co.Ltd., Osaka, Japan. The solution of 1,5-diphenylcarbazide (10 g L^{-1}) was produced by mixing 0.5 g of 1,5-diphenylcarbazide with 50 mL of acetone and preserved in a brown bottle.

3.2.2 Synthesis of Ag/g- C_3N_4

Ag/g- C_3N_4 can be prepared through calcination method. Briefly, firstly 3.15 g of $AgNO_3$ was dissolved in 20 mL H_2O to prepare Ag solution. Ten gram of urea was poured into a porcelain crucible, and 0.75 mL of the prepared Ag solution and 1.75 mL of H_2O were added to form slurry. The crucible was then covered, placed in an electric furnace, and heated at $500\text{ }^\circ\text{C}$ for 5 hours with a heating rate of $2\text{ }^\circ\text{C min}^{-1}$. The pale-yellow Ag/g- C_3N_4 was collected at room temperature and ground into fine powder. Bare g- C_3N_4 was prepared from the calcination of only urea as per the above mentioned method.

3.2.3 Characterization

TG analysis of the prepared Ag/g- C_3N_4 composite was carried out on the SII EXSTAR 6000 thermal analysis system (TG/DTA 6200, Japan) to assess the percentage of Ag content, where the temperature range was 25 to $950\text{ }^\circ\text{C}$ and the heating rate was $10\text{ }^\circ\text{C min}^{-1}$ in the air. To study crystal structure, XRD was taken by the Rigaku RINT Ultima-IV diffractometer (Japan) using $Cu\text{ K}\alpha$ radiation (2θ range, $10\text{--}80^\circ$) with a scan rate of $0.04^\circ/\text{s}$. FTIR measurements were performed to analyze the functional groups by a SPECTRUM 100 FTIR spectrometer (Perkin Elmer, Japan) with an ATR (Attenuated Total Reflection) assembly. A PHI Quantera SXM photoelectron spectrometer (Japan) with $Al\text{ K}\alpha$ radiation was used for XPS analysis. The N_2 adsorption-desorption isotherms were recorded by the BELSORP-miniII apparatus (MicrotracBEL, Japan) to evaluate Brunauer-Emmett-Teller (BET) surface area. The morphological characteristics of the photocatalyst were investigated through SEM and EDS

analysis by a JEOL JEM-1400 Flash SEM. The TEM was also analyzed by a JEOL JEM-1011 TEMA. A JASCO V-750 UV–visible instrument (Japan) equipped with an integrating sphere attachment was used for the UV–visible DRS study, where BaSO_4 was used as a reference. The PL spectra were tested on a Shimadzu RF-5300PC system (Japan) with an excitation wavelength of 340 nm. The EIS measurement was assayed by an electrochemical Versa STAT 3 workstation (Princeton Applied Research, Japan) equipped with a conventional three-electrode system, where a FTO glass plate was used as an electrode, which was coated by a uniform photocatalyst slurry with nafion solution. And as an electrolyte, Na_2SO_4 (0.5 mol L^{-1}) was used. Ag/AgCl (saturated KCl) and Pt wire were utilized to produce the electrodes to be applied as the reference and counter electrodes, respectively.

3.2.4 Photocatalytic Reduction

A 50 mL of pyrex vessel reactor was used for the photocatalytic Cr(VI) reduction process. Typically, 40 mg of Ag/g- C_3N_4 and EDTA-2Na (400 ppm) as a photocatalyst and a hole scavenger, respectively, are added to 30 mL of a 20 ppm Cr solution in a pyrex vessel. To ensure adsorption-desorption equilibrium, the suspension was constantly stirred in the dark for about 30 minutes before visible light irradiation. Then 1.5 mL of the suspension was taken for analysis. After that, a UV cutoff filter ($<400 \text{ nm}$) equipped LED light was used as a light source to irradiate the suspension and collect 1.5 mL of it every 10 minutes for analysis. To get clear solution, the collected suspension was centrifuged for 4 minutes. The Nesslerization technique was applied to assess the photocatalytic reduction of Cr(VI). The sample ($300 \mu\text{L}$), 10 g L^{-1} 1,5-diphenyl carbazide ($200 \mu\text{L}$), and 2 mol L^{-1} H_2SO_4 ($500 \mu\text{L}$) were put into a volumetric flask (20 mL). The mixture was then diluted with distilled water and left for 10 minutes. The absorbance was measured at 540 nm by a UV-visible spectrophotometer (AS ONE Corp., ASV11D). Finally, using Eq. 3.1, the reduction efficacy (%) of Cr(VI) was calculated.

$$\text{Reduction efficacy}(\%) = \frac{C_0 - C}{C_0} \times 100\% \quad (3.1)$$

where C_0 and C represent the concentration of Cr(VI) at time 0 and t , respectively.

3.3 Results and Discussion

3.3.1 TG Analysis

To inspect the thermal stability and amount of Ag in the as-synthesized Ag/g-C₃N₄ composite, TG analysis was carried out from room temperature to 900 °C (heating rate 10 °C min⁻¹). As presented in Figure 3.1a, two weight loss phases appear in the TG analysis. The first weight loss phase occurred below 200 °C and was likely caused by absorbed water volatilizing on the Ag/g-C₃N₄ composite surface. The major weight loss phase was found in the temperature range of 500 to 680 °C at which g-C₃N₄ was decomposed, because Ag is thermally very stable at high temperatures [47]. As per the TG analysis, an overall 22% of Ag was acquired in the composite.

3.3.2 XRD Analysis

In order to reveal the crystal phase and crystallinity of a sample, an XRD pattern is used. Figure 3.1b displays the XRD pattern for g-C₃N₄ and Ag/g-C₃N₄ composite and Figure 3.1c shows the standard cards JCPDS as references. The XRD pattern of g-C₃N₄ gives two obvious peaks at around 27.6° and 13.2°. The strong peak appeared around 27.6° due to interplanar stacking (002) of the conjugated aromatic system with an interlayer distance of $d = 0.323$ nm. Also, a weak peak was observed at about 13.2° for interlayer stacking (100) of the in-plane structural packing motif of tri-s-triazine units with an interplanar distance of $d = 0.670$ nm [48,49]. The acquired XRD pattern reveals the crystalline phase of g-C₃N₄ and the absence of any impurities or secondary phases (JCPDS no. 87-1526) [50]. Furthermore, Ag/g-C₃N₄ exhibited diffraction peaks around 38.2°, 44.4°, 64.6°, and 77.8°, which related to the (111), (200), (220), and (311) crystal planes of elemental Ag (JCPDS no. #65-2871)[43]. Moreover,

the occurrence of the (002) plane at 27.9° demonstrates the presence of graphitic structure, which is attributed to the interlayer distance of $d = 0.320$ nm. The decrement in interlayer distance of $g\text{-C}_3\text{N}_4$ in $\text{Ag}/g\text{-C}_3\text{N}_4$ increases the interaction between the layers [49,51]. In addition, sharp and intense Ag peaks cover the broader and disappear less intense peak of 13.2° , indicating significantly decreased the size of the layer [43,48]. The crystal structure of the (100) and (002) planes in $g\text{-C}_3\text{N}_4$ and the (002) plan in $\text{Ag}/g\text{-C}_3\text{N}_4$ is presented in Figure 3.2.

3.3.3 FTIR Analysis

To evaluate the chemical nature of $g\text{-C}_3\text{N}_4$ and $\text{Ag}/g\text{-C}_3\text{N}_4$ composite, FTIR analysis was used (Figure 3.1d). For the $g\text{-C}_3\text{N}_4$ spectrum, a broad peak in the region of $3000\text{--}3350\text{ cm}^{-1}$ was assigned to the N–H and O–H stretching vibrations. This suggests that absorbed water molecules and uncondensed amino groups are present in $g\text{-C}_3\text{N}_4$. A series of characteristic absorption peaks appeared in the region from 1200 to 1650 cm^{-1} due to heterocyclic C–N and aromatic C=N stretching vibrations. And also, an intense band at 801 cm^{-1} is corresponds to the tri-s-triazine breathing mode in the $g\text{-C}_3\text{N}_4$ [52,53]. The FTIR spectra of $\text{Ag}/g\text{-C}_3\text{N}_4$ composite showed the characteristic absorption peaks of $g\text{-C}_3\text{N}_4$, signifying that Ag fabrication may not have influenced the structure of $g\text{-C}_3\text{N}_4$. Thus, it can be assumed from XRD and FTIR studies that Ag content impacts crystal structure but not the chemical nature of $g\text{-C}_3\text{N}_4$.

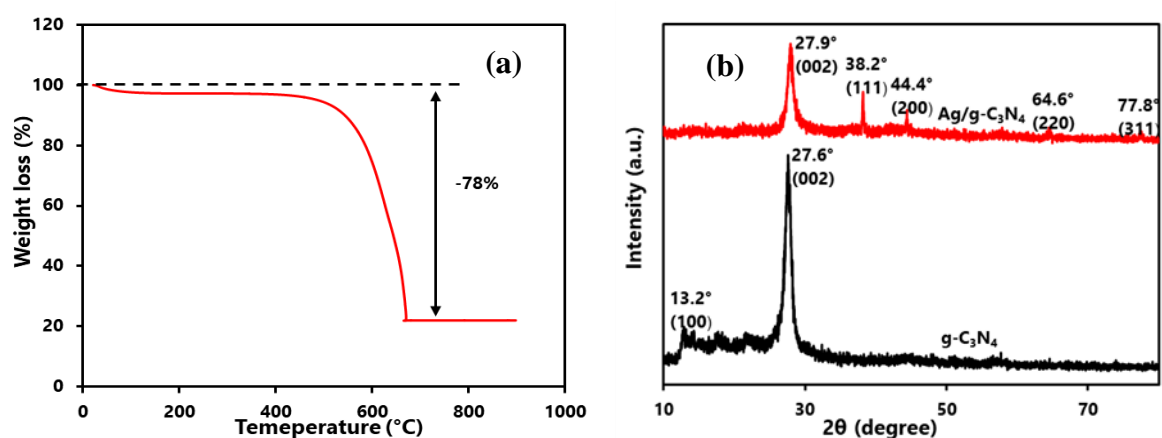


Figure 3.1 (a) TG analysis curve for $\text{Ag}/g\text{-C}_3\text{N}_4$ composite and (b) XRD patterns of $g\text{-C}_3\text{N}_4$, and $\text{Ag}/g\text{-C}_3\text{N}_4$

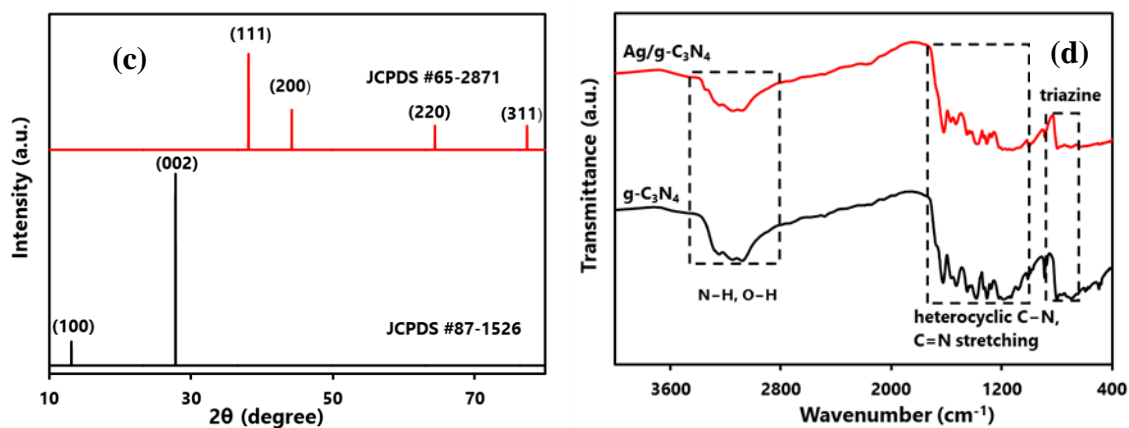


Figure 3.1 (c) Standard XRD cards of JCPDS 87-1526 and 65-2871, and (d) FTIR spectra of g-C₃N₄, and Ag/g-C₃N₄.

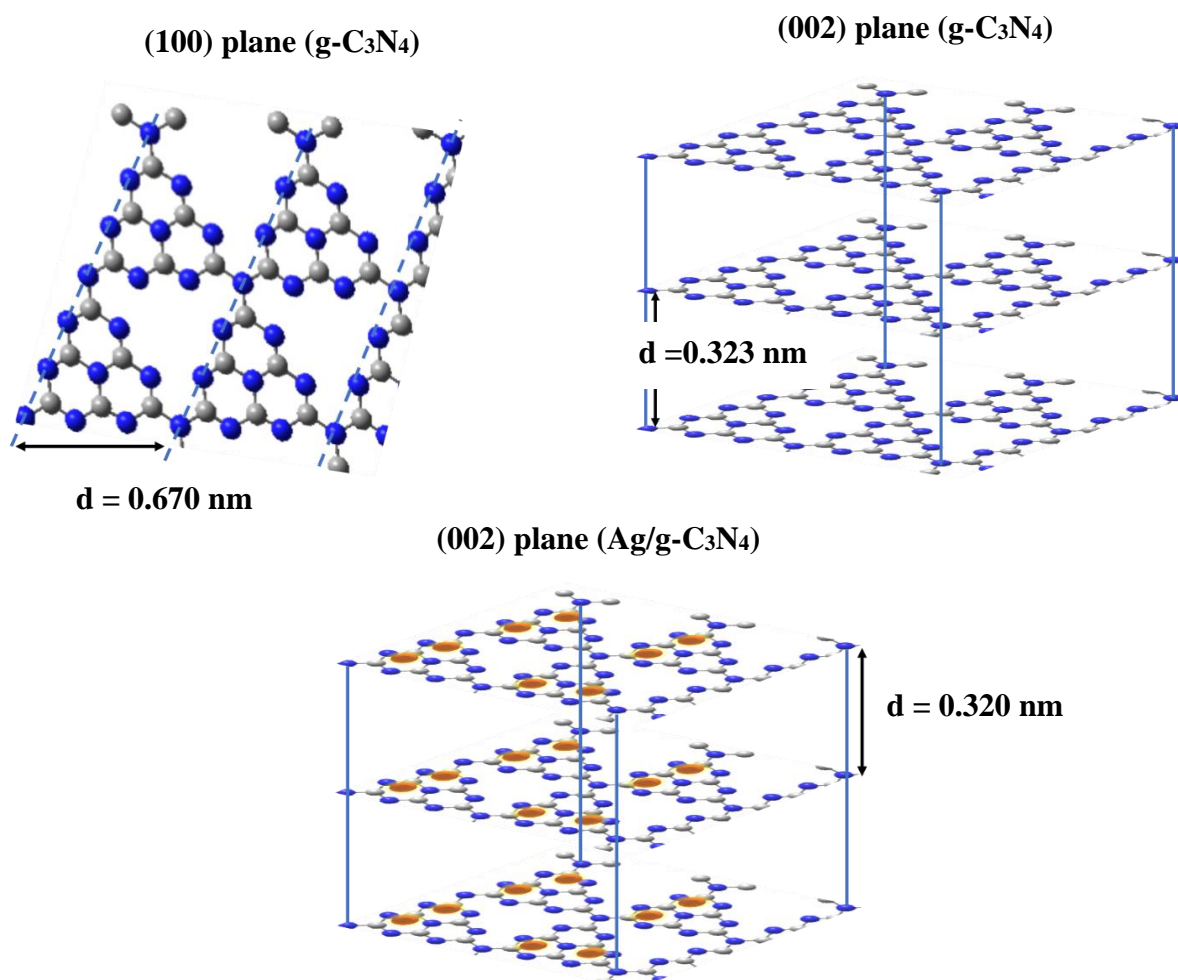


Figure 3.2 The crystal structure of the 100 and 002 planes in g-C₃N₄ and the (002) plane in Ag/g-C₃N₄.

3.3.4 XPS Analysis

XPS analysis was further performed to confirm the chemical state and composition of the as-synthesized Ag/g-C₃N₄ photocatalyst (Figure 3.3). The survey XPS spectra of g-C₃N₄ and Ag/g-C₃N₄ are depicted in Figure 3.3a. The survey XPS spectra of g-C₃N₄ showed the presence of C, N, and O, while those of Ag/g-C₃N₄ exhibited all of the peaks that corresponded to the elements Ag, C, N, and trace amounts of O. The high-resolution C1s spectrum of Ag/g-C₃N₄ displays four distinct peaks centered at 284.8 eV, 286.4 eV, 287.9 eV, and 288.8 eV (Figure 3.3b). These peaks are attributed to sp²C=C, sp³C-N, C=O, and N=C-N species, respectively [54,55]. Figure 3.3c illustrates the high-resolution spectrum N 1s of composite fitted into three peaks representing sp²-bonded N in triazine rings (C-N=C at 398.5 eV), bridging N atoms (N-(C)₃ at 400.2 eV), and π excitation (charging effect) cause of weak peak at 404.2 eV, respectively [44,56]. Figures 3.3b, c also demonstrate that the high resolution spectra C 1s and N 1s of g-C₃N₄ and Ag/g-C₃N₄ are nearly identical, supporting the composite's purity. The high-resolution O 1s XPS spectra of both Ag/g-C₃N₄ and g-C₃N₄ exhibited only one peak with small intensity, which is attributed to the -OH groups in the adsorbed H₂O or -OH groups on the g-C₃N₄ surface (Figure 3.3d). In addition, the Ag 3d spectra (Figure 3.3e) presented two peaks for metallic Ag⁰ species at 367.9 and 373.9 eV aroused from Ag 3d_{5/2} and Ag 3d_{3/2} binding energies, respectively. The splitting binding energy of these distinctive Ag 3d peaks is 6.0 eV, which indicates the presence of metallic Ag⁰ species. These findings also imply that metallic Ag⁰ was well-doped on the g-C₃N₄ surface [57,58].

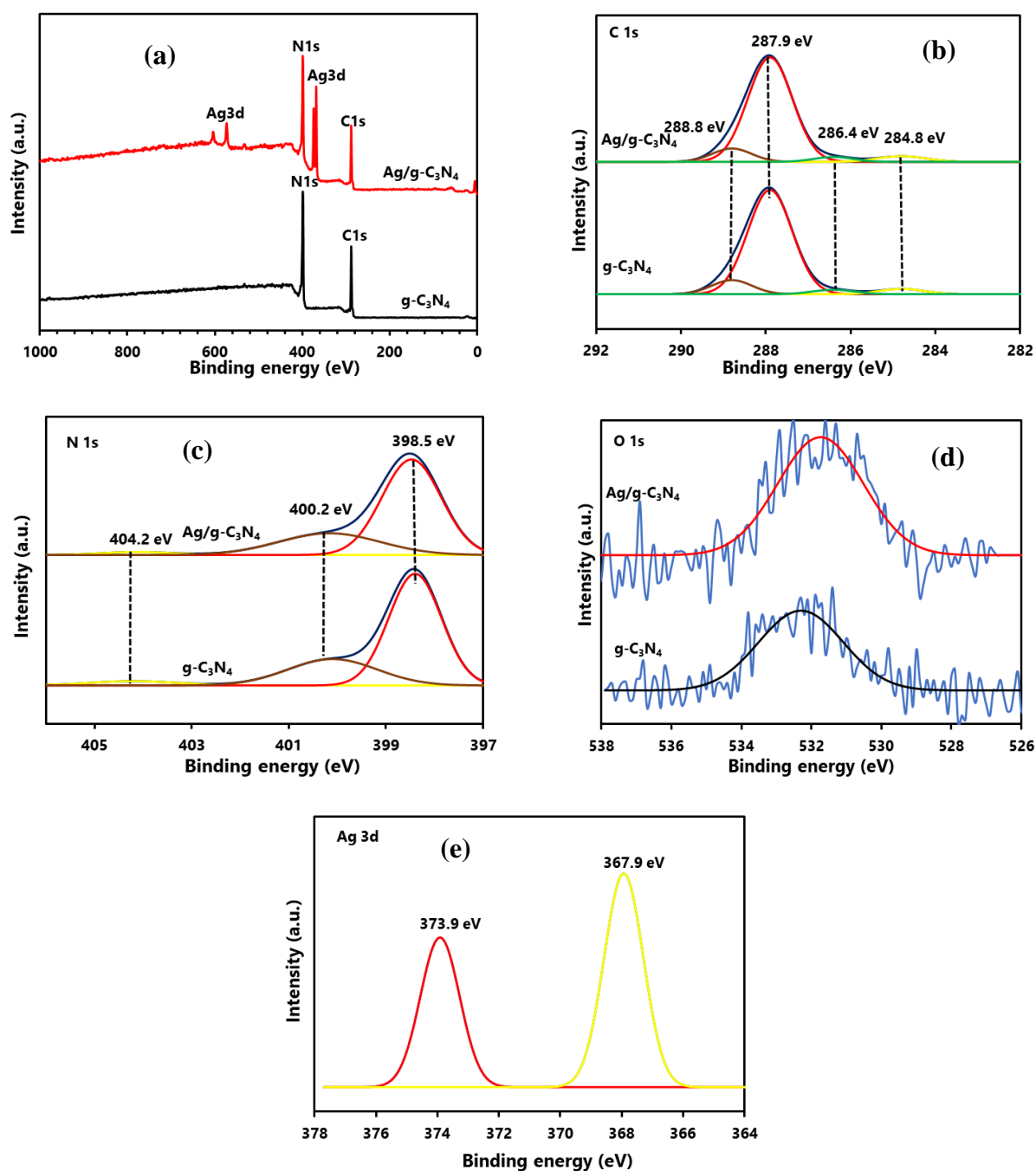


Figure 3.3 (a) survey XPS spectra of Ag/g-C₃N₄ composite and g-C₃N₄; overlapping high resolution (b) C 1s, (c) N 1s, and (d) O 1s XPS spectra of Ag/g-C₃N₄ and g-C₃N₄ and (e) high resolution Ag 3d XPS spectra of Ag/g-C₃N₄ composite.

3.3.5 BET Surface Area and Pore Size Distribution Analysis

The BET surface area of the catalyst also impacts its photocatalytic performance as well. Nitrogen adsorption-desorption isotherms by the Brunauer-Emmett-Teller (BET) method

were used for the analysis of surface area, total pore volume, and average pore size. From Figure 3.4, it was appeared that both $g\text{-C}_3\text{N}_4$ and $\text{Ag/g-C}_3\text{N}_4$ have type IV isotherms with H3 hysteresis loops. This appearance revealed that $\text{Ag/g-C}_3\text{N}_4$ possesses a mesoporous structure, just like $g\text{-C}_3\text{N}_4$ [44,59]. Table 3.1 presents the corresponding data, such as surface area, pore size, and pore volume of $g\text{-C}_3\text{N}_4$ and $\text{Ag/g-C}_3\text{N}_4$. The BET surface area of $\text{Ag/g-C}_3\text{N}_4$ was smaller than that of $g\text{-C}_3\text{N}_4$. This may be attributed to the decrease of the small pore, which is confirmed by the pore size distribution, as mentioned in the literature [60,61]. According to the result, the improved photocatalytic efficiency is not a consequence of the composite BET surface area.

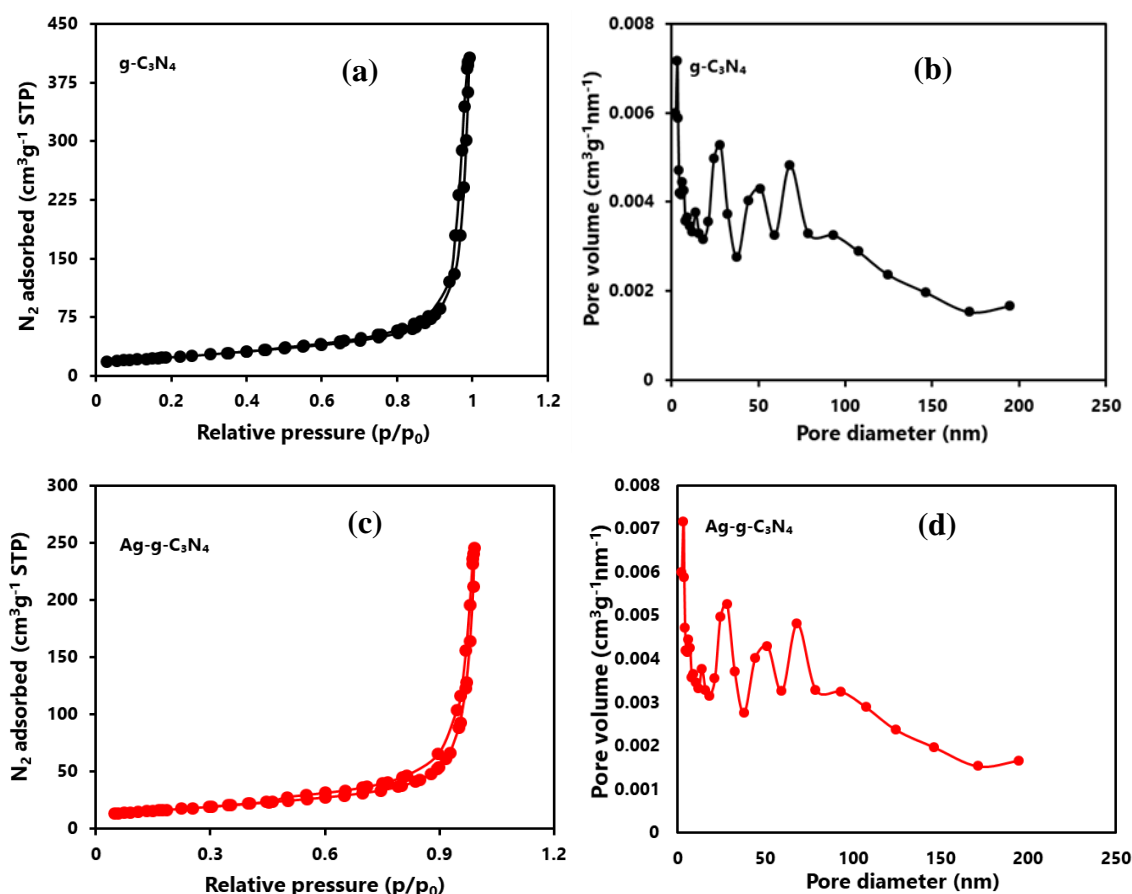


Figure 3.4 N_2 adsorption-desorption isotherms (a,c) and pore size distribution curves (b,d) of $g\text{-C}_3\text{N}_4$ and $\text{Ag/g-C}_3\text{N}_4$ composite.

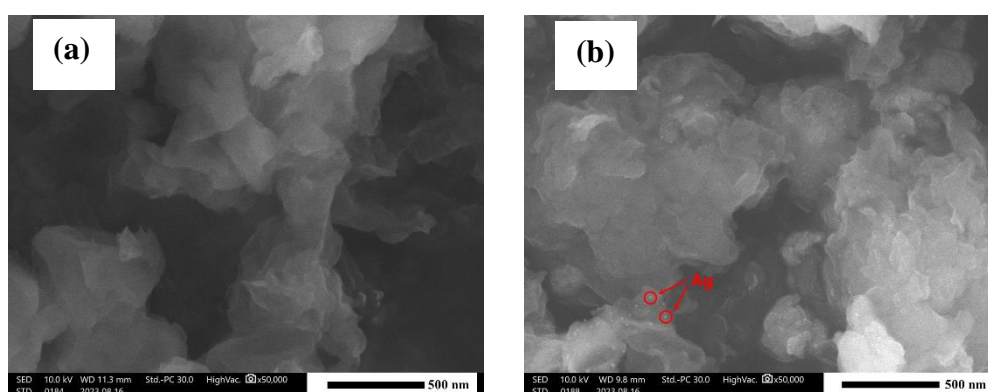
Table 3.1 Surface area, pore volume, and pore diameter of the g-C₃N₄ and Ag-g-C₃N₄ composite

Photocatalyst	BET surface area (m ² /g)	Total pore volume (cm ³ /g)	Average pore diameter (nm)
g-C ₃ N ₄	83.10	0.58	28.55
Ag-g-C ₃ N ₄	59.55	0.35	24.34

3.3.6 Morphological Analysis

The morphological features of the synthesized Ag/g-C₃N₄ catalyst were explored by SEM, TEM, and EDS analysis. The SEM image (Figure 3.5a) of g-C₃N₄ clearly possesses a lamellar stacking structure, which corresponds to the literature report [26]. After introducing Ag, the Ag/g-C₃N₄ composite (Figure 3.5b) also shows lamellar structure, where Ag particles were observed to be uniformly deposited on the surface of g-C₃N₄, which strongly impacts the photocatalytic efficacy of Ag/g-C₃N₄ and may have advantages in the reduction of Cr(VI).

Figures 3.5c, d represent the TEM images of synthesized g-C₃N₄ and Ag/g-C₃N₄. As represented in Figure 3.5c, g-C₃N₄ exhibited a flat layered structure similar to that seen in SEM images. However, the presence of Ag particles on the surface of the g-C₃N₄ was not clearly visualized in the TEM image of the Ag/g-C₃N₄ composite (Figure 3.5d).

**Figure 3.5** SEM images of (a) g-C₃N₄ and (b) Ag/g-C₃N₄

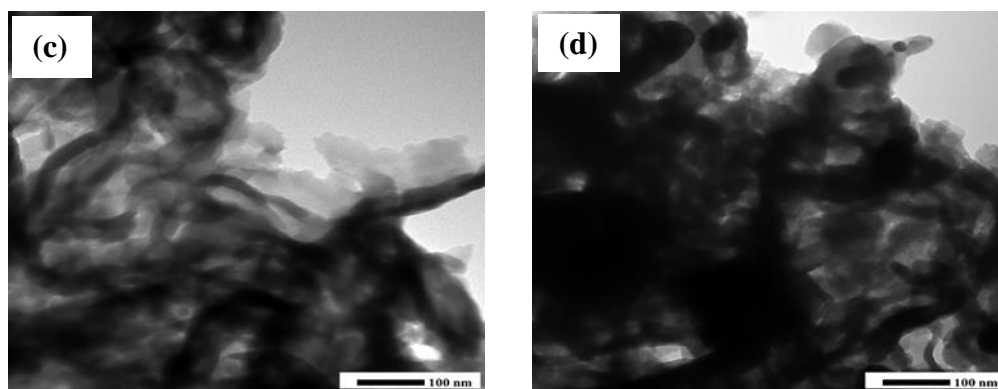


Figure 3.5 TEM images of (c) g-C₃N₄ and (d) Ag/g-C₃N₄.

The synthesized composite was further evaluated using EDS analysis to explore the elemental composition (Figure 3.6). According to EDS mapping, C, N, O, and Ag are present in the Ag/g-C₃N₄ composite and distributed uniformly. This finding suggests that the Ag/g-C₃N₄ composite was composed of Ag and g-C₃N₄ [60,62].

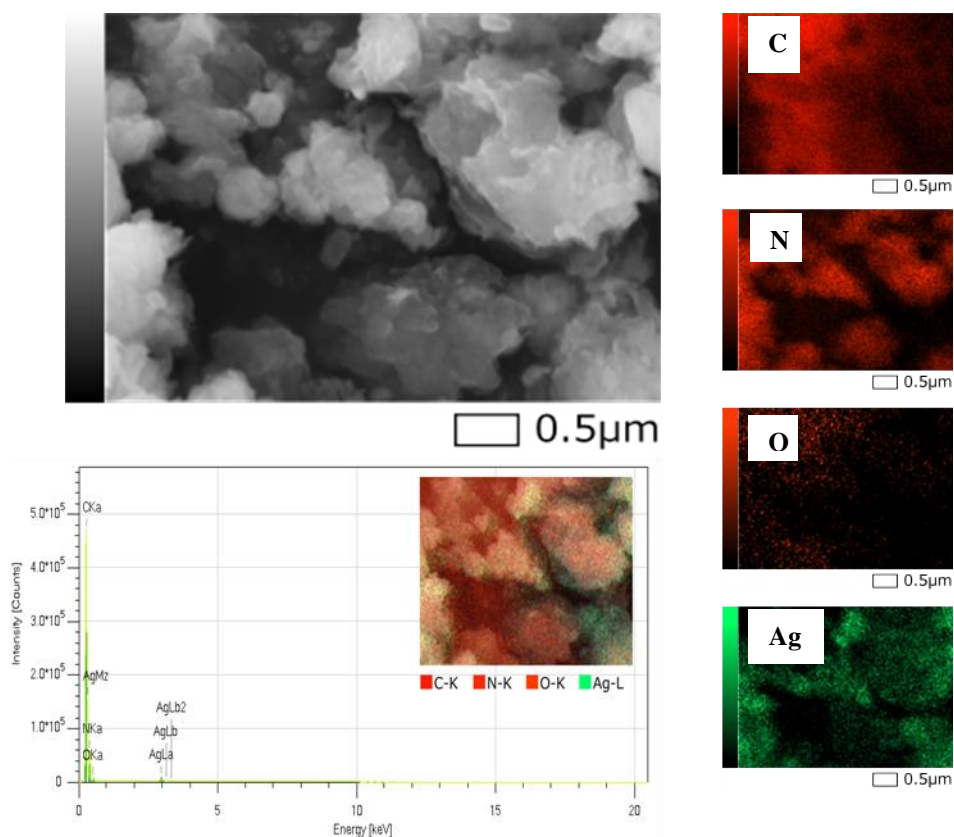


Figure 3.6 EDS mapping of Ag/g-C₃N₄ with SEM and EDX spectra.

3.3.7 Optical Properties Analysis

The optical properties of catalysts influence their photocatalytic activity. Figure 3.7a shows the optical properties of g-C₃N₄ and Ag/g-C₃N₄ composite, which were analyzed via the UV-visible DRS and expressed in terms of Kubelka-Munk absorption units. The indirect optical band gap of g-C₃N₄ and Ag/g-C₃N₄ was estimated by using the Tauc equation (Eq. 3.2) of indirect transition [63].

$$\alpha h\nu = A(h\nu - E_g)^2 \quad (3.2)$$

where α is the absorption coefficient, $h\nu$ is the photoenergy, A is a constant, and E_g is the optical band gap. Therefore, by plotting the value of $(\alpha h\nu)^{1/2}$ versus $h\nu$, the optical band gaps of g-C₃N₄ and Ag/g-C₃N₄ were estimated. It was observed that the absorption edge of g-C₃N₄ is about 430 nm with a band gap energy of 2.93 eV (Figure 3.7b). In contrast, the Ag/g-C₃N₄ composite (band gap energy 2.69 eV) exhibited significant red-shift due to the absorption of light, demonstrating its photocatalytic effectiveness in the visible region [64]. This characteristic could be due to the localized SPR effect of Ag content, which exhibited an effective plasmon resonance in the visible region. Additionally, the SPR effect of Ag particles enhances the local electromagnetic field (LEF), which accelerates the generation rate of photogenerated charge carriers (e^- - h^+ pair) on the g-C₃N₄ surface [65,66]. Furthermore, the decrement of the band gap as well as the enhancement of the visible light absorption ability of the Ag/g-C₃N₄ composite are attributed to a charge-transfer conversion between the g-C₃N₄ and Ag [62].

3.3.8 PL Analysis

PL analysis of the photocatalyst was performed with an excitation wavelength of 340 nm to clarify the charge separation behavior (Figure 3.7c). Generally, PL spectra describe the photoformed e^- - h^+ pair recombination process by the intensity of the peak. The slower

photogenerated e^-h^+ pair recombination is indicated by the small intensity peak [67]. Figure 3.7c shows a highly intense peak of g-C₃N₄, suggesting fast photogenerated electron and hole recombination. On the other hand, the presence of Ag in Ag/g-C₃N₄ composites decreases the PL peak intensity, providing evidence of direct influence on the e^-h^+ pair recombination because of the well-known capability of silver to act as an electron pool [42,68]. As a result, hole number and availability will increase on the g-C₃N₄ surface, and it might improve photocatalytic performance.

3.3.9 EIS Analysis

To learn more about the processes involved in the migration and transfer of photogenerated electrons, EIS measurements were carried out. The Nyquist plot's semicircle radius can be used to determine the interface resistance on an electrode's surface. The charge transfer efficiency is higher at a lower semicircle radius [69]. Figure 3.7d shows that the Nyquist plot of g-C₃N₄ has a larger semicircle radius, whereas Ag/g-C₃N₄ has a smaller semicircle radius. Moreover, the Nyquist plots of g-C₃N₄ and Ag/g-C₃N₄ were fitted to an equivalent circuit as shown in the inset of Figure 3.7d, where R_s is the series resistance, R_{ct} is the resistance due to the charge transfer process through the interfacial region of semiconductor and electrolyte solution, and C is the capacitance [59,70,71]. The R_{ct} values of g-C₃N₄ and Ag/g-C₃N₄ were estimated to be about 4.4×10^5 and $6.5 \times 10^4 \Omega$, respectively [31]. The lower charge transfer resistance and smaller semicircle radius indicate that g-C₃N₄ fabricated with Ag may effectively improve charge transfer capacitance because of the SPR effect between Ag and g-C₃N₄ [39,62]. Therefore, lessen the recombination of the e^-h^+ pair of photogenerated electrons and promote the progress of photocatalytic reactions.]

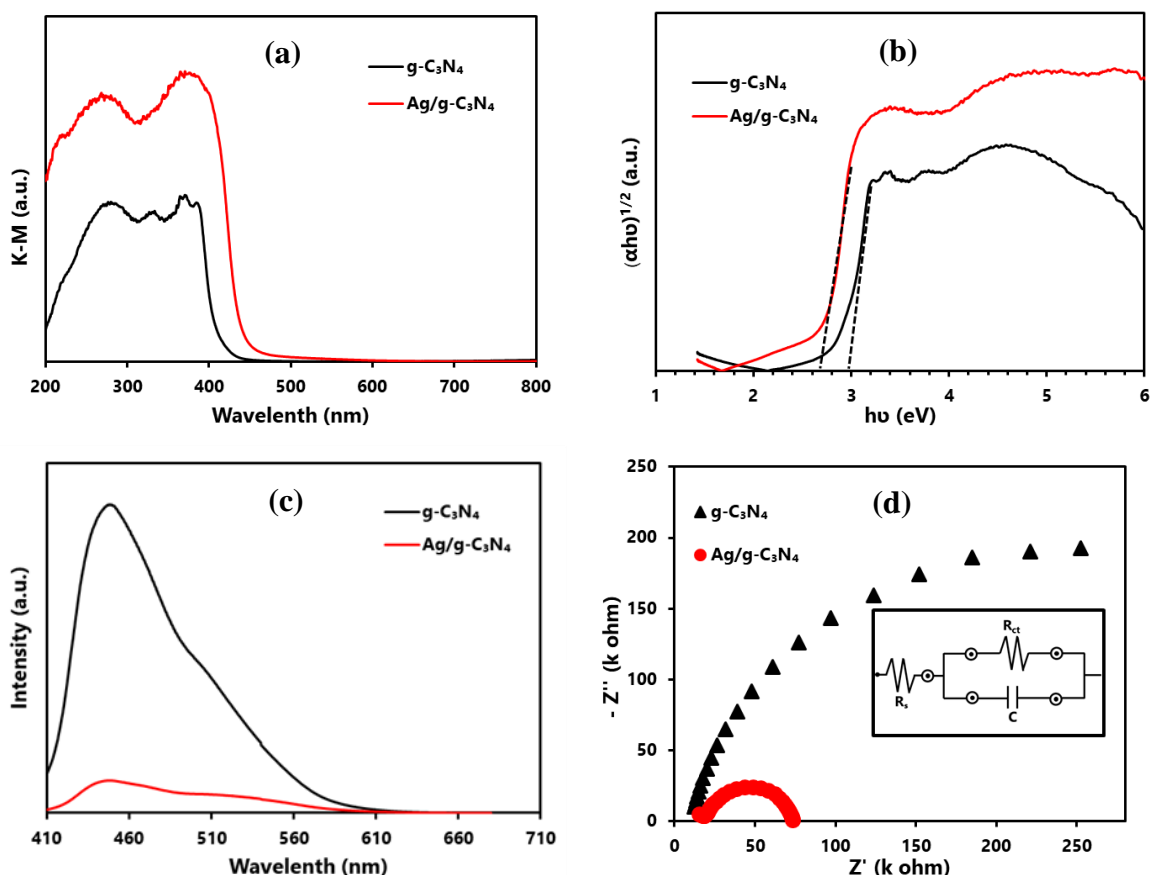


Figure 3.7 (a) UV-visible DRS, (b) Tauc plot, (c) Photoluminescence spectra and (d) Nyquist plots of $g\text{-C}_3\text{N}_4$, and $\text{Ag/g-C}_3\text{N}_4$ (inset figure: equivalent circuit diagram).

3.3.10 Mott-Schottky plots, Valance Band (VB) XPS Analysis and Band Diagram

The flat-band potential (E_{FB}) along with the conduction band potential (E_{CB}) of $g\text{-C}_3\text{N}_4$ and $\text{Ag/g-C}_3\text{N}_4$ composite were determined by constructing Mott-Schottky plots (Figures 3.8a, b). The positive slopes of the plots signify that $g\text{-C}_3\text{N}_4$ and $\text{Ag/g-C}_3\text{N}_4$ have properties of n-type semiconductors. From the abscissa axis and the intercept within the tangent lines of the plot, E_{FB} values were determined. The E_{FB} values of $g\text{-C}_3\text{N}_4$ and $\text{Ag/g-C}_3\text{N}_4$ are estimated to be -0.88 and -0.69 V (vs. Ag/AgCl at pH 7), respectively. The E_{FB} of $g\text{-C}_3\text{N}_4$ and $\text{Ag/g-C}_3\text{N}_4$ are calculated to be -0.27 and -0.08 V (vs. NHE at pH 0), respectively, based on the following Eq. 3.3 [72].

$$E (\text{NHE at pH 0}) = E (\text{Ag/AgCl at pH 7}) + 0.196 + 0.059 \times 7 \quad (3.3)$$

Typically, the E_{FB} exists below 0.1 eV compared to the E_{CB} of the photocatalyst containing the g-C₃N₄ framework. Hence, the E_{CB} values of g-C₃N₄ and Ag/g-C₃N₄ were estimated at -0.37 and -0.18 V (vs. NHE at pH 0), respectively. Then the valence band potential (E_{VB}) of the photocatalyst can be calculated using the Eq. 3.4 as follows:

$$E_g = E_{VB} - E_{CB} \quad (3.4)$$

where E_g is the band gap energy. According to the Tauc plot (Figure 3.7b), the band gaps (E_g) of g-C₃N₄ and Ag/g-C₃N₄ were 2.93 and 2.69 eV, respectively. Thus, the E_{VB} of g-C₃N₄ and Ag/g-C₃N₄ were calculated at 2.56 and 2.51 V (vs. NHE at pH 0), respectively.

Furthermore, the E_{VB} values of g-C₃N₄ and Ag/g-C₃N₄ were also estimated by the VB-XPS analysis. As shown in Figures 3.8c, d, the VB edges of the g-C₃N₄ and Ag/g-C₃N₄ composite were obtained at about 2.00 and 2.21 eV, respectively. Then the E_{VB} values of the g-C₃N₄ and Ag/g-C₃N₄ composite can be estimated at the normal hydrogen scale electrode (NHE) by following the Eq. 3.5 [73].

$$E_{NHE}/V = \Phi_{WF} + \Phi_{sample} - 4.44 \quad (3.5)$$

where Φ_{WF} , E_{NHE} , and Φ_{sample} are the electron work functions of the analyzer (4.33 eV), E_{VB} of the samples at NHE scale (pH 7), and obtained VB edge of the samples (eV) using VB-XPS, respectively. Hence, the estimated E_{VB} of g-C₃N₄ and Ag/g-C₃N₄ are 1.89 and 2.10 V (vs. NHE scale at pH 7.0), respectively. Hence, the E_{VB} values of the g-C₃N₄ and Ag/g-C₃N₄ are corrected to be 2.30 and 2.51 V (vs. NHE scale at pH 0) after correction by the addition of 0.413 V. However, the VB-XPS analysis could not match with the Mott-Schottky plot analysis for g-C₃N₄. But in the case of Ag/g-C₃N₄ both data are consistent. On the basis of the Mott-Schottky plot, the band structures of g-C₃N₄ and Ag/g-C₃N₄ are shown in Figure 3.8e.

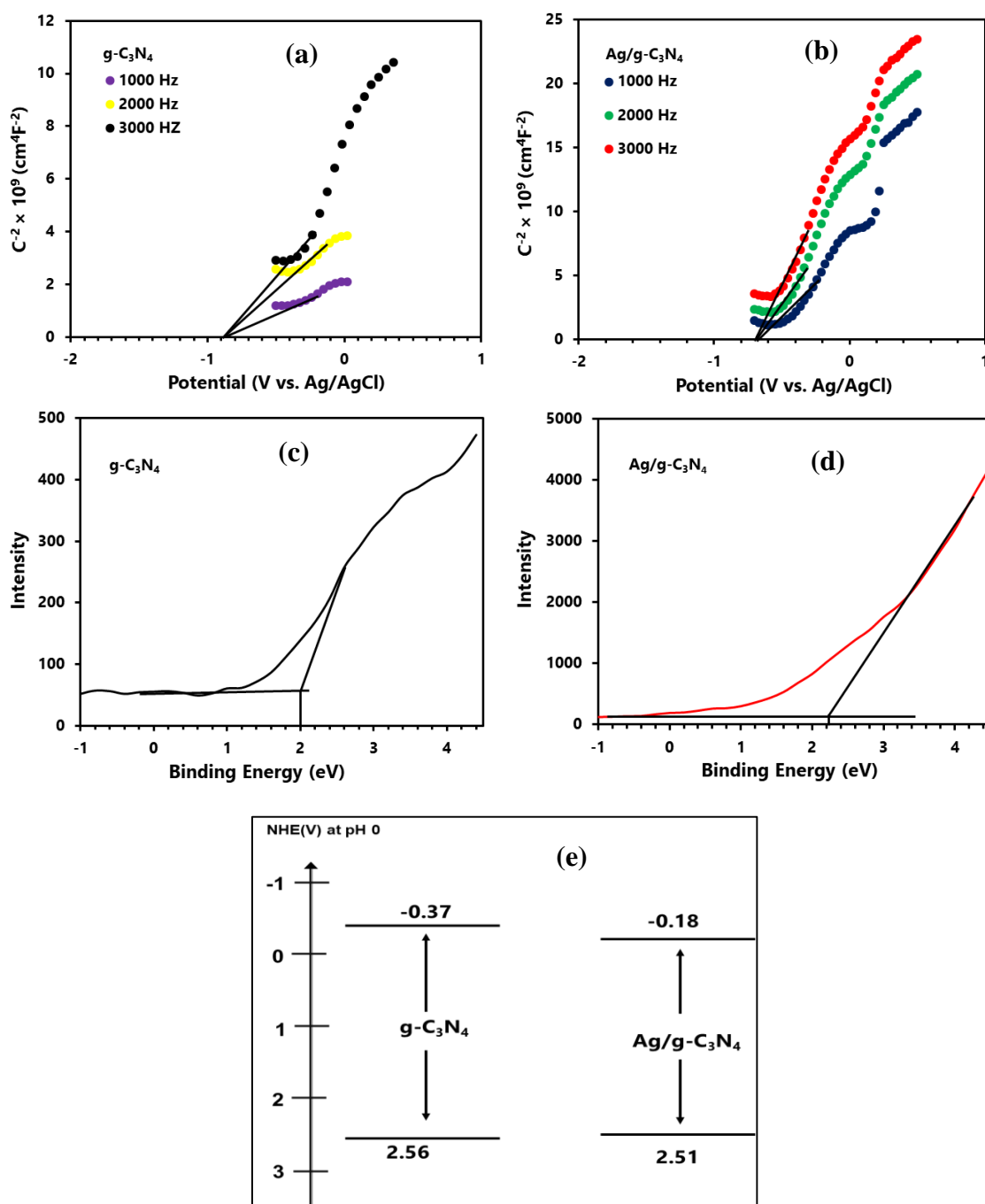


Figure 3.8 Mott-Schottky plots for (a) $g\text{-C}_3\text{N}_4$ and (b) $\text{Ag/g-C}_3\text{N}_4$, VBXPS analysis of (c) $g\text{-C}_3\text{N}_4$ and (d) $\text{Ag/g-C}_3\text{N}_4$, and (e) energy band diagram of $g\text{-C}_3\text{N}_4$ and $\text{Ag/g-C}_3\text{N}_4$.

3.3.11 The Photocatalytic Activity

Under induced visible light, the photocatalytic Cr(VI) reduction by $g\text{-C}_3\text{N}_4$ and $\text{Ag/g-C}_3\text{N}_4$ in both the absence and presence of EDTA was analyzed. As shown in Figure 3.9a, the reduction efficiency of $g\text{-C}_3\text{N}_4$ and $\text{Ag/g-C}_3\text{N}_4$ for Cr(VI) was only 5 and 19% in the absence

of EDTA. Furthermore, in the presence of EDTA, the photocatalytic efficiency of g-C₃N₄ and Ag/g-C₃N₄ for Cr(VI) reduction was increased to 43 and 96%, respectively. Additionally, the linear fitting curves of Cr(VI) reduction follow the pseudo-first-order kinetic equation (Eq. 3.6) perfectly (Figure 3.9b) [74].

$$\ln(C_0/C) = kt \quad (3.6)$$

where C_0 is the initial concentration and C is the concentration of Cr(VI) at time t (min) in ppm, and k is the apparent reaction rate constant in min^{-1} . The calculated rate constant using Ag/g-C₃N₄ (0.1054 min^{-1}) was about 6 times higher than that using g-C₃N₄ (0.0177 min^{-1}) in the presence of EDTA. Hence, the presence of EDTA was favorable for the photocatalytic reduction of Cr(VI) by Ag/g-C₃N₄.

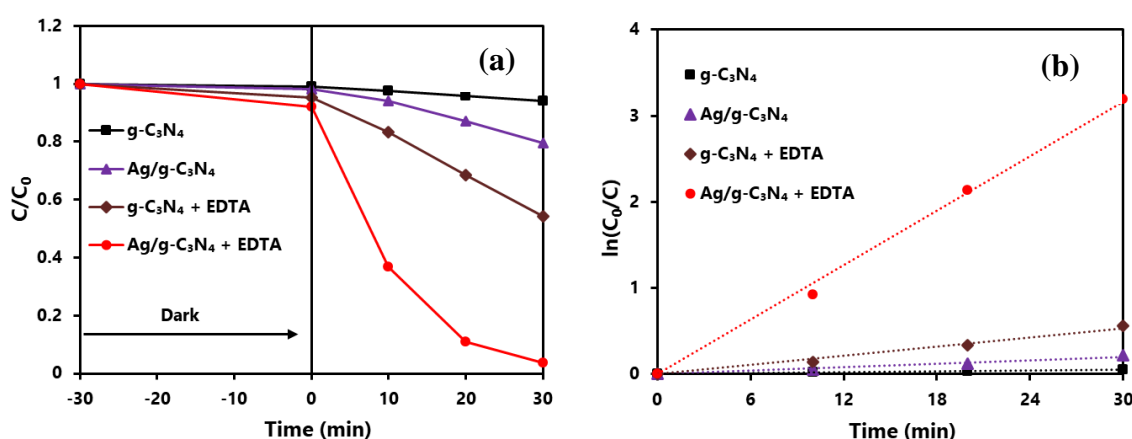


Figure 3.9 (a) Photocatalytic reduction of Cr(VI) with several conditions and (b) corresponding plot of $\ln(C_0/C)$ versus irradiation time; Cr(VI): 20 ppm (30mL), photocatalyst: 40 mg, EDTA-2Na: 400 ppm (EDTA: 314 ppm).

3.3.12 Effect of Ag Content

The photocatalytic studies showed that the amount of Ag content in the composite has a significant impact on the photocatalytic performance. In this regard, Ag/g-C₃N₄ composites were fabricated using different weight percentages of Ag with respect to the weight of urea (0.25 to 1%). As depicted in Figure 3.10, all Ag/g-C₃N₄ have higher photocatalytic efficacy compared to pure g-C₃N₄. And the photocatalytic efficiency of Ag/g-C₃N₄ composites

enhanced with increasing the Ag content in the composite. The Ag/g-C₃N₄ composite prepared from 0.75% Ag with urea exhibited maximum reduction efficiency (95%) in 30 minutes. However, the photocatalytic efficiency decreased when the Ag content further increased. This is because, at low Ag content, Ag plays a role as an electron sink to hinder e^-h^+ pair recombination, but it acts as a charge recombination center and covers the g-C₃N₄ surface at high content [52].

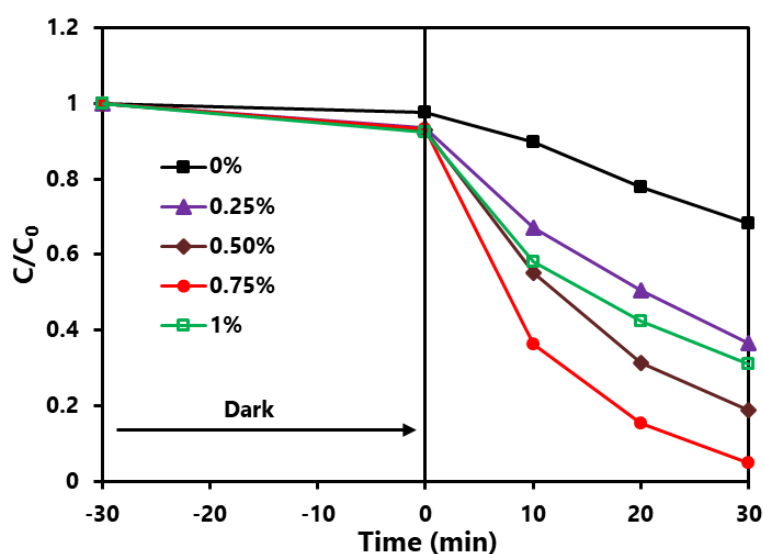


Figure 3.10 Effect of Ag content (percentage of used Ag with respect to the weight of urea in the Ag/g-C₃N₄ preparation) on the photocatalytic Cr(VI) reduction by Ag/g-C₃N₄ in presence of EDTA; Cr(VI): 20 ppm (30mL), photocatalyst: 30 mg, EDTA-2Na: 500 ppm (EDTA: 392 ppm).

3.3.13 Effect of Calcination Temperature and Time

The photocatalytic reduction capability of the Ag/g-C₃N₄ composite was examined by heating it at different temperatures (450, 500, and 550 °C) for 5 h. As shown in Figure 3.11a, the photocatalytic reduction ability of the composite increases with increasing heating temperature. The best result was found at 500 °C for the reduction of Cr(VI), followed by a decrease at higher temperatures (550 °C). The Cr(VI) reduction efficiency of the Ag/g-C₃N₄

composite was also studied by heating at 500 °C for different calcination times (1, 2, 3, 4, and 5 h) (Figure 3.11b). The maximum photocatalytic Cr(VI) reduction efficiency was found at 5 h of calcination time. The charge carrier generation and separation, which are impacted by various factors such as surface area, crystallinity, and particle size, may be primarily responsible for the best activity found in the composite heated at 500 °C for 5 h [75]. By further increasing the calcination temperature, the Ag/g-C₃N₄ composite may be deformed, causing poor visible light absorption and photocatalytic performance [76].

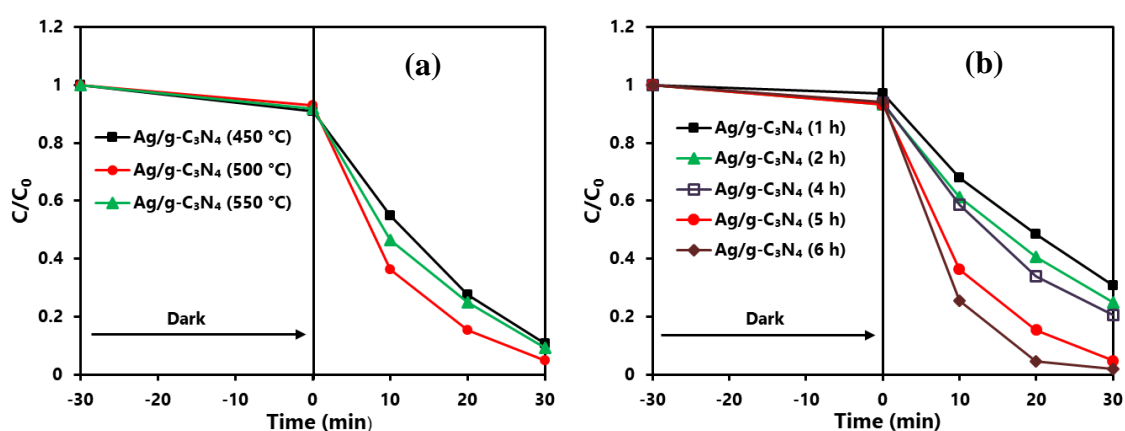


Figure 3.11 Effect of (a) heating temperature for 5 h and (b) calcination time at 500 °C of the composite fabrication on the photocatalytic Cr(VI) reduction by Ag/g-C₃N₄ in presence of EDTA; Cr(VI): 20 ppm (30 mL), photocatalyst: 30 mg, EDTA-2Na: 500 ppm (EDTA: 392 ppm).

3.3.14 Effect of Catalyst Dosages

In order to find the optimal catalyst dosage, the catalyst dosage was varied from 10 to 50 mg without modifying the initial concentration of Cr(VI). As depicted in Figure 3.12a, the different catalyst dosages of 10, 20, 30, and 40 g Ag/g-C₃N₄ composite correspond to photocatalytic reduction percentages of 83, 90, 95, and 96%, respectively. However, reduction percentages decrease to 94% with a further increase in catalyst dosage to 50 mg. Since there are more free active sites on the surface of the catalyst at higher dosages than at lower dosages,

this results in enhanced photocatalytic reduction percentages. Moreover, excessive catalyst dosage can prevent the penetration of visible light onto the catalyst surface, and particles may agglomerate, reducing access for Cr(VI) and radiation to the surface active sites of the catalyst [6,77].

The rate constant was calculated using the $\ln(C_0/C)$ versus irradiation time plot (Figure 3.12b). The kinetic rate constants, k , for 10, 20, 30, 40, and 50 mg of the Ag/g-C₃N₄ composite were 0.0568, 0.0748, 0.0958, 0.1065 and 0.0891 min⁻¹ respectively. This data revealed that 40 mg of Ag/g-C₃N₄ composite has the highest photocatalytic efficiency for the conversion of Cr(VI) to Cr(III). Therefore, 40 mg of Ag/g-C₃N₄ composite was chosen for further study.

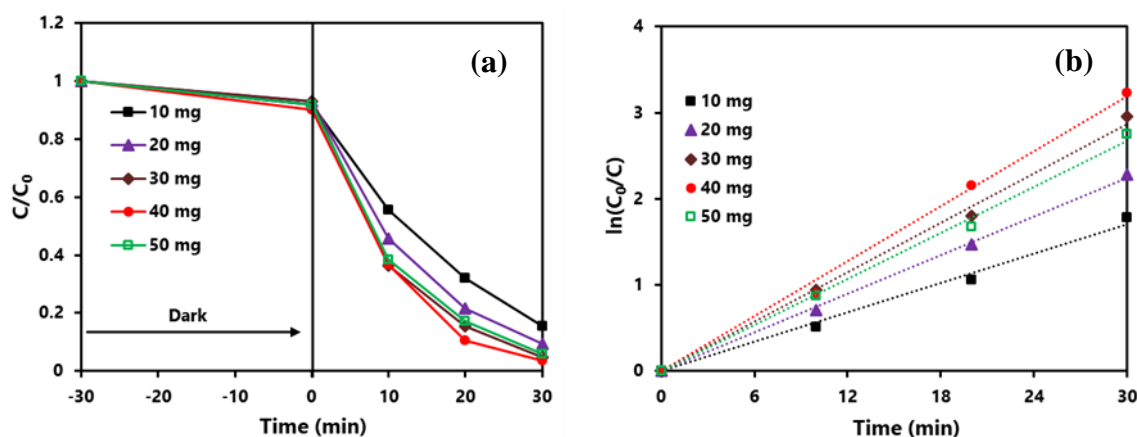


Figure 3.12 (a) Effect of photocatalyst dosage on the photocatalytic Cr(VI) reduction and (b) corresponding Plot of $\ln(C_0/C)$ versus irradiation time; Cr(VI): 20 ppm (30mL), EDTA-2Na: 500 ppm (EDTA: 392 ppm).

3.3.15 Effect of EDTA Concentration

The influence of EDTA concentration on the photocatalytic Cr(VI) reduction was assessed by varying EDTA-2Na concentration from 0 to 500 ppm. As depicted in Figure 3.13 the photocatalytic reduction efficacy of Cr(VI) by Ag/g-C₃N₄ was low without EDTA. However, with the addition of EDTA, the photocatalytic Cr(VI) reduction efficiency was significantly improved. This could be due to various factors: (i) EDTA impeded the re-

oxidation of Cr(III) to Cr(VI) by reacting with the oxidizing agent ($\cdot\text{OH}$); (ii) EDTA suppressed $e^- - h^+$ pair recombination by consuming holes [78,79]. The reactions involved in these factors are represented in Eqs. (3.7-3.9).



Meanwhile, at 400 ppm EDTA-2Na concentration, the photocatalytic reduction of Cr(VI) reached around 96% in 30 minutes. The photocatalytic reduction of Cr(VI) was almost the same as increasing the EDTA-2Na concentration from 400 to 500 ppm. This is because when EDTA concentration is high, EDTA covers Ag/g-C₃N₄ particles and absorbs more light instead of Ag/g-C₃N₄ [80].

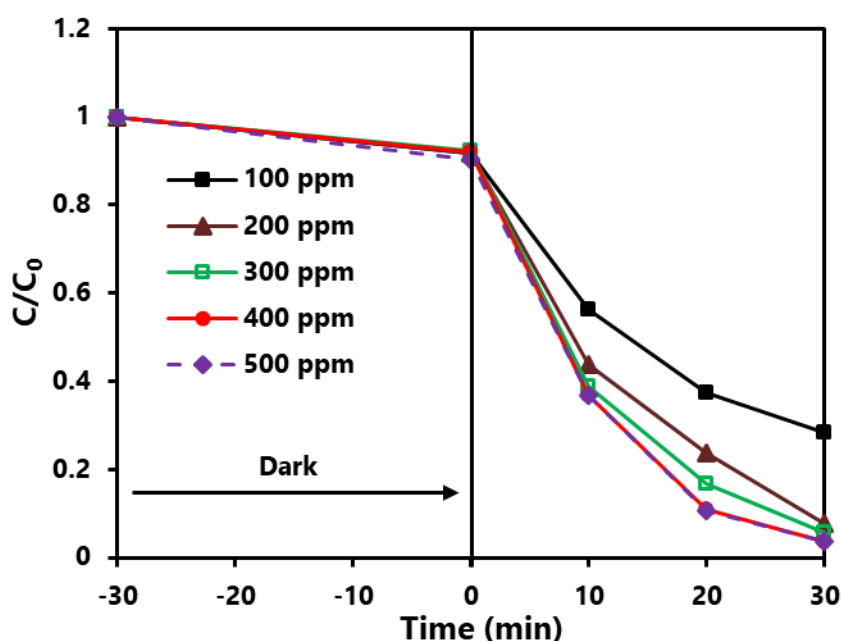


Figure 3.13 Effect of EDTA on the photocatalytic Cr(VI) reduction by Ag/g-C₃N₄; Cr(VI): 20 ppm (30mL), photocatalyst: 40 mg.

3.3.16 Effect of Initial Concentration

The photocatalytic efficiency of Ag/g-C₃N₄ was further examined by changing initial concentrations of Cr(VI) ranging from 5 to 30 ppm. The results are shown in Figure 3.14a. The photocatalytic Cr(VI) reduction was higher for the lower concentration of Cr(VI) (5 ppm) due to the higher catalytic activity sites of 40 mg of Ag/g-C₃N₄ composite. As the initial concentration of Cr(VI) was raised from 5 to 30 ppm, the photocatalytic efficacy of the reaction decreased. This behavior is owing to the higher amount of Cr(VI) ions that block the active sites and boost the shielding effect of the Ag/g-C₃N₄ composite during the process, resulting in a lower conversion of Cr(VI) ~ Cr(III) [75,77]. However, the amount of reduced chromium increased as the initial concentration of Cr(VI) increased (Figure 3.14b). So for practical application, Cr(VI) concentration of 5 or 10 ppm was quite insignificant; 20 ppm of Cr(VI) was adopted as the initial concentration for the further experiment.

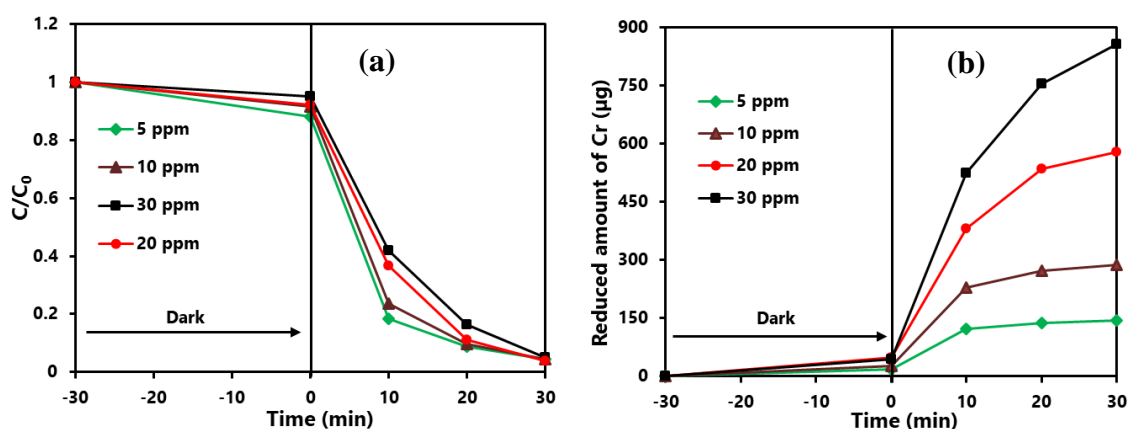
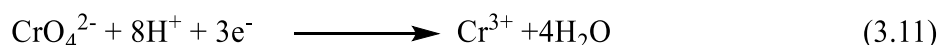
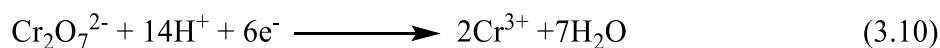


Figure 3.14 Effect of initial concentration on (a) photocatalytic Cr(VI) reduction and (b) reduced amount of Cr by Ag/g-C₃N₄ in presence of EDTA; Cr(VI): 20 ppm (30mL), photocatalyst: 40 mg, EDTA-2Na: 400 ppm (EDTA: 314 ppm).

3.3.17 Effect of pH

It is well known that pH has an immense effect on the photocatalytic conversion of Cr(VI) ~ Cr(III). Therefore, a series of experiments were carried out at various pH (2, 4, 6, and

8) to understand the pH effect (Figure 3.15). The aqueous solution of Cr(VI) had an initial pH of 2.65. It was observed that the acidic condition (pH 2) showed maximum photocatalytic reduction, and the photocatalytic reduction of Cr(VI) decreased as the pH value increased. The photocatalytic reduction reaction of Cr(VI) is as follows:



This suggests that Cr(VI)'s redox potential is significantly influenced by the solution pH. In essence, the reduction potential drastically increased at low pH due to the large concentration of H^+ in the solution, proving that acidic conditions are more favorable for Cr(VI) photo-reduction [81]. Furthermore, the protonation capability of the catalyst became weak, and the Cr^{3+} ions precipitated as $\text{Cr}(\text{OH})_3$ on the catalyst's surface when the pH was greater than 7, which is related to inferior reduction ability [82].

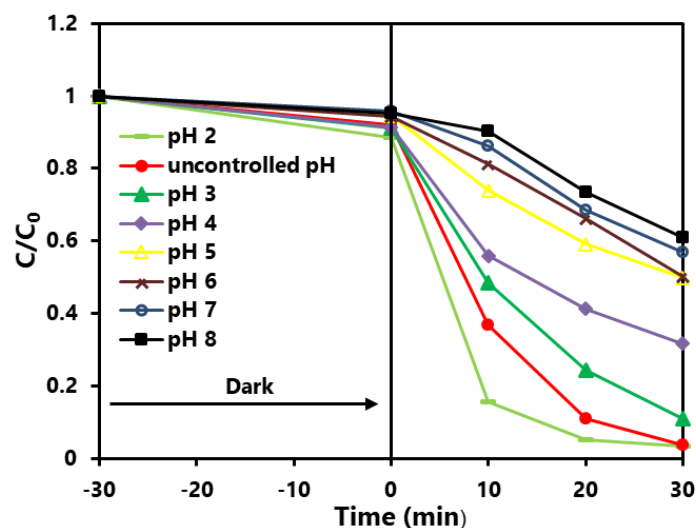


Figure 3.15 Effect of initial pH on the photocatalytic Cr(VI) reduction by Ag/g-C₃N₄ in presence of EDTA; Cr(VI): 20 ppm (30mL), photocatalyst: 40 mg, EDTA-2Na: 400 ppm (EDTA: 314 ppm).

3.3.18 Reaction Mechanism

According to the XRD observation, the interlayered distance of the conjugated aromatic system was decreased in Ag/g-C₃N₄. Upon the irradiation of visible light in the photocatalytic reaction, the light is more scattered and interact with the Ag/g-C₃N₄ compared to the g-C₃N₄, because of the decreasing interlayer distance (Figure 3.16a). Hence, the photocatalytic Cr(VI) reduction ability of Ag/g-C₃N₄ was increased compared to g-C₃N₄. The schematic diagram of a probable mechanism for photocatalytic activity of the Ag/g-C₃N₄ composite for Cr(VI) reduction is shown in Figure 3.16b. When visible light is irradiated over Ag/g-C₃N₄, g-C₃N₄ absorbs photons efficiently and generates valance band (VB) holes (h⁺) and conduction band (CB) electrons (e⁻) as shown in Eq. 3.13. Therefore, h⁺ remains at the VB of g-C₃N₄ and e⁻ is excited to the CB of g-C₃N₄. In addition, Ag is situated between valance and conduction band of the g-C₃N₄. It can be proposed that the CB electrons in g-C₃N₄ were rapidly transferred to Ag (Eq. 3.14). And, the recombination rate of photogenerated e⁻-h⁺ is decreased, and the lifetime of photogenerated electrons is increased. Furthermore, like other noble metals, dispersed Ag on Ag/g-C₃N₄ can absorb photons to generate active "hot electrons" through SPR excitation, as shown in Eq. 3.15 [54,68,83–85]. All of the electrons transferred from g-C₃N₄ and SPR excitation assembled on the Ag surface [54]. Finally, all the accumulated electrons on the Ag surface to participate in the photocatalytic reduction of Cr(VI) (Eq. 3.16), because of the lower standard reduction potential of Cr⁶⁺/Cr³⁺ [E (Cr⁶⁺/Cr³⁺) = +1.23 V vs. NHE at pH 0] [86].

Again, EDTA can trap the produced holes and inhibit the recombination rate of photogenerated e⁻-h⁺ pairs, which are supplied to the photocatalytic process (Eqs. 3.7-3.9). The solution turned pink color after 30 minutes, indicating that Cr(VI) had been reduced to Cr(III) and cleaning the surface by reducing Cr(III) through the formation of the [Cr(III)-EDTA]³⁺ complex (Eq. 3.17).

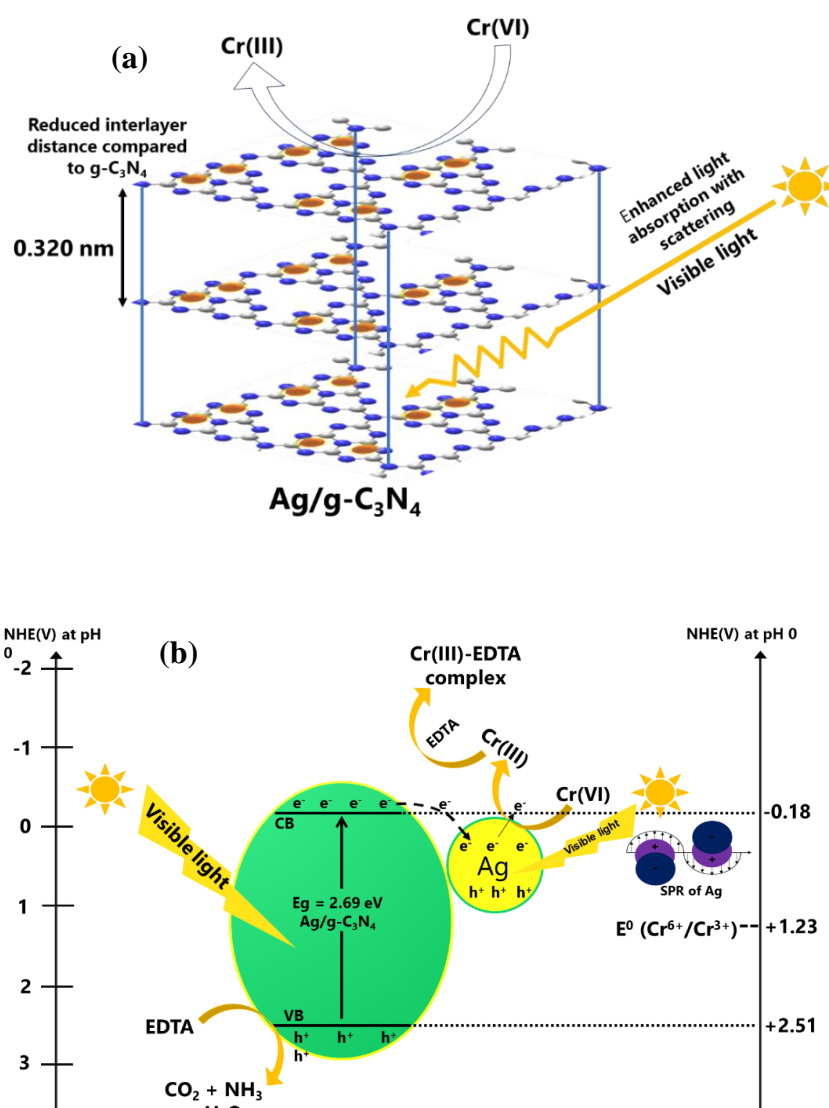
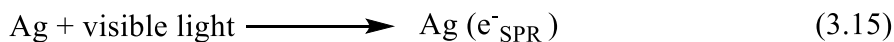


Figure 3.16 (a) Interaction of scattered visible light with Ag/g-C₃N₄ and (b) Proposed mechanisms for photocatalytic reduction of Cr(VI) by Ag/g-C₃N₄ in presence of EDTA.

3.3.19 Reusability

Apart from excellent efficiency, a photocatalyst needs to have stability for its practical application. So recycling photocatalytic reduction of Cr(VI) experiments were performed in the presence of EDTA to evaluate the stability of the Ag/g-C₃N₄ composite. The result in Figure 3.17 shows that the reduction efficiency only decreased from 96 to 87% after four runs. These findings suggest that Ag/g-C₃N₄ has strong stability and a repeatable ability to reduce Cr(VI). The photocatalytic Cr(VI) reduction efficiency of the synthesized Ag/g-C₃N₄ composite in the present study is compared with reported recent studies of g-C₃N₄-based photocatalysts. From Table 3.2, it is observed that the synthesized Ag/g-C₃N₄ composite in the present study is an excellent photocatalyst for Cr(VI) reduction.

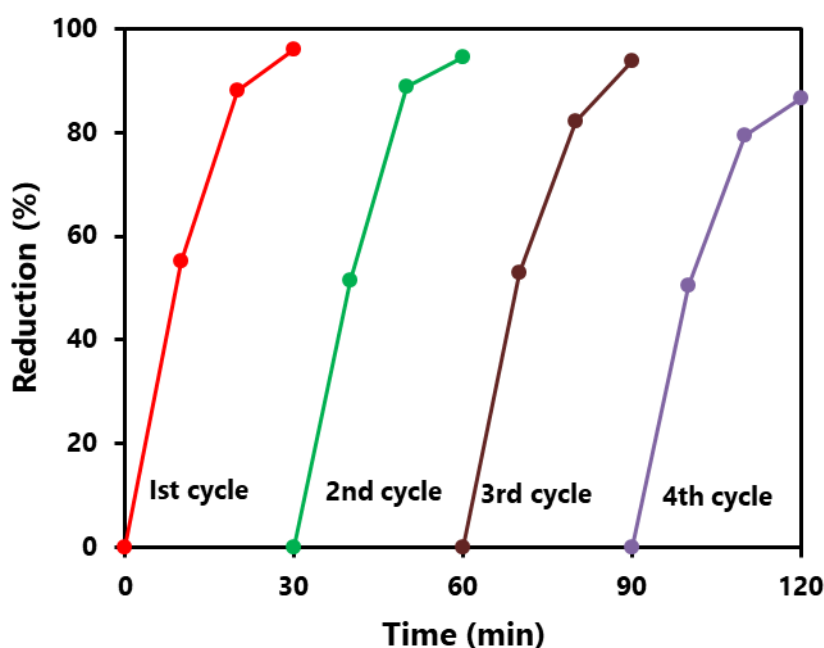


Figure 3.17 Reusability of Ag/g-C₃N₄ on the photocatalytic Cr(VI) reduction in presence of EDTA.

Table 3.2 Photocatalytic Cr(VI) reduction activity of synthesized Ag/g-C₃N₄ composite and some other recent reported g-C₃N₄-based composite

Photocatalyst (Scavenger)	Cr(VI) solution (mg L ⁻¹)	light	Irradiation time (min)	Reduction (%)	Rate constant (min ⁻¹)	Reusability	References
Ag/g-C ₃ N ₄ (EDTA)	20	Visible	30	96	0.1054	4	Current Study
ZnO/g-C ₃ N ₄	20	Visible	180	98	0.0175	5	Khatun et al. 2023
Microdisk-like g-C ₃ N ₄ /Ag/AgCl	20	Visible	45	-	0.0740	4	He et al. 2019
AgI/CeO ₂ @ g-C ₃ N ₄	15	Visible	75	99.6	0.058	4	Kohantorabi et al. 2021
Ag@AgI/FeVO ₄ / g-C ₃ N ₄	4.2	Visible	60	100	0.0525	5	Yang et al. 2023
Ag-disperse g-C ₃ N ₄ (EDTA)	10	UV	120	100	0.1200	-	Islam et al. 2023

3.4 Conclusions

In conclusion, the Ag/g-C₃N₄ composite in response to visible light was prepared by a one-step calcination process. The amount of Ag content in the Ag/g-C₃N₄ composite affected the photocatalytic performance of the Ag/g-C₃N₄ composite, and the 22 wt% Ag/g-C₃N₄ composite showed the best photocatalytic activity. According to TG, XRD, FTIR, XPS, BET, SEM, and TEM studies, the Ag/g-C₃N₄ composite was successfully synthesized. UV-visible DRS, PL, and EIS measurements showed strong absorption of visible light, low intensity peak, and small semicircle radius, respectively. The findings revealed that the lower e⁻-h⁺ pair recombination and enhanced charge separation of Ag/g-C₃N₄ were responsible for its better photocatalytic activity. The Ag/g-C₃N₄ composite showed better photocatalytic efficiency toward the Cr(VI) reduction in the presence of EDTA. Under the optimized condition, the reduction of Cr(VI) can reach 96% as follows: Cr(VI) = 20 ppm, catalyst = 40 mg, and EDTA-2Na = 400 ppm. Interestingly, the photocatalytic reduction of Cr(VI) is boosted at a lower pH (pH = 2). Moreover, the photocatalyst recyclability was also investigated and repeated up to 4th cycles (86%).

3.5 References

1. Yang, G.; Wang, L.; Zheng, S.; Wu, H.; Hao, D.; Li, Q.; Du, H.; Yamashita, H.; Wang, Q. Novel Dual Z-Scheme Ag-Bridged AgI/FeVO₄-C₃N₄ Plasmonic Heterojunction: A Study on the Performance and Mechanism of Photocatalytic Reduction of Cr(VI). *J. Environ. Chem. Eng.* **2023**, *11*, 110071, doi:10.1016/j.jece.2023.110071.
2. Diao, Z.-H.; Yan, L.; Dong, F.-X.; Chen, Z.-L.; Guo, P.-R.; Qian, W.; Zhang, W.-X.; Liang, J.-Y.; Huang, S.-T.; Chu, W. Ultrasound-Assisted Catalytic Reduction of Cr(VI) by an Acid Mine Drainage Based nZVI Coupling with FeS₂ System from Aqueous Solutions: Performance and Mechanism. *J. Environ. Manage.* **2021**, *278*, 111518, doi:10.1016/j.jenvman.2020.111518.
3. Zhong, Y.; Qiu, X.; Chen, D.; Li, N.; Xu, Q.; Li, H.; He, J.; Lu, J. Flexible Electrospun Carbon Nanofiber/Tin(IV) Sulfide Core/Sheath Membranes for Photocatalytically Treating Chromium(VI)-Containing Wastewater. *ACS Appl. Mater. Interfaces* **2016**, *8*, 28671–28677, doi:10.1021/acsami.6b10241.
4. Jiang, B.; Liu, Y.; Zheng, J.; Tan, M.; Wang, Z.; Wu, M. Synergetic Transformations of Multiple Pollutants Driven by Cr(VI)–Sulfite Reactions. *Environ. Sci. Technol.* **2015**, *49*, 12363–12371, doi:10.1021/acs.est.5b03275.
5. Zhang, S.; Lan, H.; Cui, Y.; An, X.; Liu, H.; Qu, J. Insight into the Key Role of Cr Intermediates in the Efficient and Simultaneous Degradation of Organic Contaminants and Cr(VI) Reduction via g-C₃N₄ -Assisted Photocatalysis. *Environ. Sci. Technol.* **2022**, *56*, 3552–3563, doi:10.1021/acs.est.1c08440.

6. Prabakaran, E.; Pillay, K. Self-Assembled Silver Nanoparticles Decorated on Exfoliated Graphitic Carbon Nitride/Carbon Sphere Nanocomposites as a Novel Catalyst for Catalytic Reduction of Cr(VI) to Cr(III) from Wastewater and Reuse for Photocatalytic Applications. *ACS Omega* **2021**, *6*, 35221–35243, doi:10.1021/acsomega.1c00866.
7. Hu, X.; Zhao, Y.; Wang, H.; Cai, X.; Hu, X.; Tang, C.; Liu, Y.; Yang, Y. Decontamination of Cr(VI) by Graphene oxide@TiO₂ in an Aerobic Atmosphere: Effects of pH, Ferric Ions, Inorganic Anions, and Formate. *J. Chem. Technol. Biotechnol.* **2018**, *93*, 2226–2233, doi:10.1002/jctb.5565.
8. Zhao, Z.; An, H.; Lin, J.; Feng, M.; Murugadoss, V.; Ding, T.; Liu, H.; Shao, Q.; Mai, X.; Wang, N.; et al. Progress on the Photocatalytic Reduction Removal of Chromium Contamination. *Chem. Rec.* **2019**, *19*, 873–882, doi:10.1002/tcr.201800153.
9. Dong, Y.; Wang, P.; Gan, L.; Li, B.; Wen, H. Enhanced Removal of Aqueous Cr(VI) Using Optimized Fe Complex on EDTA Modified Cotton Fiber via Photocatalytic Reduction and Adsorption Hybrid Functions. *Cellulose* **2019**, *26*, 7383–7397, doi:10.1007/s10570-019-02598-4.
10. Islam, J.B.; Islam, M.R.; Furukawa, M.; Tateishi, I.; Katsumata, H.; Kaneco, S. Performance of EDTA Modified Magnetic ZnFe₂O₄ during Photocatalytic Reduction of Cr(VI) in Aqueous Solution under UV Irradiation. *J. Environ. Sci. Heal. Part A* **2021**, *56*, 44–51, doi:10.1080/10934529.2020.1835389.
11. Li, G.; Wu, Y.; Zhang, M.; Chu, B.; Huang, W.; Fan, M.; Dong, L.; Li, B. Enhanced Removal of Toxic Cr(VI) in Wastewater by Synthetic TiO₂/g-C₃N₄ Microspheres/rGO

- Photocatalyst under Irradiation of Visible Light. *Ind. Eng. Chem. Res.* **2019**, 58, 8979–8989, doi:10.1021/acs.iecr.8b05990.
12. Ding, J.; Pu, L.; Wang, Y.; Wu, B.; Yu, A.; Zhang, X.; Pan, B.; Zhang, Q.; Gao, G. Adsorption and Reduction of Cr(VI) Together with Cr(III) Sequestration by Polyaniline Confined in Pores of Polystyrene Beads. *Environ. Sci. Technol.* **2018**, 52, 12602–12611, doi:10.1021/acs.est.8b02566.
 13. He, C.; Gu, L.; Xu, Z.; He, H.; Fu, G.; Han, F.; Huang, B.; Pan, X. Cleaning Chromium Pollution in Aquatic Environments by Bioremediation, Photocatalytic Remediation, Electrochemical Remediation and Coupled Remediation Systems. *Environ. Chem. Lett.* **2020**, 18, 561–576, doi:10.1007/s10311-019-00960-3.
 14. He, H.; Li, J.; Yu, C.; Luo, Z. Surface Decoration of Microdisk-like g-C₃N₄/diatomite with Ag/AgCl Nanoparticles for Application in Cr(VI) Reduction. *Sustain. Mater. Technol.* **2019**, 22, e00127, doi:10.1016/j.susmat.2019.e00127.
 15. Shi, L.; Wang, T.; Zhang, H.; Chang, K.; Meng, X.; Liu, H.; Ye, J. An Amine-Functionalized Iron(III) Metal–Organic Framework as Efficient Visible-Light Photocatalyst for Cr(VI) Reduction. *Adv. Sci.* **2015**, 2, doi:10.1002/advs.201500006.
 16. Islam, J.B.; Furukawa, M.; Tateishi, I.; Kawakami, S.; Katsumata, H.; Kaneco, S. Enhanced Photocatalytic Reduction of Toxic Cr(VI) with Cu Modified ZnO Nanoparticles in Presence of EDTA under UV Illumination. *SN Appl. Sci.* **2019**, 1, 1240, doi:10.1007/s42452-019-1282-x.
 17. Song, X.-Y.; Chen, Q.-L. Facile Preparation of g-C₃N₄/Bi₂WO₆ Hybrid Photocatalyst with

- Enhanced Visible Light Photoreduction of Cr(VI). *J. Nanoparticle Res.* **2019**, *21*, 183, doi:10.1007/s11051-019-4632-0.
18. Alaghmandfard, A.; Ghandi, K. A Comprehensive Review of Graphitic Carbon Nitride (g-C₃N₄)–Metal Oxide-Based Nanocomposites: Potential for Photocatalysis and Sensing. *Nanomaterials* **2022**, *12*, 294, doi:10.3390/nano12020294.
19. Li, X.; Zhu, L.; Zhou, Y.; Yin, H.; Ai, S. Enhanced Photoelectrochemical Method for Sensitive Detection of Protein Kinase A Activity Using TiO₂/g-C₃N₄, PAMAM Dendrimer, and Alkaline Phosphatase. *Anal. Chem.* **2017**, *89*, 2369–2376, doi:10.1021/acs.analchem.6b04184.
20. Khatun, A.; Suhag, M.H.; Tateishi, I.; Furukawa, M.; Katsumata, H.; Kaneco, S. Facile Synthesis of ZnO/g-C₃N₄ with Enhanced Photocatalytic Performance for the Reduction of Cr(VI) in Presence of EDTA Under Visible Light Irradiation. *Int. J. Environ. Res.* **2023**, *17*, 32, doi:10.1007/s41742-023-00522-0.
21. Krishna Kumar, A.S.; You, J.-G.; Tseng, W.-B.; Dwivedi, G.D.; Rajesh, N.; Jiang, S.-J.; Tseng, W.-L. Magnetically Separable Nanospherical g-C₃N₄@Fe₃O₄ as a Recyclable Material for Chromium Adsorption and Visible-Light-Driven Catalytic Reduction of Aromatic Nitro Compounds. *ACS Sustain. Chem. Eng.* **2019**, *7*, 6662–6671, doi:10.1021/acssuschemeng.8b05727.
22. Zhao, L.; Guo, L.; Tang, Y.; Zhou, J.; Shi, B. Novel g-C₃N₄/C/Fe₂O₃ Composite for Efficient Photocatalytic Reduction of Aqueous Cr(VI) under Light Irradiation. *Ind. Eng. Chem. Res.* **2021**, *60*, 13594–13603, doi:10.1021/acs.iecr.1c02411.

23. Tang, J.; Xu, R.; Sui, G.; Guo, D.; Zhao, Z.; Fu, S.; Yang, X.; Li, Y.; Li, J. Double-Shelled Porous g-C₃N₄ Nanotubes Modified with Amorphous Cu-Doped FeOOH Nanoclusters as 0D/3D Non-Homogeneous Photo-Fenton Catalysts for Effective Removal of Organic Dyes. *Small* **2023**, *19*, 2208232, doi:10.1002/sml.202208232.
24. Nallusamy, S.; Asaithambi, S.; Pandiaraj, S.; Rahaman, M.; Elangovan, V.; Eswaramoorthy, N.; Nandagopal, C. Cerium-Modified TiO₂/g-C₃N₄ Nanocomposites with Synergistic Effect on Enhancing Visible-Light Photocatalytic Activity Employing Cationic Dyes. *Colloids Surfaces A Physicochem. Eng. Asp.* **2024**, *685*, 133175, doi:10.1016/j.colsurfa.2024.133175.
25. Khan, M.A.; Mutahir, S.; Wang, F.; Zhen, H.; Lei, W.; Xia, M.; Ouyang, Y.; Muhmood, T. Synthesis of Environmentally Encouraged, Highly Robust Pollutants Reduction 3-D System Consisting of Ag/g-C₃N₄ and Cu-Complex to Degrade Refractory Pollutants. *J. Photochem. Photobiol. A Chem.* **2018**, *364*, 826–836, doi:10.1016/j.jphotochem.2018.04.035.
26. Wang, X.; Tan, F.; Wang, W.; Qiao, X.; Qiu, X.; Chen, J. Anchoring of Silver Nanoparticles on Graphitic Carbon Nitride Sheets for the Synergistic Catalytic Reduction of 4-Nitrophenol. *Chemosphere* **2017**, *172*, 147–154, doi:10.1016/j.chemosphere.2016.12.103.
27. Sui, G.; Li, J.; Du, L.; Zhuang, Y.; Zhang, Y.; Zou, Y.; Li, B. Preparation and Characterization of g-C₃N₄/Ag–TiO₂ Ternary Hollowsphere Nanoheterojunction Catalyst with High Visible Light Photocatalytic Performance. *J. Alloys Compd.* **2020**, *823*, 153851, doi:10.1016/j.jallcom.2020.153851.
28. Cako, E.; Dudziak, S.; Głuchowski, P.; Trykowski, G.; Pisarek, M.; Fiszka Borzyszkowska,

- A.; Sikora, K.; Zielińska-Jurek, A. Heterojunction of (P, S) Co-Doped g-C₃N₄ and 2D TiO₂ for Improved Carbamazepine and Acetaminophen Photocatalytic Degradation. *Sep. Purif. Technol.* **2023**, *311*, 123320, doi:10.1016/j.seppur.2023.123320.
29. Xu, R.; Li, J.; Sui, G.; Zhuang, Y.; Guo, D.; Luo, Z.; Liang, S.; Yao, H.; Wang, C.; Chen, S. Constructing Supramolecular Self-Assembled Porous g-C₃N₄ Nanosheets Containing Thiophene-Groups for Excellent Photocatalytic Performance under Visible Light. *Appl. Surf. Sci.* **2022**, *578*, 152064, doi:10.1016/j.apsusc.2021.152064.
30. Li, Z.; Wang, W.; Liu, Q.; Zhang, Z.; Fang, X. In-Situ Microwave-Assisted Heating Synthesis of a High-Performance g-C₃N₄/carbon Nanotubes Composite Photocatalyst with Good Contact Interfaces. *Mater. Res. Bull.* **2018**, *106*, 152–161, doi:10.1016/j.materresbull.2018.06.004.
31. Suhag, M.H.; Katsumata, H.; Tateishi, I.; Furukawa, M.; Kaneco, S. Black Phosphorus-Doped Graphitic Carbon Nitride with Aromatic Benzene Rings for Efficient Photocatalytic Hydrogen Production. *Langmuir* **2023**, *39*, 13121–13131, doi:10.1021/acs.langmuir.3c01518.
32. Liang, S.; Sui, G.; Guo, D.; Luo, Z.; Xu, R.; Yao, H.; Li, J.; Wang, C. g-C₃N₄ -Wrapped Nickel Doped Zinc Oxide/carbon Core-Double Shell Microspheres for High-Performance Photocatalytic Hydrogen Production. *J. Colloid Interface Sci.* **2023**, *635*, 83–93, doi:10.1016/j.jcis.2022.12.120.
33. Shoran, S.; Chaudhary, S.; Sharma, A. Photocatalytic Dye Degradation and Antibacterial Activities of CeO₂/g-C₃N₄ Nanomaterials for Environmental Applications. *Environ. Sci.*

- Pollut. Res.* **2022**, *30*, 98682–98700, doi:10.1007/s11356-022-23815-x.
34. Xu, R.; Li, J.; Sui, G.; Zhuang, Y.; Guo, D.; Luo, Z.; Liang, S.; Yao, H.; Wang, C. Construction of Novel CdS@CuS/g-C₃N₄ Heterojunctions for Efficient Visible Light-Driven Photo-Fenton Degradation Performance. *Colloids Surfaces A Physicochem. Eng. Asp.* **2023**, *659*, 130598, doi:10.1016/j.colsurfa.2022.130598.
 35. Wang, Z.; Li, J.; Fu, S.; Guo, D.; Tang, J.; Yang, X.; Xu, R.; Sui, G.; Chen, S. Construction of MoS₂/CdS/Bi₂MoO₆ Z-Scheme Photocatalyst for Efficient Photocatalytic Degradation under Visible-Light. *J. Solid State Chem.* **2023**, *322*, 123957, doi:10.1016/j.jssc.2023.123957.
 36. Wu, J.-H.; Shao, F.-Q.; Luo, X.-Q.; Xu, H.-J.; Wang, A.-J. Pd Nanocones Supported on g-C₃N₄: An Efficient Photocatalyst for Boosting Catalytic Reduction of Hexavalent Chromium under Visible-Light Irradiation. *Appl. Surf. Sci.* **2019**, *471*, 935–942, doi:10.1016/j.apsusc.2018.12.075.
 37. Wang, M.; Zeng, Y.; Dong, G.; Wang, C. Br-Doping of g-C₃N₄ towards Enhanced Photocatalytic Performance in Cr(VI) Reduction. *Chinese J. Catal.* **2020**, *41*, 1498–1510, doi:10.1016/S1872-2067(19)63435-2.
 38. Patnaik, S.; Sahoo, D.P.; Parida, K.M. Bimetallic Co-Effect of Au-Pd Alloyed Nanoparticles on Mesoporous Silica Modified g-C₃N₄ for Single and Simultaneous Photocatalytic Oxidation of Phenol and Reduction of Hexavalent Chromium. *J. Colloid Interface Sci.* **2020**, *560*, 519–535, doi:10.1016/j.jcis.2019.09.041.
 39. He, Q.; Zhou, F.; Zhan, S.; Yang, Y.; Liu, Y.; Tian, Y.; Huang, N. Enhancement of

- Photocatalytic and Photoelectrocatalytic Activity of Ag Modified Mp g-C₃N₄ Composites. *Appl. Surf. Sci.* **2017**, *391*, 423–431, doi:10.1016/j.apsusc.2016.07.005.
40. Nguyen, T.T.; Bui, H.T.; Nguyen, G.T.; Hoang, T.N.; Van Tran, C.; Ho, P.H.; Hoai Nguyen, P.T.; Kim, J.Y.; Chang, S.W.; Chung, W.J.; et al. Facile Preparation of Porphyrin@g-C₃N₄/Ag Nanocomposite for Improved Photocatalytic Degradation of Organic Dyes in Aqueous Solution. *Environ. Res.* **2023**, *231*, 115984, doi:10.1016/j.envres.2023.115984.
41. Min, C.; Shen, C.; Li, R.; Li, Y.; Qin, J.; Yang, X. In-Situ Fabrication of Ag/g-C₃N₄ Composite Materials with Improved Photocatalytic Activity by Coordination-Driven Assembly of Precursors. *Ceram. Int.* **2016**, *42*, 5575–5581, doi:10.1016/j.ceramint.2015.12.042.
42. Muñoz-Batista, M.J.; Fontelles-Carceller, O.; Ferrer, M.; Fernández-García, M.; Kubacka, A. Disinfection Capability of Ag/g-C₃N₄ Composite Photocatalysts under UV and Visible Light Illumination. *Appl. Catal. B Environ.* **2016**, *183*, 86–95, doi:10.1016/j.apcatb.2015.10.024.
43. Zhang, W.; Zhou, L.; Deng, H. Ag Modified g-C₃N₄ Composites with Enhanced Visible-Light Photocatalytic Activity for Diclofenac Degradation. *J. Mol. Catal. A Chem.* **2016**, *423*, 270–276, doi:10.1016/j.molcata.2016.07.021.
44. Ren, T.; Dang, Y.; Xiao, Y.; Hu, Q.; Deng, D.; Chen, J.; He, P. Depositing Ag Nanoparticles on g-C₃N₄ by Facile Silver Mirror Reaction for Enhanced Photocatalytic Hydrogen Production. *Inorg. Chem. Commun.* **2021**, *123*, 108367, doi:10.1016/j.inoche.2020.108367.
45. Islam, J.B.; Islam, M.R.; Furukawa, M.; Tateishi, I.; Katsumata, H.; Kaneco, S. Ag-

- Modified g-C₃N₄ with Enhanced Activity for the Photocatalytic Reduction of Hexavalent Chromium in the Presence of EDTA under Ultraviolet Irradiation. *Environ. Technol.* **2023**, *44*, 3627–3640, doi:10.1080/09593330.2022.2068379.
46. Bao, C.; Chen, M.; Jin, X.; Hu, D.; Huang, Q. Efficient and Stable Photocatalytic Reduction of Aqueous Hexavalent Chromium Ions by Polyaniline Surface-Hybridized ZnO Nanosheets. *J. Mol. Liq.* **2019**, *279*, 133–145, doi:10.1016/j.molliq.2019.01.122.
47. Han, Z.; Wang, N.; Fan, H.; Ai, S. Ag Nanoparticles Loaded on Porous Graphitic Carbon Nitride with Enhanced Photocatalytic Activity for Degradation of Phenol. *Solid State Sci.* **2017**, *65*, 110–115, doi:10.1016/j.solidstatesciences.2017.01.010.
48. Azizi-Toupkanloo, H.; Karimi-Nazarabad, M.; Shakeri, M.; Eftekhari, M. Photocatalytic Mineralization of Hard-Degradable Morphine by Visible Light-Driven Ag@g-C₃N₄ Nanostructures. *Environ. Sci. Pollut. Res.* **2019**, *26*, 30941–30953, doi:10.1007/s11356-019-06274-9.
49. Zhao, H.; Yu, H.; Quan, X.; Chen, S.; Zhang, Y.; Zhao, H.; Wang, H. Fabrication of Atomic Single Layer Graphitic-C₃N₄ and Its High Performance of Photocatalytic Disinfection under Visible Light Irradiation. *Appl. Catal. B Environ.* **2014**, *152-153*, 46–50, doi:10.1016/j.apcatb.2014.01.023.
50. Vu, M.-H.; Sakar, M.; Nguyen, C.-C.; Do, T.-O. Chemically Bonded Ni Cocatalyst onto the S Doped g-C₃N₄ Nanosheets and Their Synergistic Enhancement in H₂ Production under Sunlight Irradiation. *ACS Sustain. Chem. Eng.* **2018**, *6*, 4194–4203, doi:10.1021/acssuschemeng.7b04598.

-
51. Ishak, N.; Jeyalakshmi, V.; Setka, M.; Grandcolas, M.; Devadas, B.; Šoóš, M. Upgrading of g-C₃N₄ Semiconductor by a Nitrogen-Doped Carbon Material: A Photocatalytic Degradation Application. *J. Environ. Chem. Eng.* **2023**, *11*, 109381, doi:10.1016/j.jece.2023.109381.
52. Jin, J.; Liang, Q.; Ding, C.; Li, Z.; Xu, S. Simultaneous Synthesis-Immobilization of Ag Nanoparticles Functionalized 2D g-C₃N₄ Nanosheets with Improved Photocatalytic Activity. *J. Alloys Compd.* **2017**, *691*, 763–771, doi:10.1016/j.jallcom.2016.08.302.
53. Song, Y.; Gao, S.; Tian, J.; Zhang, H. Construction of Ag/g-C₃N₄ Composites with Uniform-Sized Ag Nanoparticles and the Application for Sulfisoxazole Degradation in the Presence of Visible Radiation. *J. Environ. Chem. Eng.* **2020**, *8*, 104390, doi:10.1016/j.jece.2020.104390.
54. Li, Y.; Liu, Z.; Li, Z.; Wang, Q. Renewable Biomass-Derived Carbon-Supported g-C₃N₄ Doped with Ag for Enhanced Photocatalytic Reduction of CO₂. *J. Colloid Interface Sci.* **2022**, *606*, 1311–1321, doi:10.1016/j.jcis.2021.08.176.
55. Song, Y.; Qi, J.; Tian, J.; Gao, S.; Cui, F. Construction of Ag/g-C₃N₄ Photocatalysts with Visible-Light Photocatalytic Activity for Sulfamethoxazole Degradation. *Chem. Eng. J.* **2018**, *341*, 547–555, doi:10.1016/j.cej.2018.02.063.
56. Li, F.; Zhao, R.; Yang, B.; Wang, W.; Liu, Y.; Gao, J.; Gong, Y. Facial Synthesis of Dandelion-like g-C₃N₄/Ag with High Performance of Photocatalytic Hydrogen Production. *Int. J. Hydrogen Energy* **2019**, *44*, 30185–30195, doi:10.1016/j.ijhydene.2019.09.217.
57. Ge, L.; Han, C.; Liu, J.; Li, Y. Enhanced Visible Light Photocatalytic Activity of Novel

- Polymeric g-C₃N₄ Loaded with Ag Nanoparticles. *Appl. Catal. A Gen.* **2011**, 409-410, 215–222, doi:10.1016/j.apcata.2011.10.006.
58. Deng, Q.; Tang, H.; Liu, G.; Song, X.; Xu, G.; Li, Q.; Ng, D.H.L.; Wang, G. The Fabrication and Photocatalytic Performances of Flower-like Ag nanoparticles/ZnO Nanosheets-Assembled Microspheres. *Appl. Surf. Sci.* **2015**, 331, 50–57, doi:10.1016/j.apsusc.2014.12.202.
 59. Gogoi, D.; Shah, A.K.; Qureshi, M.; Golder, A.K.; Peela, N.R. Silver Grafted Graphitic-Carbon Nitride Ternary Hetero-Junction Ag/g-C₃N₄ (Urea)- g-C₃N₄ (Thiourea) with Efficient Charge Transfer for Enhanced Visible-Light Photocatalytic Green H₂ Production. *Appl. Surf. Sci.* **2021**, 558, 149900, doi:10.1016/j.apsusc.2021.149900.
 60. Ho, P.-N.-T.; Nguyen, T.-B.; Huang, C.P.; Doong, R.; Chen, C.-W.; Dong, C.-D. In-Situ Immobilization of Ag/AgCl on Sulfurized g-C₃N₄ Nanosheet for Enhancing Visible-Light Driven Photocatalysis toward Simultaneous Oxidation of Tetracycline and Reduction of Cr(VI) in Water. *J. Environ. Chem. Eng.* **2023**, 11, 109453, doi:10.1016/j.jece.2023.109453.
 61. Bao, Y.; Chen, K. AgCl/Ag/g-C₃N₄ Hybrid Composites: Preparation, Visible Light-Driven Photocatalytic Activity and Mechanism. *Nano-Micro Lett.* **2016**, 8, 182–192, doi:10.1007/s40820-015-0076-y.
 62. Zhang, H.; Bian, H.; Wang, F.; Zhu, L.; Zhang, S.; Xia, D. Enhanced Photocatalytic Reduction of CO₂ over P g-C₃N₄ -Supported TiO₂ Nanoparticles with Ag Modification. *Colloids Surfaces A Physicochem. Eng. Asp.* **2023**, 674, 131989,

- doi:10.1016/j.colsurfa.2023.131989.
63. Zhang, Z.; Sun, Y.; Wang, Y.; Yang, Y.; Wang, P.; Shi, L.; Feng, L.; Fang, S.; Liu, Q.; Ma, L.; et al. Synthesis and Photocatalytic Activity of g-C₃N₄/ZnO Composite Microspheres under Visible Light Exposure. *Ceram. Int.* **2022**, *48*, 3293–3302, doi:10.1016/j.ceramint.2021.10.104.
 64. Bai, X.; Zong, R.; Li, C.; Liu, D.; Liu, Y.; Zhu, Y. Enhancement of Visible Photocatalytic Activity via Ag@C₃N₄ Core–shell Plasmonic Composite. *Appl. Catal. B Environ.* **2014**, *147*, 82–91, doi:10.1016/j.apcatb.2013.08.007.
 65. Wang, P.; Huang, B.; Qin, X.; Zhang, X.; Dai, Y.; Wei, J.; Whangbo, M. Ag@AgCl: A Highly Efficient and Stable Photocatalyst Active under Visible Light. *Angew. Chemie Int. Ed.* **2008**, *47*, 7931–7933, doi:10.1002/anie.200802483.
 66. Sun, Y.; Xiong, T.; Ni, Z.; Liu, J.; Dong, F.; Zhang, W.; Ho, W.-K. Improving g-C₃N₄ Photocatalysis for NO_x Removal by Ag Nanoparticles Decoration. *Appl. Surf. Sci.* **2015**, *358*, 356–362, doi:10.1016/j.apsusc.2015.07.071.
 67. Ma, R.; Zhang, S.; Li, L.; Gu, P.; Wen, T.; Khan, A.; Li, S.; Li, B.; Wang, S.; Wang, X. Enhanced Visible-Light-Induced Photoactivity of Type-II CeO₂/g-C₃N₄ Nanosheet toward Organic Pollutants Degradation. *ACS Sustain. Chem. Eng.* **2019**, *7*, 9699–9708, doi:10.1021/acssuschemeng.9b01477.
 68. Qi, K.; Li, Y.; Xie, Y.; Liu, S.; Zheng, K.; Chen, Z.; Wang, R. Ag Loading Enhanced Photocatalytic Activity of g-C₃N₄ Porous Nanosheets for Decomposition of Organic Pollutants. *Front. Chem.* **2019**, *7*, doi:10.3389/fchem.2019.00091.

-
69. Chen, L.; Meng, D.; Wu, X.; Wang, A.; Wang, J.; Wang, Y.; Yu, M. In Situ Synthesis of V^{4+} and Ce^{3+} Self-Doped $BiVO_4/CeO_2$ Heterostructured Nanocomposites with High Surface Areas and Enhanced Visible-Light Photocatalytic Activity. *J. Phys. Chem. C* **2016**, *120*, 18548–18559, doi:10.1021/acs.jpcc.6b04131.
70. Sun, X.; Xu, T.; Xian, T.; Yi, Z.; Liu, G.; Dai, J.; Yang, H. Insight on the Enhanced Piezo-Photocatalytic Mechanism of $In_2O_3/BiFeO_3$ Heterojunctions for Degradation of Tetracycline Hydrochloride. *Appl. Surf. Sci.* **2023**, *640*, 158408, doi:10.1016/j.apsusc.2023.158408.
71. Chen, H.; Wang, J.M.; Zhao, Y.L.; Zhang, J.Q.; Cao, C.N. Electrochemical Performance of Zn-Substituted $Ni(OH)_2$ for Alkaline Rechargeable Batteries. *J. Solid State Electrochem.* **2005**, *9*, 421–428, doi:10.1007/s10008-004-0578-x.
72. Huang, W.; Li, Z.; Wu, C.; Zhang, H.; Sun, J.; Li, Q. Delaminating Ti_3C_2 MXene by Blossom of $ZnIn_2S_4$ Microflowers for Noble-Metal-Free Photocatalytic Hydrogen Production. *J. Mater. Sci. Technol.* **2022**, *120*, 89–98, doi:10.1016/j.jmst.2021.12.028.
73. Suhag, M.H.; Khatun, A.; Tateishi, I.; Furukawa, M.; Katsumata, H.; Kaneco, S. One-Step Fabrication of the $ZnO/g-C_3N_4$ Composite for Visible Light-Responsive Photocatalytic Degradation of Bisphenol E in Aqueous Solution. *ACS Omega* **2023**, *8*, 11824–11836, doi:10.1021/acsomega.2c06678.
74. Liu, W.; Wang, M.; Xu, C.; Chen, S. Facile Synthesis of $g-C_3N_4/ZnO$ Composite with Enhanced Visible Light Photooxidation and Photoreduction Properties. *Chem. Eng. J.* **2012**, *209*, 386–393, doi:10.1016/j.cej.2012.08.033.

75. Qamar, M.; Gondal, M.A.; Yamani, Z.H. Synthesis of Nanostructured NiO and Its Application in Laser-Induced Photocatalytic Reduction of Cr(VI) from Water. *J. Mol. Catal. A Chem.* **2011**, *341*, 83–88, doi:10.1016/j.molcata.2011.03.029.
76. Sun, Q.; Hu, X.; Zheng, S.; Zhang, J.; Sheng, J. Effect of Calcination on Structure and Photocatalytic Property of N-TiO₂/g-C₃N₄ @diatomite Hybrid Photocatalyst for Improving Reduction of Cr(VI). *Environ. Pollut.* **2019**, *245*, 53–62, doi:10.1016/j.envpol.2018.10.121.
77. Saravanakumar, K.; Karthik, R.; Chen, S.-M.; Vinoth Kumar, J.; Prakash, K.; Muthuraj, V. Construction of Novel Pd/CeO₂/g-C₃N₄ Nanocomposites as Efficient Visible-Light Photocatalysts for Hexavalent Chromium Detoxification. *J. Colloid Interface Sci.* **2017**, *504*, 514–526, doi:10.1016/j.jcis.2017.06.003.
78. Rosli, S.A.; Alias, N.; Bashrom, N.; Ismail, S.; Tan, W.K.; Kawamura, G.; Matsuda, A.; Lockman, Z. Hexavalent Chromium Removal via Photoreduction by Sunlight on Titanium–Dioxide Nanotubes Formed by Anodization with a Fluorinated Glycerol–Water Electrolyte. *Catalysts* **2021**, *11*, 376, doi:10.3390/catal11030376.
79. Meichtry, J.M.; Colbeau-Justin, C.; Custo, G.; Litter, M.I. Preservation of the Photocatalytic Activity of TiO₂ by EDTA in the Reductive Transformation of Cr(VI). Studies by Time Resolved Microwave Conductivity. *Catal. Today* **2014**, *224*, 236–243, doi:10.1016/j.cattod.2013.10.021.
80. Hsu, H.-T.; Chen, S.-S.; Tang, Y.-F.; Hsi, H.-C. Enhanced Photocatalytic Activity of chromium(VI) Reduction and EDTA Oxidization by Photoelectrocatalysis Combining Cationic Exchange Membrane Processes. *J. Hazard. Mater.* **2013**, *248-249*, 97–106,

doi:10.1016/j.jhazmat.2012.12.058.

81. Kohantorabi, M.; Moussavi, G.; Oulego, P.; Giannakis, S. Synthesis of a Novel, Ternary AgI/CeO₂@g-C₃N₄ Nanocomposite with Exceptional Stability and Reusability for Visible Light-Assisted Photocatalytic Reduction of Hexavalent Chromium. *Appl. Surf. Sci.* **2021**, 555, 149692, doi:10.1016/j.apsusc.2021.149692.
82. Patnaik, S.; Das, K.K.; Mohanty, A.; Parida, K. Enhanced Photo Catalytic Reduction of Cr (VI) over Polymer-Sensitized g-C₃N₄/ZnFe₂O₄ and Its Synergism with Phenol Oxidation under Visible Light Irradiation. *Catal. Today* **2018**, 315, 52–66, doi:10.1016/j.cattod.2018.04.008.
83. Liu, R.; Yang, W.; He, G.; Zheng, W.; Li, M.; Tao, W.; Tian, M. Ag-Modified g-C₃N₄ Prepared by a One-Step Calcination Method for Enhanced Catalytic Efficiency and Stability. *ACS Omega* **2020**, 5, 19615–19624, doi:10.1021/acsomega.0c02161.
84. Sun, X.; Zheng, Z.; Ma, J.; Xian, T.; Liu, G.; Yang, H. Development of Ternary Pt/BaTiO₃/Bi₂O₃ Heterostructured Piezo-Photocatalysts for Antibiotic Degradation. *Appl. Surf. Sci.* **2024**, 653, 159421, doi:10.1016/j.apsusc.2024.159421.
85. Shi, Q.; Li, Z.; Chen, L.; Zhang, X.; Han, W.; Xie, M.; Yang, J.; Jing, L. Synthesis of SPR Au/BiVO₄ Quantum Dot/rutile-TiO₂ Nanorod Array Composites as Efficient Visible-Light Photocatalysts to Convert CO₂ and Mechanism Insight. *Appl. Catal. B Environ.* **2019**, 244, 641–649, doi:10.1016/j.apcatb.2018.11.089.
86. Chenthamarakshan, C.R.; Rajeshwar, K.; Wolfrum, E.J. Heterogeneous Photocatalytic Reduction of Cr(VI) in UV-Irradiated Titania Suspensions: Effect of Protons, Ammonium

Ions, and Other Interfacial Aspects. *Langmuir* **2000**, *16*, 2715–2721, doi:10.1021/la9911483.

CHAPTER FOUR

Summary and Thesis Conclusions

4.1 Summary and Thesis Conclusions

A major environmental problem is the increase in heavy metal pollution caused by industrial activities. One of the most common and harmful heavy metals is chromium. The technology of photocatalytic remediation has gained a lot of attention for the reduction of heavy metals from aqueous solutions due to its beneficial properties such as cost-effectiveness, ease of operation, less secondary pollution, and eco-friendly nature. The objectives of this thesis were to develop different composite materials based on graphitic carbon nitride, and these were applied for the photocatalytic remediation of hazardous hexavalent chromium, Cr(VI), in aqueous solutions. The thesis is divided into four chapters.

❖ In chapter one

Chapter one is focused on the general introduction to heavy metals, types of heavy metals, and sources. Subsequently, an overview of toxic Cr(VI) is provided, including its sources, toxicity, and effects on health. The conventional removal techniques for removing contaminants from aqueous solutions, along with their benefits and drawbacks, are briefly discussed. Next, a thorough explanation of the photocatalytic remediation process has been mentioned. After that, the theoretical general background about graphitic carbon nitride and possible approaches to modify its properties via different approaches, including elemental doping, heterojunction formation with other semiconductors, etc., are described. Finally, the reaction mechanism of the photocatalytic remediation technique has been elaborately illuminated.

❖ In chapter two

Facile synthesis of ZnO/g-C₃N₄ with enhanced photocatalytic performance for the reduction of Cr(VI) in the presence of EDTA under visible light irradiation is studied. The ZnO/g-C₃N₄ composite was synthesized through a facile one step calcination method using urea and zinc acetate

dehydrate precursors. The results of thermogravimetric analysis (TGA), X-ray diffraction (XRD), fourier transform infrared (FTIR), Brunauer–Emmett–Teller (BET) surface area, scanning electron microscopy (SEM), transmission electron microscopy (TEM), and X-ray photoelectron spectroscopy (XPS) investigation unequivocally demonstrated that the ZnO/g-C₃N₄ composite was successfully synthesized. The UV-visible DRS, PL, and EIS measurements were used to evaluate the narrower band gap, decreased PL intensity, and smaller arc radius, respectively, of composites. In the presence of sacrificial electron donor EDTA, the ZnO/g-C₃N₄ photocatalyst showed better visible light response photocatalytic reduction ability against Cr(VI). Several parameters have been adapted for photocatalytic Cr(VI) reduction, such as ZnO amount in the composite, synthesis calcination condition, catalytic dosage, initial concentration of Cr(VI), EDTA concentration and solution pH. Moreover, after fifth cycle, ZnO/g-C₃N₄ composite showed modest stability. The possible photocatalytic reaction mechanisms and pathway have been proposed.

❖ In chapter three

Fabrication of semiconductors by metal element has received considerable attention to enhance carrier separation and migration rates of e^-h^+ pairs and retain strong redox abilities. Since, The facile fabrication of Ag/g-C₃N₄ photocatalyst with visible light responsive efficiency for Cr(VI) reduction in the presence of EDTA was investigated. In order to enhance photocatalytic Cr(VI) reduction from aqueous solution, g-C₃N₄ was fabricated by Ag to synthesize Ag/g-C₃N₄ composite via a simple one-step calcination method from urea and AgNO₃. The amount of Ag content in the Ag/g-C₃N₄ composite affected the photocatalytic performance of the Ag/g-C₃N₄ composite. The properties of the as-synthesized Ag/g-C₃N₄ were examined by a series of characterization techniques such as TG, XRD, FTIR, XPS, BET, SEM, TEM UV-visible DRS, PL, and EIS analysis. Additionally, the influence of various factors, including Ag quantity in the composite,

calcination temperature and time, amount of catalyst, initial Cr(VI) concentration, ethylenediaminetetraacetic acid (EDTA) concentration, and pH, was studied to find an optimized condition for Cr(VI) reduction. The Ag/g-C₃N₄ composite containing 22 wt% of Ag exhibits 96% photocatalytic Cr(VI) reduction within 30 min in the presence of EDTA. The rate constant using Ag/g-C₃N₄ composite (0.1054 min⁻¹) was 6 times higher than that of g-C₃N₄ (0.0177 min⁻¹) in the presence of EDTA.

❖ In chapter four

Research conclusions on the advancement of photocatalytic technology for reducing toxic hexavalent chromium are described.

List of Published Articles

1. “Facile Synthesis of ZnO/g-C₃N₄ with Enhanced Photocatalytic Performance for the Reduction of Cr(VI) in Presence of EDTA Under Visible Light Irradiation.”

Aklima Khatun, Mahmudul Hassan Suhag, Mai Furukawa, Ikki Tateishi, Hideyuki Katsumata, Satoshi Kaneco, International Journal of environmental research 2023, 17:32.

<https://doi.org/10.1007/s41742-023-00522-0>

2. “Facile Fabrication of Ag/g-C₃N₄ Photocatalyst with Visible Light Responsive Efficiency for Cr(VI) Reduction in Presence of EDTA.”

Aklima Khatun, Mahmudul Hassan Suhag, Mai Furukawa, Ikki Tateishi, Hideyuki Katsumata, Satoshi Kaneco, Environmental Processes 2024, 11:28.

<https://doi.org/10.1007/s40710-024-00705-7>

List of Attending Conference

1. “Facile Synthesis of ZnO/g-C₃N₄ with Enhanced Photocatalytic Performance for the Reduction of Cr(VI) in Presence of EDTA Under Visible Light Irradiation.”
Aklima Khatun, Mai Furukawa, Ikki Tateishi, Hideyuki Katsumata, Satoshi Kaneco 12th
International Symposium for Sustainability by Engineering.
Mie University, Japan. 27-28th September 2022.
2. “Facile Fabrication of Ag/g-C₃N₄ Photocatalyst with Visible Light Responsive Efficiency for Cr(VI) Reduction in Presence of EDTA.”
Aklima Khatun, Mai Furukawa, Ikki Tateishi, Hideyuki Katsumata, Satoshi Kaneco 13th
International Symposium for Sustainability by Engineering.
Mie University, Japan. 27-28th September 2023.